UNIVERSITÀ
DEGLI STUDI DI ROMA
TOR VERGATA

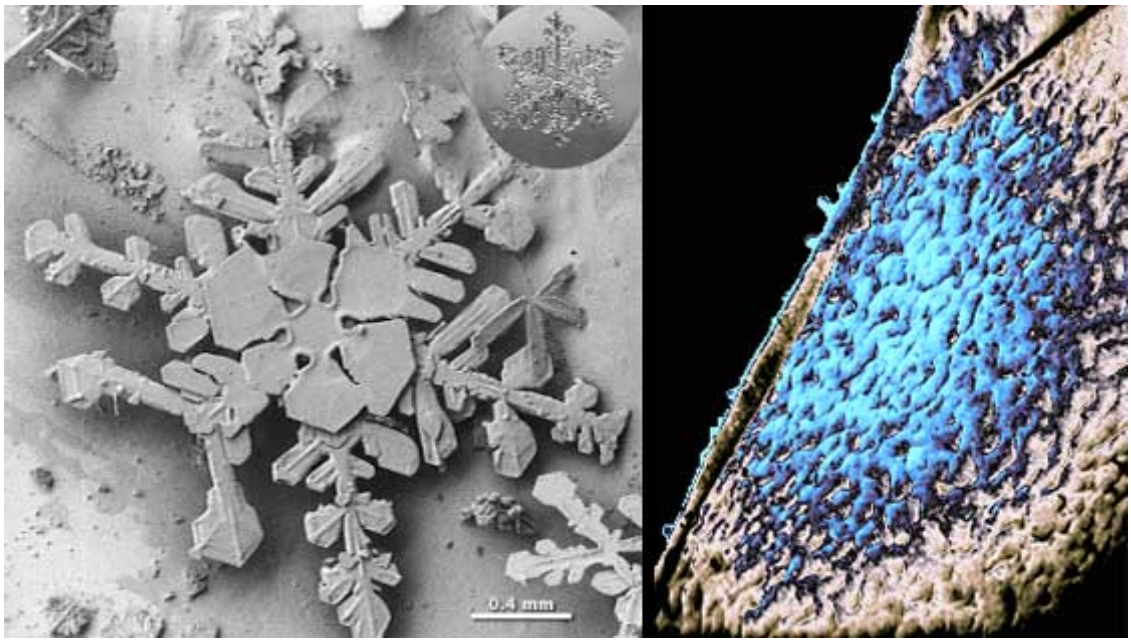

Follow the water

An insight into proton quantum dynamics of selected phases of water by inelastic neutron scattering

ALEXANDRA PARMENTIER

PhD Program in Physics - cycle XXVIII
Dept. of Physics - Tor Vergata University of Rome, Italy

FOLLOW THE WATER
An insight into proton quantum dynamics of selected phases of water by inelastic neutron scattering

SUPERVISORS
Prof. C. Andreani, Dept. of Physics, Tor Vergata University of Rome, Italy
Prof. R. Senesi, Dept. of Physics, Tor Vergata University of Rome, Italy

PhD COORDINATOR
Prof. R. Benzi, Dept. of Physics, Tor Vergata University of Rome, Italy

PhD Thesis 2016
SWING group
Dept. of Physics
Tor Vergata University
Rome, Italy

Cover: A familiar snowflake (ice I_h) and a representation of high density amorphous ice. Credits: NASA/Earth Observatory (left) and NASA/ARC/P. Jenniskens and D.F. Blake (right).

Typeset in LaTeX
Rome, Italy 2016

Abstract

The present PhD thesis stems from 36 months of intensive experimental investigation and data analysis of quantum dynamics of the hydrogen nucleus in various amorphous solid states (AIs) and supercritical phase (SCW) of water by inelastic neutron scattering.

This doctoral effort places this work into the apparently inexhaustible stream of studies on water, at the same time offering an evidence of the role of density in shaping the single-particle potential-energy surface in terms of curvature and anharmonicity, as highlighted by a recent high-impact publication in *J. Phys. Chem. Lett.* [1].

The layout of the monograph has been thought for a broad audience, with an eye to making it both agile and exhaustive. After a brief introduction on the why and how of water and neutron spectroscopy, two separate chapters are dedicated to the properties of amorphous ices and the supercritical fluid, followed by the presentation of the fundamentals of inelastic (INS) and deep-inelastic (DINS) neutron techniques, and a sketch of the instrumentation employed, which is functional to the full understanding of the development of data reduction and analysis.

The subsequent chapter on the potential of mean force (PMF) introduces an alternative and possibly easier-to-manage way to interpret DINS outputs. The arrangement of related data and their interpretation into a scientific paper for a special issue of *Front. Phys.* is currently afoot.

The work closes with a clean report of experimental results and relative discussion, which allows for inferring new insights into the function and effects of the H-bond environment the molecules are immersed in, as well as picturing future investigation scenarios.

All INS and DINS experiments described in the following sections were performed at MARI and VESUVIO spectrometers, respectively, both located at ISIS Neutron and Muon Pulsed Source at the Rutherford Appleton Laboratory in the UK, with later data analysis and interpretation developed at the Department of Physics of Tor Vergata University of Rome, Italy.

A detailed scheme of my contribution to the stages of the above-mentioned activities is given below.

	Proposal	Exp prep	Measurements	Analysis	Interpretation
AIs INS			√	√	√
AIs DINS	√	√	√	√	√
SCW DINS				√	√
PMF DINS				√	√

The experimental work was accompanied by the participation by poster contribution in the 2013 International Conference on Neutron Scattering in Edinburgh, UK, the VI Workshop in eV Neutron Spectroscopy (2014) in Abingdon, UK, and the 2016 Erice School ('Water and Water Systems') held in Erice (TP), Italy, and promoted by the School of Neutron Scattering (SoNS) entitled to Francesco Paolo Ricci.

The second meeting called for my personal involvement into the coordination of the final scientific discussion, which is currently included in the proceedings of the conference [2–4].
A fruitful introduction to the PhD route was for sure the pre-doctorate course on general neutron scattering held by ILL in summer 2012 (Giornate Didattiche).
As to present, I am about to start a full-immersion training as a McStas professional user, in order to participate in the development of the VESPA Project at the European Spallation Source (ESS).
A parallel collaboration is in progress with a team based in Sapienza University of Rome in order to investigate anomalous transport properties of ultraconfined water by quasi-elastic neutron scattering (QENS) [5] and other spectroscopic techniques.

Keywords: water, amorphous ices, supercritical water, INS, DINS, PMF

Acknowledgements

The road to a robust PhD dissertation is a hard path where the candidate's commitment proves vital, yet not sufficient.
Each of us involved in this kind of task has directly experienced how large an influence the human environment we are daily bathed in can have upon our research work and life in general, to such a point to embrace it as a real surrogate family.
The following, to which my thanks are directed, is mine.
First, thanks to my supervisors, Prof. C. Andreani and Prof. R. Senesi. When I entered (then unfamiliar) Tor Vergata University in 2012 with my fresh PhD grant, they provided this early NMR and dielectric spectroscopist with the exciting opportunity to keep studying a beloved topic - water - from the point of view of a new powerful experimental technique. And they operated as smart mentors and filters in the large international scene I was in and around in order to carry out my experiments and formal education. Without their constant support and precious inputs no important target would have been achieved.
I would like to thank my lab mates, too - Giovanni, Alice, Giulia, Federico, Laura, Pamela - each in his/her own role, as well as all people met in Casa Azzurri at Abingdon, and at ISIS Neutron Source at Harwell, on the occasion of experimental trips to the UK. Lots of serious talks and laughs have gladdened our minds and hearts in these three years - no chance to get bored or gloomy. A real dream team.
Once again, thanks to Gianluca, my computer wizard. Still here after ten years and so many hurdles - quite frankly, I suspect he is a superhero.
And thanks to my parents. They cannot witness this event, but they worked hard to make it possible.
I love you, folks.

Rome, October 2016

Contents

List of Figures

List of Tables

1

Introduction

Un homme qui ne boit que de l'eau a un secret à cacher à ses semblables

Charles Baudelaire

1.1 The archetypal substance

No matter how far one may roam back into past history, water has ever represented an anthropological paradigm.
An early preserve of phylosophy and religion, it officially entered the domain of non-elemental modern science in the late 18^{th} century, also making its debut as a standard in the newborn International System of Units.
And still today this substance 'the solar system and beyond is awash in' [6] keeps representing a source of fascination to the physical scientist due to a jungle of more than 70 counterintuitive anomalies that are at the core of water's role as the 'matrix of life' [7, 8].
Such anomalies are quantitatively small at room temperature and standard pressures, though qualitatively significant. Yet more pronounced peculiarities become apparent when one starts to explore outer regions of the phase diagram.

1.2 A weird behavior

Fig. 1.1 is taken from an old classic of the 70s' by Speedy and Angell [9]. Here a number of thermophysical properties of water are measured down to 247 K, with associated response functions that increase sharply in magnitude upon cooling and appear to diverge at a singular temperature $T_s = 228$ K.
It was Speedy himself, in 1982, to propose a theoretical explanation for this behavior [10,11] (Fig. 1.2, case (a)). Unlike normal liquids, water's liquid-gas spinodal[1] would go to negative pressures with a positive slope at high temperature, then meeting the locus of temperatures of maximum density and retracing back to positive pressures.

[1]The liquid-gas spinodal curve sets the limit of stability of superheated water with respect to vapor formation. In a normal liquid it curves monotonically away from the critical point to meet null absolute temperature at large negative pressures.

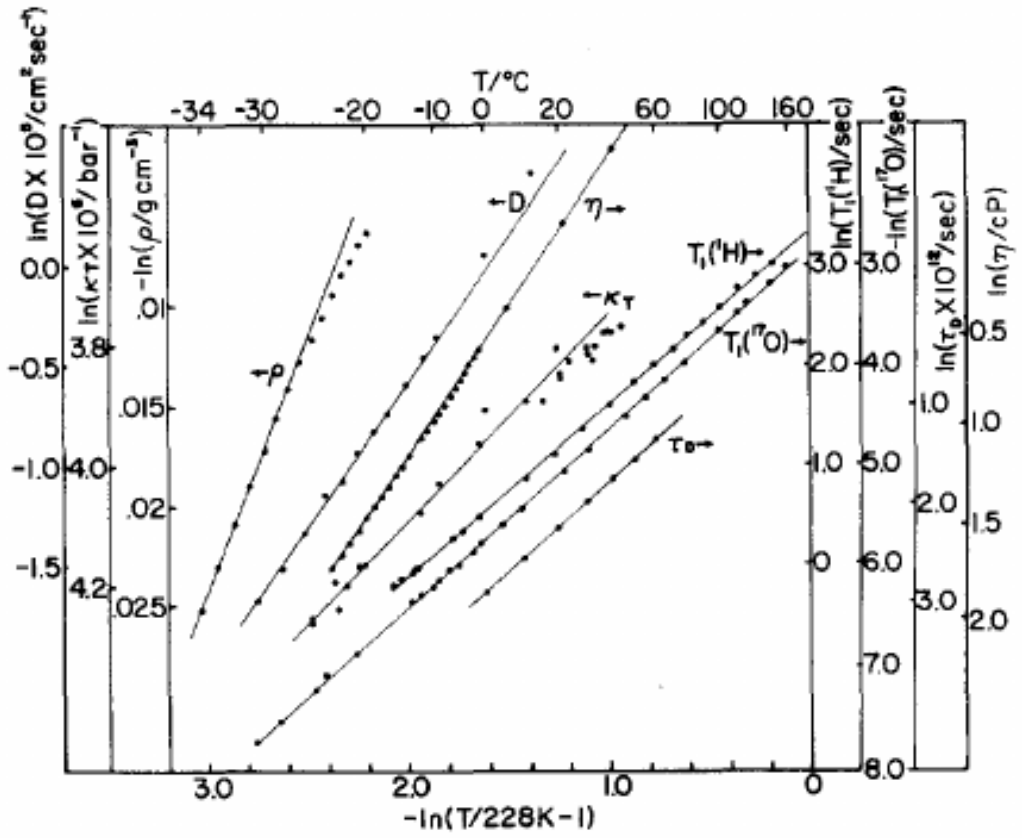

Figure 1.1: A double-log plot of major response functions and relaxation times of water at atmospheric pressure, suggesting a power-law trend and implying an extrapolated divergence of all represented quantities near $T_s = 228$ K. From left to right: ρ (density), D (diffusion coefficient), η (viscosity), κ_T (isothermal compressibility), $T_1(^1\mathrm{H})$ (proton spin-lattice relaxation time), $T_1(^{17}\mathrm{O})$ (oxygen spin-lattice relaxation time), τ_D (dielectric relaxation time). Reproduced from [9].

This scenario was argued by Debenedetti on the basis of thermodynamic consistency arguments combined with simulation results[2] [12].
More recently (1992) Poole et al. submitted another intriguing justification for water anomalies [13] (Fig. 1.2, case (c)).
In their tracking of Speedy's spinodal by simulation, they found an anomaly in the $p - \rho$ relation at positive pressures which, at the limit of simulation capability, developed into a van der Waals loop. Such result was interpreted in terms of the existence, at low temperature, of fluctuations around a liquid-liquid critical point (LLCP), below which a tetrahedrally coordinated low-density liquid (LDL) should coexist with a less structured liquid of higher density (HDL), in fact mimicking the corresponding supercritical subdomains placed aside the so-called Widom line (Fig. 1.3). This would rationalize the occurrence of high-density and low-density amorphous states as the vitrified counterparts of such fluids. Above the LLCP, the fraction of temporarily existing LDL patches would progressively decrease, so that supercooled and stable water could be pictured as a mixture of high- and low-density components[3].
No need to say that a major problem emerges with Poole's scheme, which concerns its validation for both the ST2 model[4] used in [13] and real water.
Indeed, apart from ancestral disputes about the reliability of multiple water models retrieved in the literature, the sore spot here is the experimental inaccessibility of the alleged LLCP, which would be placed somewhere in the 'no man's land', the region where no bulk liquid water can be directly observed prior to the occurrence of homogeneously-nucleated crystallization below T_H (Fig. 1.4). A trick to suppress crystallization at any temperature would consist of relying on ultra-confined water samples, provided that the geometrical restriction is sufficiently severe to prevent molecules from rearranging in a tetrahedral ice structure. For example, nuclear magnetic resonance (NMR) spectroscopy and quasi-elastic neutron scattering (QENS) applied to water confined in nanopores allow for testing the proportionality between the inverse diffusion coefficient D^{-1} and the viscosity η, which actually gets broken on approaching the glass transition temperature T_g from the liquid side, thus signaling the existence of a fragile-to-strong crossover (see appendix A) in turn suggestive of a LLCP [17]. Yet no clear idea exists whether the properties of such a supercooled liquid are of relevance to the bulk counterpart [18]. On the other hand, ultrafast techniques approaching the timescale of homogeneous nucleation look promising [19].
That said, Poole's interpretation is highly debated [20, 21], with Chandler arguing that the appearance of LDL should only reflect transient local fluctuations that precede the completion of water's structural relaxation [22].

[2]For example, a retracing spinodal would require the metastable continuation of the boiling curve to terminate at a critical point placed below the triple-point temperature.

[3]That's just one example of two-fluid model for water, actually belonging to an extensive family rolled out by Roentgen in 1892 [15]. Also the one-component model family exists, which pivots on the idea of a continuous modification of the H-bond network topology. One-component formalizations quite well describe molecular mobility, but usually struggle to match the thermodynamic properties of the liquid.

[4]ST2 is a hystorical water model introduced in 1974 by Stillinger and Rahman [16] belonging to the 5-site model family, which places, within a tetrahedral-like geometry, the negative charges on dummy atoms representing the lone pairs of oxygen.

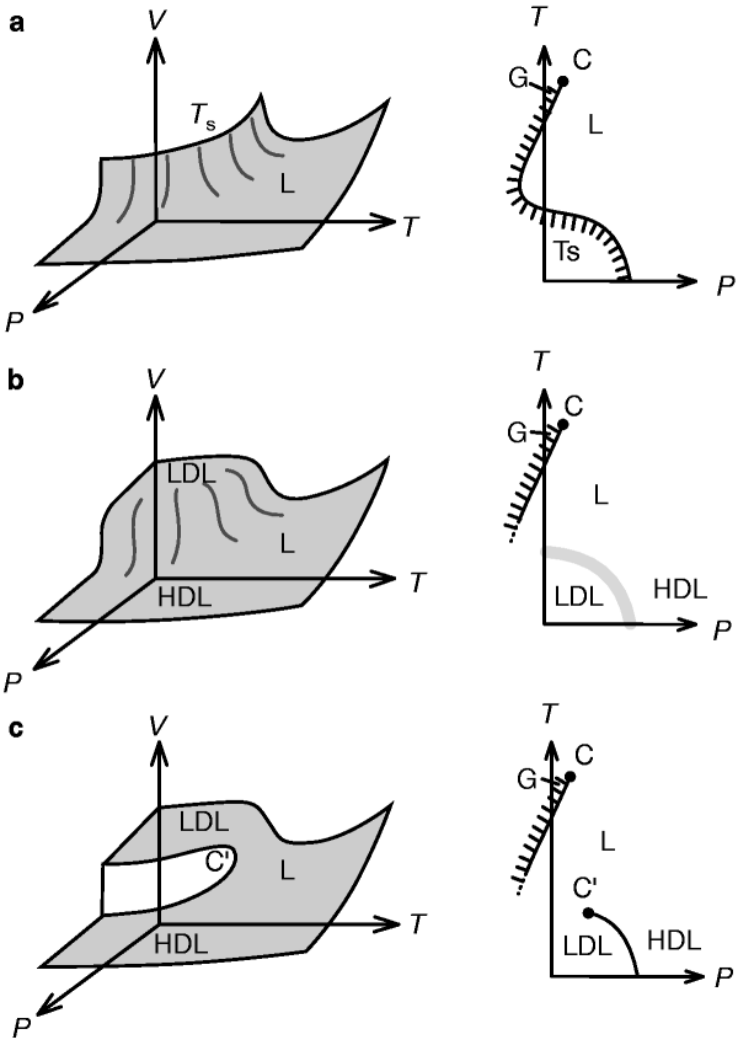

Figure 1.2: Popular theoretical scenarios to explain water anomalies: a) the stability-limit conjecture by Speedy (1982); b) the singularity-free hypothesis; c) the liquid-liquid phase-transition (LLPT) hypothesis by Poole et al. (1992). C and C' denote the known critical point and the conjectured LLCP at low temperature, respectively. Reproduced from [11].

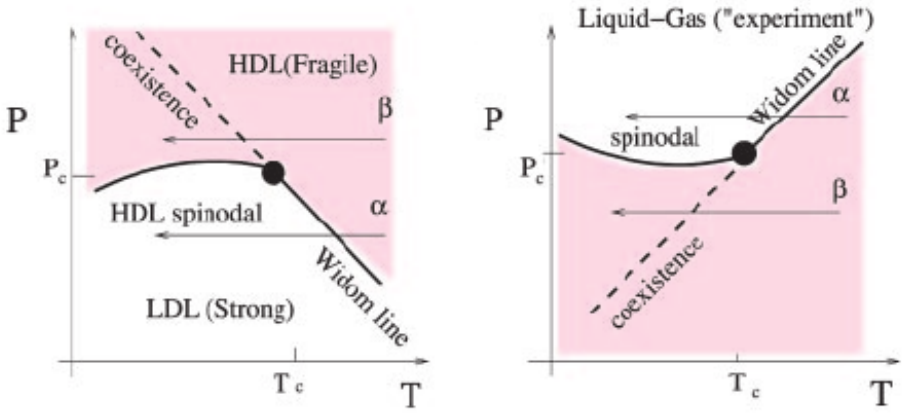

Figure 1.3: Right: Water's critical region associated with the liquid-gas CP, also showing a generic Widom line and the spinodal beyond which the gas phase is no longer stable (superheated water). Left: A hypothetical Widom line promanating from the LLCP in the 'no-man's land', with the associated HDL spinodal. Reproduced from [14] with modifications.

Finally, various singularity-free scenarios (Fig. 1.2, case (b)) have been popping out in the literature since the mid 90s' [12,23], which skip the LLCP, while retaining LDL and HDL metastable phases. These formalizations treat water as a locally structured transient system of bonded subdomains, as well as polyamorphic changes as mere relaxation phenomena.
It looks like there's still room for long discussions out there.
But, in the end, what is the key factor that underpins water's uniqueness? Hydrogen-bonding[5], which adds a supramolecular length scale to the microscopic network structure of water, is typically referred to as the principal character, yet different multiply H-bonded materials exist (think of hydrogen peroxide, H_2O_2, or hydrazine, N_2H_4, for example) that show none of water's anomalies.
That's seemingly a matter of local tetrahedral symmetry of the bonds instead (Fig. 1.5), as suggested by water's 'siblings' like Si and Ge, which belong to some group of tetrahedral-structure-forming species and show some of water's peculiarities.
Water's tetrahedrality is transient in the liquid and tends to become permanent in ice. Indeed, in bulk water, individual molecules are held together via H-bonds inside highly cooperative dynamic clusters which are continually subject to collapse, reconstruction, or rearrangement. Non-H-bonded adjacent molecules often interact with one another under the van der Waals modality, yet they can also interface with

[5]According to the 2011 IUPAC Recommendations [24], the hydrogen bond is an attractive interaction (energy of the order of several $\frac{Kcal}{mol}$ vs. the typical values of 80-100 $\frac{Kcal}{mol}$ of covalent bonds) between a hydrogen atom from a molecule or a molecular fragment X-H in which X is more electronegative than H, and an atom or a group of atoms in the same or a different molecule, in which there is evidence of bond formation. X-H represents the hydrogen bond donor. The acceptor may be an atom or an anion Y, or a fragment or a molecule Y-Z, where Y is bonded to Z. A renowned Compton-scattering study by Isaacs et al. [25] on I_h revealed, in 1999, the partial covalent, i.e., quantum nature of the hydrogen bond (already suggested by Pauling in the 30s' [26]) by exploitation of Compton-profile anisotropies along crystal axes, which are exceptionally sensitive to phase coherence of the electron wavefunctions (and, thus, to covalence) of bonded atoms.

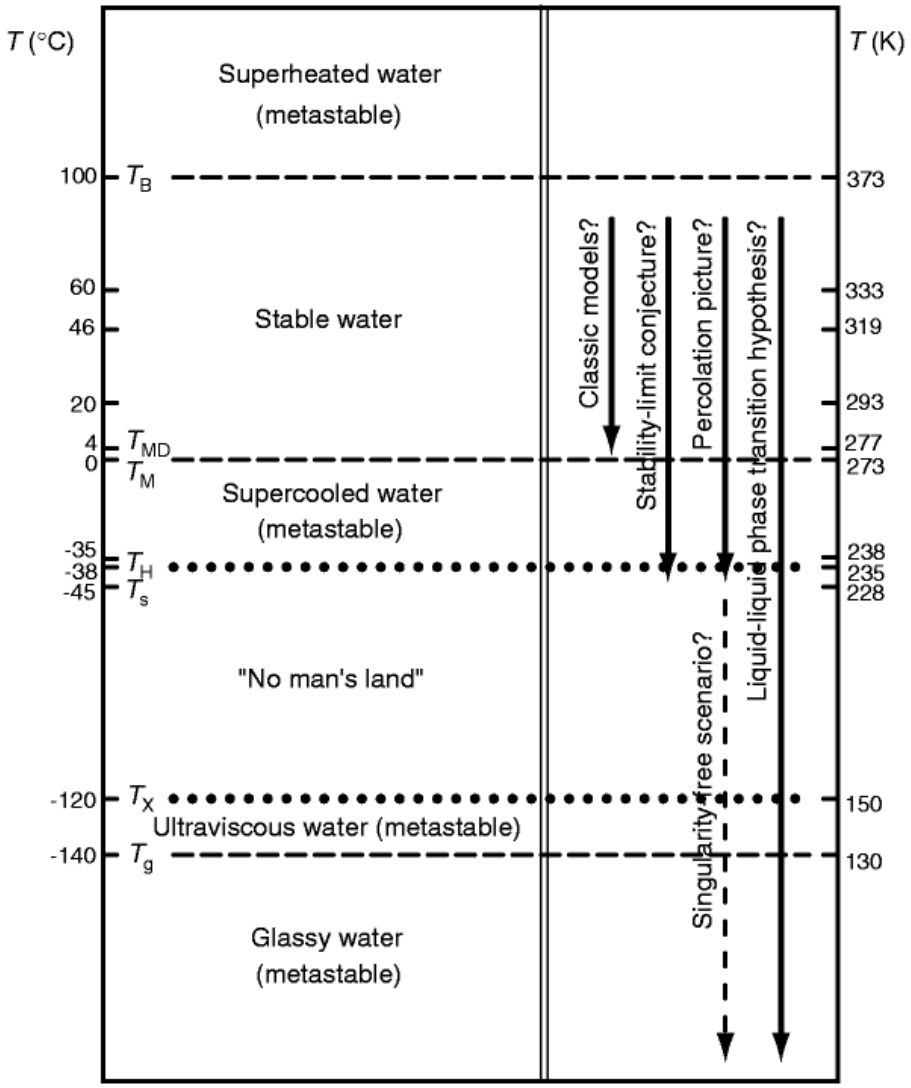

Figure 1.4: A scheme of different temperature domains for subcritical water at atmospheric pressure. The stable region is delimited by the equilibrium melting (T_M) and the boiling point (T_B), T_{MD} being the temperature of max density. T_H (homogeneous-nucleation temperature) and T_X (crystallization temperature) enclose the 'no man's land'-region. T_s is the singular temperature described in Fig. 1.1, while T_g marks the glass transition. Reproduced from [11].

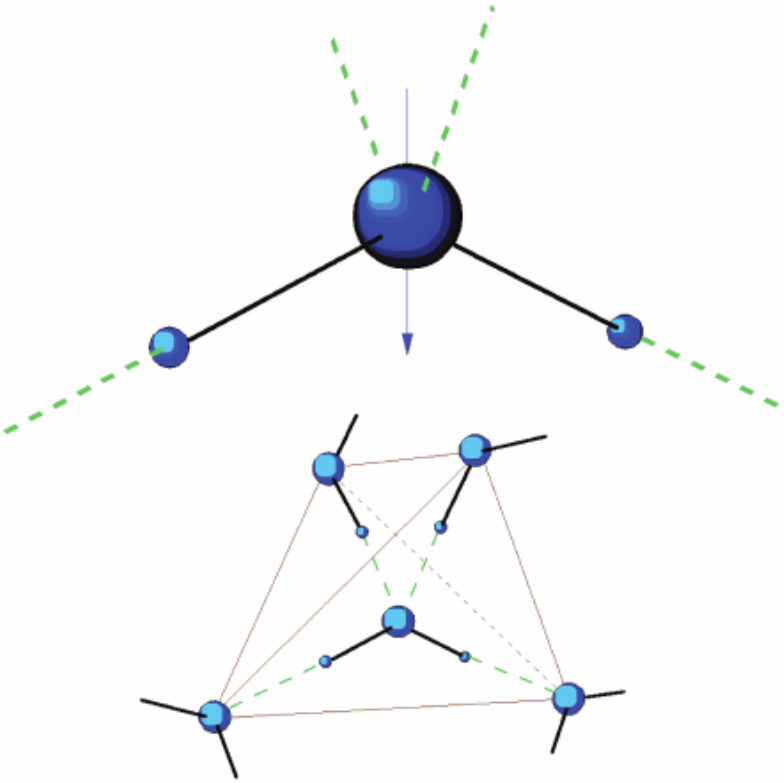

Figure 1.5: A scheme of the water molecule (top) and its tetrahedral arrangement in ice (bottom). Water has a polar molecule, with a marked electric dipole moment ($\sim$ 1.83 D) directed along its axis of simmetry. Its H-O-H angle is about 104.5° and its O-H distance about 0.96 Å. Its electronic structure consists of two σ orbitals that form the two covalent O-H bonds (H-bond donors), as well as two nonbonding orbitals that remain on its O-atom and are each occupied by two lone-pair electrons (H-bond acceptors). The geometry of these four electronic orbitals around the O-atom is approximately that of a tetrahedron. Anyway, it is important to understand that for a water dimer, all possible diagnostics of H bonding (binding energy, charge transfer, geometric criteria) are continuous (especially in the liquid phase), so any sharp cutoff separating H-bonded from non-H-bonded configurations is essentially arbitrary. Reproduced from [27].

already existing H-bonds in order to form sort of 'bifurcations' able to reduce the average life of the latter down to the order of picoseconds. These bifurcations are often modeled as large angular jumps within the mechanism of rotational relaxation of water [28]. Upon cooling the formation of bifurcations gets less and less probable, which causes a progressive strengthening of the tetrahedral clustering and the prolongation of H-bonding over time [29]. This macroscopically causes the characteristic anticorrelation of volume and entropy fluctuations observed in water below 277 K.
What said suggests that all experimental techniques giving specific spectral signatures of the bond network are the most suitable to investigate water.

1.3 Why neutrons?

Chemically speaking, the neutron can be interpreted as the completion of both the Periodic Table of Elements (from the point of view of its net charge, which is null) and of Nuclides (from the point of view of its mass - $m_n = 1.0087$ a.m.u. - slightly larger than the proton's). Further properties are outlined within the Standard Model, which defines this particle as one of the lightest baryons undergoing β-decay (when free) with a mean lifetime of about 15 min, as well as a fermion with half-integer spin and magnetic dipole moment $\mu_n = \frac{\gamma e \hbar}{2m_p}$ with negative gyromagnetic ratio ($\gamma = -1.913$).
These characteristics are the ground for neutrons' interaction with matter via strong and e.m. forces, usually with total cross-sections[6] small enough to allow for high (and non-destructive) penetrating power into the bulk of the investigated sample [31] (Fig. 1.6). Our apology of the neutron probe starts here, since this feature makes it ideal to investigate biological materials and samples under extreme conditions of pressure, temperature, magnetic field or within chemical reaction vessels.
Reasoning in terms of the wave nature of neutrons[7], wavelengths currently used for science can range from 10^{-4} Å to 1000 Å, which allows for the exploration of any species from single nuclei up to large molecular structures, such as biopolymers.
Strong interactions experienced by neutrons include two major families of events: scattering and absorption phenomena. Scattering can be either coherent (collective component; relative phases between the incident and the scattered waves preserved) or incoherent (single-particle contribution; phase relationships not maintained), thus proving sensitive to single- and two-particle spatiotemporal correlations in condensed

[6] As usual [30], cross section σ is interpreted as an area deriving from the ratio of the total number of particles interacting in all directions per second to the flux of the incident beam, thus quantifying the occurrence probability of an event involving a probe and a target at the atomic/molecular level. Differential cross-section $\frac{d\sigma}{d\Omega}$ gets defined when a specific solid angle Ω is monitored and represents the proportionality constant between the count rate and the product of the beam flux, the detector efficiency, the number of particles in the beam, and the subtended solid angle ($C = \eta\Phi\left[\frac{d\sigma}{d\Omega}\right]\Delta\Omega$). When also an energy range is spanned in the course of the process, a double-differential cross-section $\frac{d^2\sigma}{d\Omega dE}$ can be introduced, according to the identity $\sigma = \int_{4\pi} \frac{d\sigma}{d\Omega} d\Omega = \int\int \frac{d^2\sigma}{d\Omega dE'} d\Omega dE'$.
Notice how the dimension of $\frac{d^2\sigma}{d\Omega dE}$ is $\frac{m^2}{eV}$, unlike σ and $\frac{d\sigma}{d\Omega}$, which are areas.

[7] $E_n = \frac{h^2}{2m_n\lambda_n^2} = \frac{\hbar^2 k_n^2}{2m_n} = k_B T$, with λ_n the De Broglie wavelength.

matter. But also elastic (no change in energy of the wave after scattering) or inelastic, with an energy-transfer range spanning from the μeV order[8] to several hundred electronvolts. That means direct applications to both diffraction (i.e., structural investigation) and spectroscopy (i.e., inspection of dynamic properties), respectively, the latter starting from very slow diffusive motion in soft matter, through coherent intermolecular (phonons and magnons) and incoherent intramolecular modes (vibrations), up to the zero-point dynamics of single nuclei.
As to neutron scattering lengths[9], both their magnitudes and signs[10] vary in a rather irregular fashion as a function of the atomic (Z) or atomic-mass (A) number, with a relatively mild increase in absolute magnitude as one moves across the Periodic Table of Elements [31] and no scaling with the size of the electron cloud. This makes neutrons sensitive to light atoms, as well as to different isotopes of the same element (with the possibility to implement telling isotopic-substitution experiments) or different atoms with similar Z's (case in point: adjacent transition metals). The variation in b is also independent of the momentum transfer $\mathbf{Q}$, which means that, unlike the X-ray case, no hurdle is encountered at large Q-values with no severe limit on the information content from data, especially when Fourier transforms are calculated.
Finally, neutrons enable the study of magnetic structures (with associated spin dynamics) and nuclear-spin correlations, due to the interaction of μ_n with the magnetic moments of unpaired electrons and non-zero spins of some nuclei, respectively.
While no single probe can cover the whole span of time- and length-scales required for scientific enquiry, it's clear from the above outline how crucially important neutrons prove as a research tool.
Indeed, neutron science is able to reveal the structure and dynamics of atoms and molecules, linking molecular-scale properties to the macroscopic features of matter.

1.4 Why inelastic scattering?

The kinetic energy of a neutron beam is usually expressed in eV and referred to as a (detection) 'temperature'[11] with reference to the process of moderation in a medium at fixed T (Fig. 1.7).
A typical condensed-matter neutron spectrum for up-to-epithermal exchanged energies is given in Fig. 1.8.
The objective of inelastic neutron scattering (INS) techniques is primarily the measurement of scattered intensities as a function of both the momentum tranfer $\mathbf{Q}$ and energy E.

[8] Even the neV order, if spin-echo techniques are taken into account.

[9] In the low-energy s-wave-scattering limit, the square of the scattering lenght b returns something proportional to the cross section.

[10] From time to time, b can turn out complex, with the imaginary part describing absorption. This happens in the presence of low-lying resonances, with scattering and absorption cross sections depending on wavelength.

[11] Precisely, the neutron energy distribution is modeled through a Maxwell-Boltzmann curve, which, as known, describes the statistics of a particle system at thermal equilibrium under dilute-gas conditions. For thermal neutrons (energies around 25 meV) the most probable velocity corresponds to a temperature of 290 K.

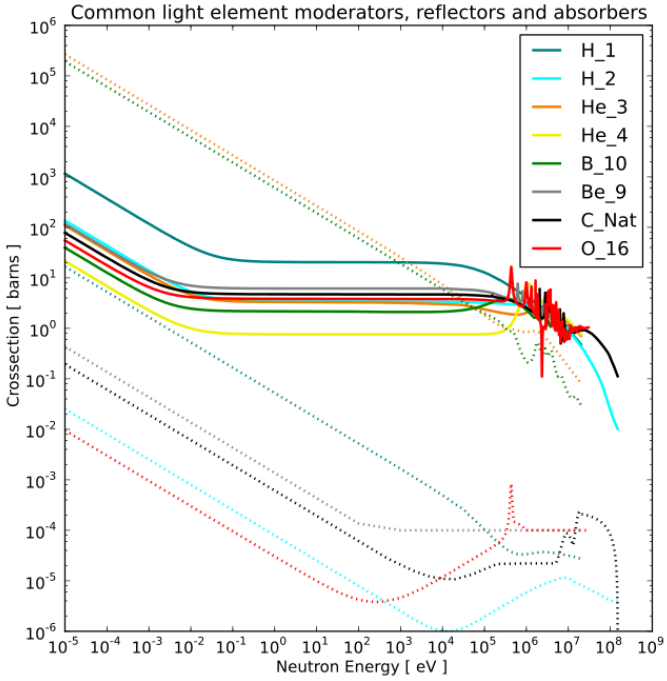

Figure 1.6: Scattering (full line) and absorption (dots) cross sections of light elements commonly used as neutron moderators, reflectors and absorbers. Data obtained from ENDF/B-VII database via JANIS software. Credits: ProkopHapala - Own work. Licensed under CC BY-SA 3.0 via Commons.

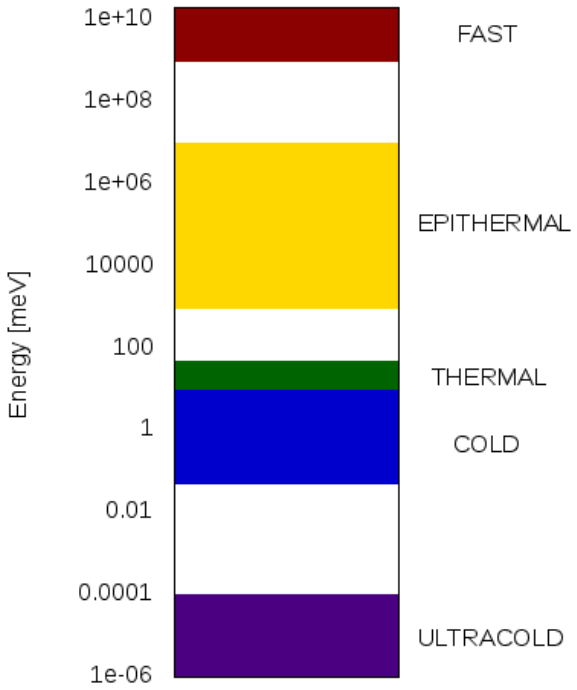

Figure 1.7: Typical classification of neutron 'temperatures'. Generated via Gnuplot 4.6.

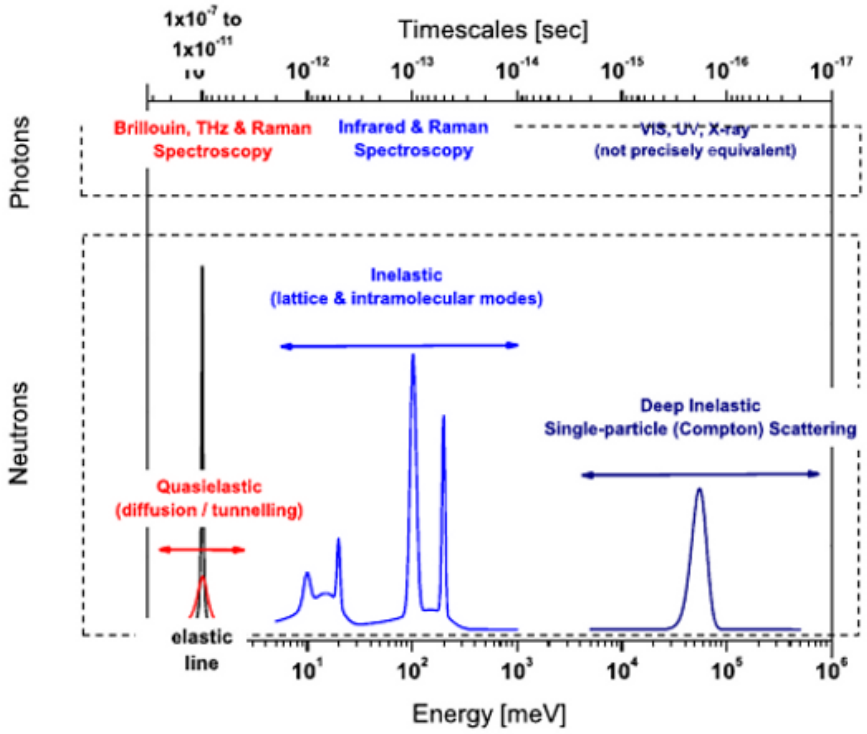

Figure 1.8: Common shape of a condensed-matter neutron spectrum for exchanged energies up to the epithermal region. Reproduced from [32].

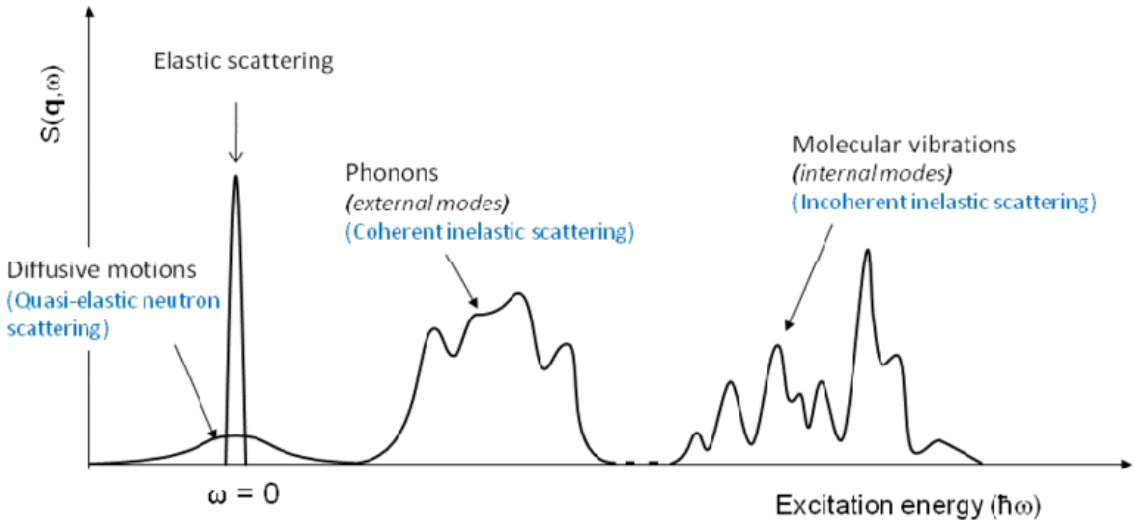

Figure 1.9: A zoom of the region enclosing energies less than epithermal. Reproduced from the ILL website (www.ill.eu/science-technology/science-at-ill/why-and-how/neutron-techniques/inelastic-neutron-scattering/).

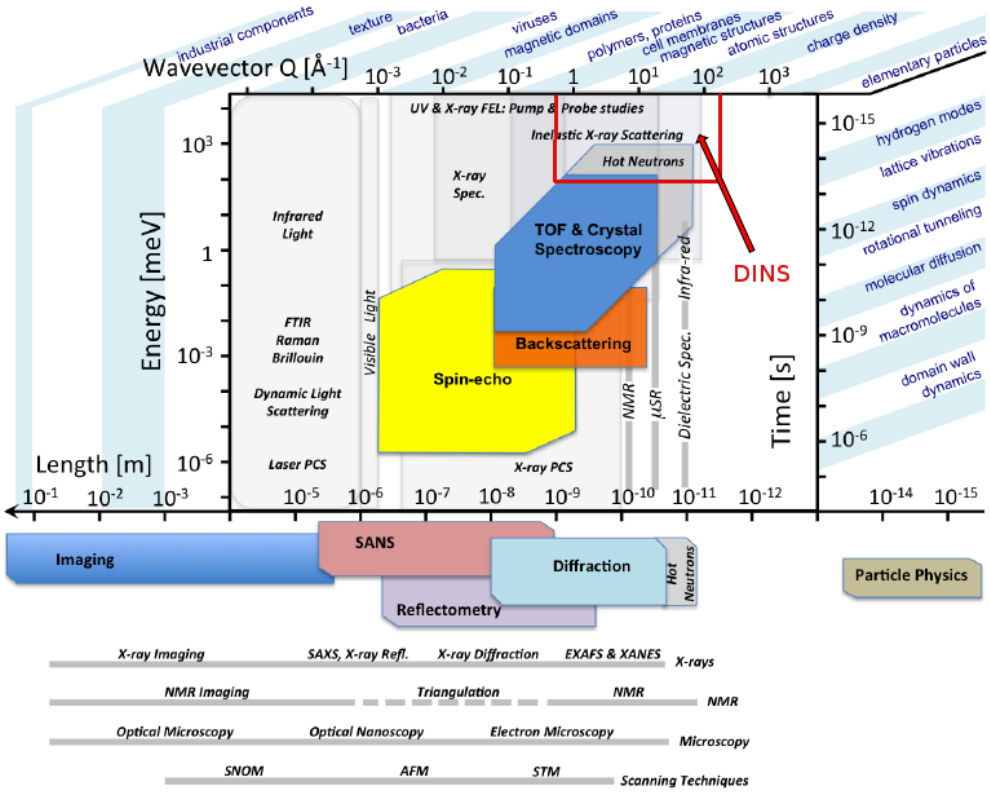

Figure 1.10: Neutron- and complementary techniques to explore different length- and time-scales. The experimentally accessible areas of various neutron-based methods available at the European Spallation Source (ESS) are shown as filled polygons in strong colors, except for the areas labeled as 'Hot Neutrons'. The red-edged region accommodates eV spectroscopy (at energies up to 10^6 meV), which is not avalaible at ESS. Reproduced from [35] with modifications.

While QENS is mostly intended to investigate diffusion, inelastic instruments tuned on energy transfers less than epithermal (Fig. 1.9) are aimed to explore both lattice and inter/intra-molecular modes in condensed matter with high resolution over wide regions of the (Q,E)-space, which remains a distinct asset of INS when compared to other spectroscopies[12] (Fig. 1.10) and the main driver for the construction and operation of large centralized neutron facilities across the globe [31].
When exchanged energies go epithermal (i.e., much greater than the binding energies of the scatterers) and momentum transfers span the region above 25 $Å^{-1}$, deep inelastic neutron scattering (DINS) routines take place (Fig. 1.11).
DINS is currently the only technique to *directly* probe quantum effects involving atomic nuclei (NQEs) through the mean kinetic energy, $< E_K >$, of the scatterers -

[12] As an early NMR and dielectric spectroscopist, let me stress the significant degree of overlap of NMR with neutron scattering, especially after the development of pulsed-field-gradient techniques (PFG NMR) to probe stochastic magnetic-relaxation processes with spatial resolution [33]. On the other hand, dielectric spectroscopy is able to probe dynamic processes over an unrivaled frequency range extending from 10^{-4} to 10^{10} Hz [34].

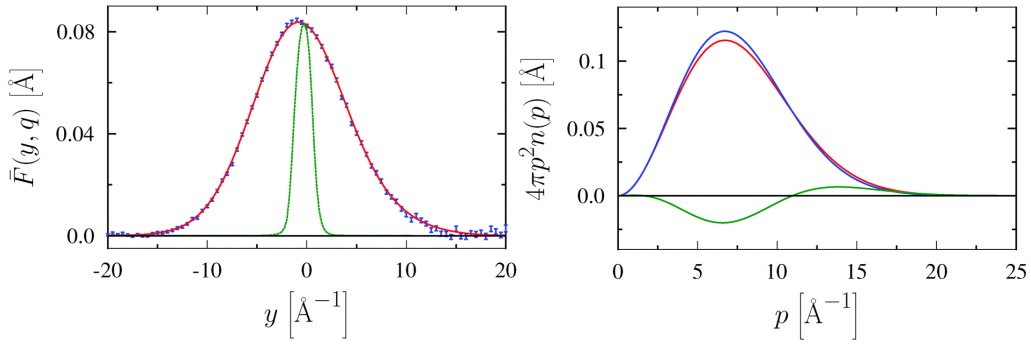

Figure 1.11: An example of the common outputs of a DINS experiment. Left: Angle-averaged neutron Compton profile (NCP) for hydrogen of water 2D-entrapped in graphene oxide (GO) sponges at 293 K (blue dots) + rescaled VESUVIO experimental resolution (green curve) + global fit of the angle-dependent NCPs using a 3D anisotropic Gaussian line-shape derived from a quasi-harmonic model (red curve). Right: Momentum distribution $n(p)$ for hydrogen of water 2D-entrapped in GO sponges at 293 K (red curve) + $n(p)$ for bulk water at 300 K (blue curve) + difference curve magnified by 3 (green curve). Reproduced from [36].

which is predominantly determined by the properties of the vibrational ground state - as well as any superposition of NQEs and anharmonicity of the local potential via the single-particle momentum distribution, $n(\mathbf{p})$, of the target particles, or, better, via possible deviations of its radial counterpart ($4\pi p^2 n(p)$) from the Maxwell-Boltzmann profile.

As to water, chemical interactions occurring in the bulk typically represent small changes in the energy of constituents, compared to the energy sequestered in the zero-point (ZP) motion of hydrogens[13].

In general, NQEs prove remarkable in this substance. For example, 'superstrong', Arrhenius-like behavior of low-temperature water ($T < 150$ K) in terms of T-dependence of the structural relaxation time[14] is a clear mark of NQEs in action. As well as water's astoundingly pronounced isotope effect for a range of physical and chemical properties [37].

The last decade has witnessed a major surge of activity in the study of bulk and confined water from the computational point of view [37]. In particular, the effective inclusion of NQEs in algorithms - with special focusing on competing quantum effects [39–43] - has paved the way for capturing most of the spectrum of properties of water and, in general, of any system containing light atoms.

On the other hand, in spite of the large range of techniques having access to NQEs (Table 1.1), only a smaller amount of experimental investigations is available to counterbalance the computational effort.

All that said, the systematic exploration by DINS of hydrogen's $< E_k >$ and $n(\mathbf{p})$ in

[13] Indeed, the ZP energy of the $O-H$ stretch is equivalent to a $\sim$ 2000 K rise in temperature along that coordinate [37].

[14] The fragility index $m = \left(\frac{dlog_{10}(\tau)}{d\frac{T_g}{T}} \right)_{T=T_g}$ for low-density amorphous ice (LDA) and amorphous solid water (ASW) has been recently assessed around 14 by dielectric spectroscopy, which is the lowest fragility known at present [38].

Table 1.1: Summary of major experimental techniques accessing NQEs in condensed matter. Cited literary selection is from the last 15 years and specifically refers to the topic of NQEs in water.

Technique	Avail. experiments
DINS	[44–46]
INS and DINS	[1, 47]
QENS	[48]
XRS and Compton scattering, XAS, RIXS	[49–52]
Raman, IR	[53]
X-ray and neutron diffraction	[54]
Microscopy	[55, 56]
Pump-probe laser spectroscopy	[57, 58]
NMR	[59, 60]
Dielectric spectroscopy	[61]

bulk water from low-T metastable phases to supercritical conditions can effectively depict the connection of the proton short-scale response to the ^1H-bond network dynamics. And the combination of this unique experimental tool with INS, which, conversely, scans transitions to the first excited state mainly within the harmonic frame (Fig. 1.12), can provide important additional experimental information about the nature of single-nucleus motions beyond the harmonic approximation.
All of this is far from being mere curiosity-driven research, since the applicative potential is large. Indeed, the topic of water polyamorphism influences many fields of investigation, such as biology (when explaining the structure and reaction of liquid water around organic macromolecules [62]); or geology (when studying polyamorphic transitions in water confined in clays and other porous materials [63]); or astrophysics (since it has been speculated that polyamorphic transitions in liquid and amorphous solid water may occur inside - or on the surface of - icy bodies in space [64]). On the other hand, the investigation of quantum-dynamic properties of supercritical water is likely to allow for breakthroughs in various areas, which include the quest for new solvation techniques demanded by nanotechnologies and commercial chemistry [65, 66], or the construction of generation-IV reactors, which use supercritical water as their coolant [67].
That's why the INS + DINS duo was selected as the technical gizmo of choice to perform the experiments on water described in the present monograph.

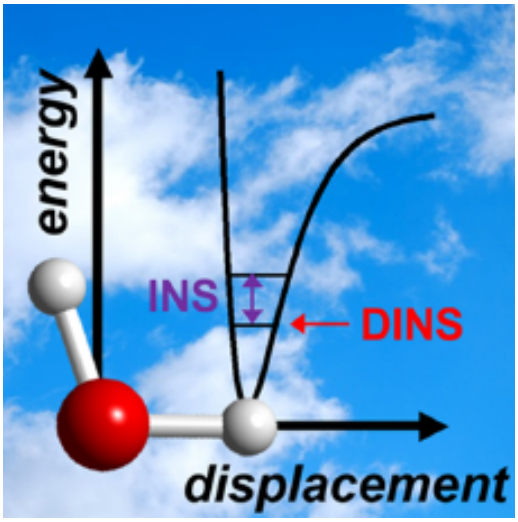

Figure 1.12: While DINS returns quantities influenced by the properties of the single-nucleus vibrational ground state irrespective of any approximation (apart from the impulse approximation guaranteed by very large values of energy and momentum transfers), INS gives back information about $0 \rightarrow 1$ energy transitions, whose interpretation is greatly simplified by resorting to a harmonic framework. Reproduced from [1].

2

Going metastable - Water amorphous ices

Perfectly ordered disorder designed
with a helter-skelter magnificence

Emily Carr

2.1 Amorphous solids

The amorphous solid state of matter has long proven a tricky topic in condensed matter physics [68] basically because of its lack of long-range order, which is commonly flagged by the appearance of extreme broadening in features observed by diffraction or various spectroscopic techniques.
Indeed, though still characterized by short-range order (i.e., tetrahedrality in water) just like crystals, in amorphous solids such order typically disappears at molecular distances of 20-50 Å [69]. This inherent disorder makes them thermodynamically metastable.
Amorphs are usually branched into two sub-families: so-called glasses and the remaining non-glassy materials. What makes glasses special is their thermodynamic link to the corresponding supercooled liquid state (see Appendix A).
The standard liquid constitutes a well-defined phase with constant and rapid interchange of atomic configurations by diffusion and structural relaxation processes, but relatively high degree of order in averaged local structures [70]. When thermal energy is removed from the liquid at a rate that inhibits nucleation and crystal growth, normal freezing into a crystalline configuration is kinetically hindered, so that the liquid phase metastably persists into a supercooled state that still maintains a local internal thermodynamic equilibrium. Yet, a temperature (T_g) is eventually reached at which equilibrium is no longer achieved: at this point a glass transition takes place towards a low-temperature, vitrified version of the liquid structure. This path can be walked through backwards.
Conversely, a non-glassy amorph is not expected to turn into a supercooled liquid during heating, but either it remains in the amorphous solid state or it crystallizes. This behavior is often explained in terms of 'nanocristallinity', i.e., the idea that the material is made of a huge number of nanosized crystal grains, each of which contains a few hundred molecules. Put this way, sharp Bragg peaks characteristic of crystals in scattering experiments are not observed because they are massively

broadened due to particle size effects.
Three distance ranges are usually defined for amorphous solids: the short-range order, which typically extends to the nearest neighbors of a central atom or molecule (first coordination sphere); the intermediate range order, encompassing the second to fifth-through-seventh coordination spheres, where the above-mentioned loss of order occurs; and the long range beyond, where no order persists.
An effective way to discern glassy from non-glassy amorphs consists of assessing how the short-range order disappears at intermediate ranges [71]. While this order vanishes more or less continuously in the glassy state by slow variation of interbond angles and interatomic distances, almost no variation is observed inside nanocrystals, with strong change at the intergrain boundaries instead.

2.2 Pressure-induced amorphization

Several techniques exist to prepare amorphous solids [72], but our attention is drawn here to the formation of an amorph directly from a crystalline material through the application of pressure, at a temperature below the melting point or glass transformation range. This is what's called 'pressure-induced amorphization' (PIA). In such a process, a crystal-to-amorph transition takes place when the crystalline structure is driven away from an equilibrium state and the formation of other possible crystalline phases gets kinetically hindered.
This phenomenon can be effectively described in terms of a configurational energy landscape (CEL), i.e., a multidimensional (3N-6 coordinates) potential energy surface determined as a function of the arrangements and interactions between system particles. Within the CEL, stable crystalline configurations are represented by a few deep, sharp minima, whereas most of the surface consists of families of shallower minima representing less well-ordered or amorphous states, separated by energy barriers and connected via different possible pathways.
Large classes of each amorphous type are grouped into so-called megabasins that are presumed to share some structural and thermodynamic commonality with the corresponding crystals and represent regions with short to intermediate range order, with stability areas separated by relatively low energy barriers. A polyamorphic[1] transformation would be associated with the system crossing the energy barrier between two megabasins (Fig. 2.1).
PIA was experimentally observed for the first time in 1984, when a seminal experiment by Mishima et al. [76] established that ice I_h has a negative melting slope as a function of pressure, which can be extended metastably below its melting line.
The application of pressure results in a phase transition to another thermodynamically stable state if the thermal energy of the system is enough to allow re-equilibration. Otherwise, the system gets trapped into some metastable state that

[1]Polymorphism is a long-lived notion concerning the occurrence of more than one crystal structure for a particular material, with no change in composition [73]. The phase diagram of stable crystalline polymorphs usually consists of various coexistence lines that, once crossed, are accompanied by sharp structural transitions, that is, a change of short-range order in the unit cell.

On the other hand, the parallel concept of polyamorphism is rather new [74], not so well understood, and recently attracting a lot of attention [75].

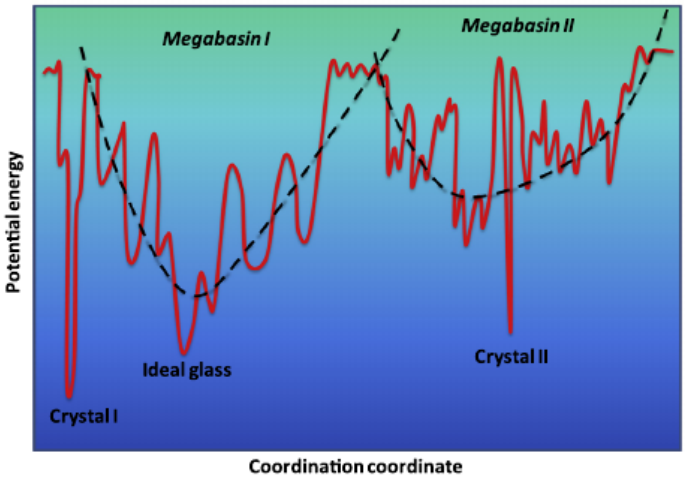

Figure 2.1: The CEL depicted as a 2D diagram where only one generalized configurational coordinate axis is considered. The two sharp, deep minima represent the most stable (I) and one metastable crystal (II) whereas the 'ideal glass' configuration appears as a broader minimum located above the potential energy of state I. Other amorphous configurations correspond to other broad minima, each located in the megabasin characterized by structural and thermodynamic similarity to the corresponding crystal. Reproduced from [77].

corresponds to an amorph. In this view, PIA could be depicted as a frustrated attempt of the metastably compressed crystal to seek a lower energy solution when no sufficient energy is given for bond breaking or atomic diffusion events that allow for nucleation and crystal growth.
Precisely, the occurrence of PIA means that a metastable amorphous state exists with an effective free energy lower than the one of the metastably compressed crystal. At sufficiently low temperature the crystalline transformation into the high-pressure (HP) polymorph is kinetically impeded and the compression of the low-pressure (LP) phase continues along a metastable extension of its compression path at $T < T_g$. This results in a direct transformation of the metastably compressed crystal into an amorphous solid (either thermal or mechanical[2]), that can be mapped onto a high-pressure, low-temperature version of the glassy state derived from the supercooled

[2] Any material possesses an intrinsic limit to its extension into a metastable regime, which is set by fundamental constraints related to its bond strengths and mechanical stability against applied stress. That's why a crystal cannot be compressed indefinitely without eventually experiencing some phenomenon, such as a vanishing resistance to strain or phonon/electronic instability. When this happens, the crystal can no longer exist and its free-energy curve terminates at a point known as the spinodal, beyond which the system must seek a new solution in terms of interatomic configurations.

Mechanical stability is governed by the so-called Born criteria:

$$\left[\frac{\partial \sigma_\perp}{\partial \epsilon_\perp}\right]_{T,C_{ij}} = \mu_T > 0 \qquad \left[\frac{-1}{V}\frac{\partial p}{\partial V}\right]_{T,C_{ij}} = B_T > 0 \tag{2.1}$$

where $\sigma_\perp$ and $\epsilon_\perp$ are the shear stress and strain parameters, respectively, while the C_{ij}s' are the shear elastic coefficients.

The violation of the Born criteria leads to a 'mechanical melting' that appears as PIA.

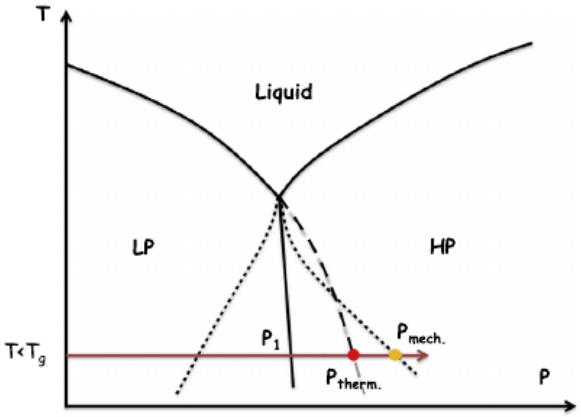

Figure 2.2: A scheme of PIA as a metastable melting event. The transition pressure P_{therm} corresponds to the intersection of the compression path of the LP phase with the extension of the melting line. Being $T < T_g$, the corresponding state is not liquid anymore but amorphous. If this transformation does not occur, the super-pressed LP phase may reach its spinodal limit (P_{mech}) and get mechanically unstable. Reproduced from [77].

liquid (Fig. 2.2). An analogous reverse argument can be applied to amorphization that results from the metastable decompression of a high pressure phase.

2.3 The case of water

Solid water amorphs have a long history.
The first experimental observation of what is nowadays known as amorphous solid water (ASW) - obtained by deposition of warm water vapor on a cold substrate - dates back to 1935 [78]. Since then many other amorphous ices (AIs) and preparation routes have been discovered, as exhaustively summarized in Table 2.1.
Let us focus on AIs obtained by PIA.
Upon compressing I_h [76] or I_c [79] at 77 K beyond 1.1 GPa, PIA takes place and high-density amorphous (HDA) ice gets formed. Nowadays, this specific amorphous solid is named unannealed high-density amorphous (uHDA) ice. If uHDA is annealed at $0.1 - 0.3$ GPa, another state of the HDA family appears, which is called expanded HDA (eHDA) [80]. Otherwise, if it is annealed up to $T > 160$ K at $p \geq 0.8$ GPa, a structurally distinct new state can be produced, known as very high-density amorphous (vHDA) ice [81]. Again, if uHDA is heated up to $T > 115$ K at ambient pressure, another structurally different amorph is recovered, named low-density amorphous ice I (LDA-I): this transition is accompanied by a release of heat and an expansion by $\sim 25\%$ [76,82]. Alternatively, LDA can be produced by decompressing vHDA to ambient pressure in the narrow temperature range $139 - 140$ K [83]: this member of the low-density family is termed LDA-II.
Other routes to the above-mentioned amorphs exist (see Table 2.1). Furthermore, LDA can be equally recovered from high-pressure ice VII and VIII [75] (Fig. 2.3).

Table 2.1: Summary of bulk amorphous water ices currently described in the literature. Ices produced by the influence of high-energy radiation on crystalline ice are not listed. Reproduced with modifications from [75].

Family	Name	Route of preparation	Density/$\frac{g}{cm^3}$
LDA	ASW	Water vapor deposition	0.94
	HGW	Cooling of liquid droplets at 10^7 $\frac{K}{s}$	0.94
	LDA-I	Heating of uHDA to 130 K at < 0.1 GPa	0.94
	LDA-II	Decompression of vHDA to ≤ 0.05 GPa at 140 K	0.94
HDA	uHDA	Compression of I_h to > 1.2 GPa at 77 K	1.15
	eHDA	Annealing of uHDA to 130 K at 0.18-0.30 GPa	-
		Decompression of vHDA to 0.07 GPa at 140 K	1.13
		Compression of LDA to > 0.4 GPa at 130-140 K	-
	rHDA	Annealing of uHDA at 0.3-1.9 GPa	-
vHDA	vHDA	Annealing of uHDA to > 160 K at ≥ 0.8 GPa	1.26
		Compression of LDA to ≥ 1.2 GPa at ≥ 125 K	-
		Compression of I_h to ≥ 1.2 GPa at ≥ 130 K	-

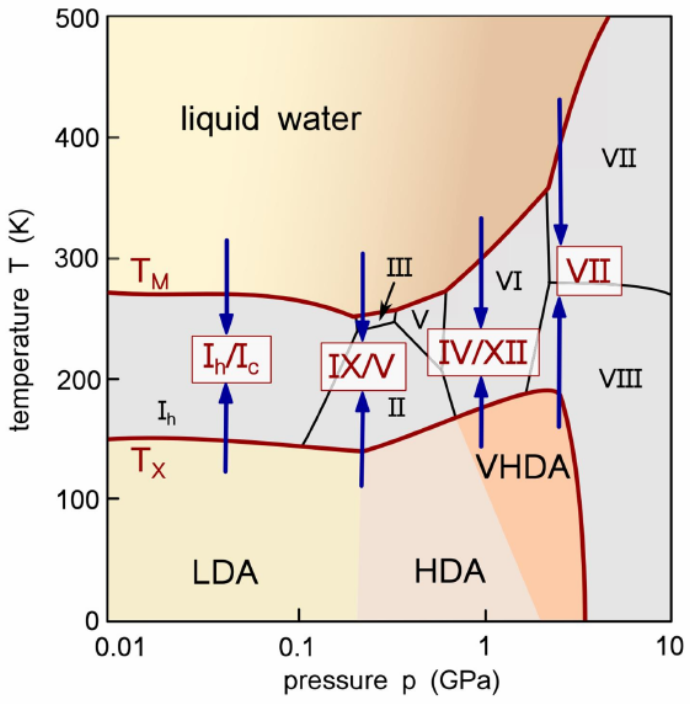

Figure 2.3: A schematic view of the low-temperature portion of the phase diagram of water. Reproduced from [84].

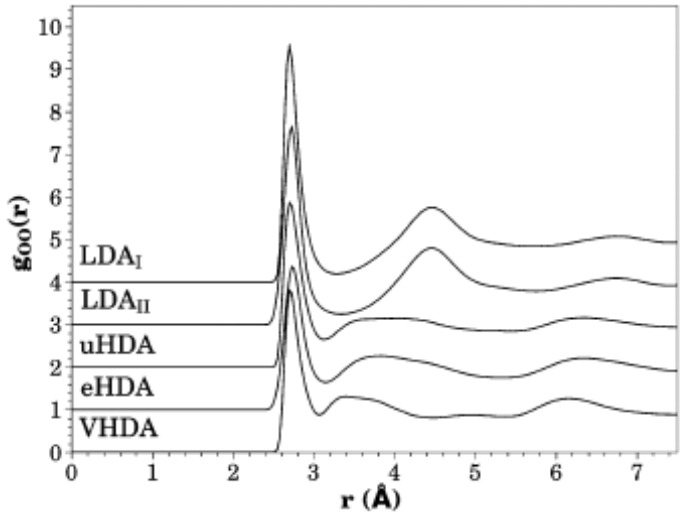

Figure 2.4: O-O radial distribution functions for five different water AIs. Reproduced from [75].

As explained in the previous paragraphs, compared to their crystalline counterparts, water-AI structural families cannot be told apart from each other by means of space-group or long-range-ordering criteria. Structure factors and radial distribution functions (RDFs) can be utilized instead in order to analyze the short- and intermediate-range ordering in these amorphs (see Appendix B).
Fig. 2.4 shows a set of five O-O radial distribution functions of various water AIs. A clear similarity exists between the $g_{OO}(r)$ functions of LDA-I and LDA-II, as well as those of uHDA and eHDA. On the other hand, the $g_{OO}(r)$ of vHDA neatly differs from the remaining ices.
The information retrieved from Fig. 2.4 in terms of local coordination is that all water ices are bonded to four approximately tetrahedrally disposed neighbors (the 'Walrafen pentamer'), but the HDA category holds an additional molecule (at a similar distance) not directly H-bonded to the central one and located in between its first and second coordination shell, while vHDA holds two (Fig. 2.5). This picture has been recently corroborated by simulation [85].
Indeed, the first-neighbor coordination number, as calculated by integration over the first peak of the $g_{OO}(r)$ curve, is 4 for LDA, 5 for HDA and 6 for vHDA. These additional molecules are termed 'interstitial', since they appear as a 'surplus' compared to what one might intuitively expect for the essential underlying random network structure of the AIs. This is coherent (though counterintuitively when the issue is thought of in terms of bulk density[3]) with a longer average O-O distance between H-bonded molecules for vHDA (2.85 Å) than for HDA (2.82 Å), and an even shorter distance for LDA (2.77 Å) [81, 87].
The issue of HDA and vHDA either being distinct amorphous ices or belonging to

[3] This phenomenon is a typical example of the pressure-coordination rule (with increasing pressure an increase of the coordination number takes place) and the consequent pressure-distance paradox (when the coordination number increases according to the previous rule, the interatomic distances also increase) [86].

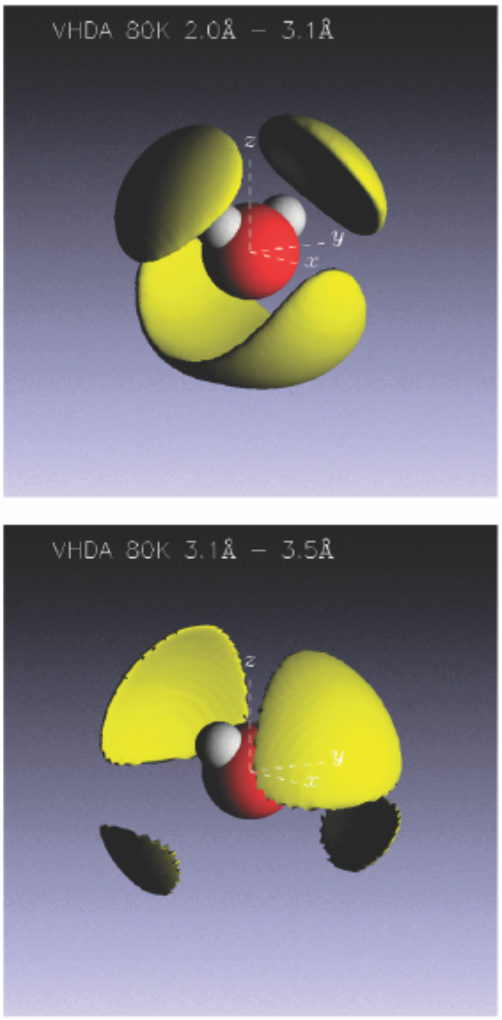

Figure 2.5: Top panel: tetrahedrally arranged first shell of water molecules in the O-O distance range $2.0 - 3.1$ Å in the vHDA structure as generated from EPSR refinement of isotope substitution neutron diffraction data. Bottom panel: interstitial shell in the distance range $3.1 - 3.5$ Å in the same structure (region of the O-O RDF into which the second-neighbor molecules get pushed as the density increases). The two upper large lobes show where interstitial water molecules would sit relative to the central one, whereas the two smaller lobes correspond to where non-bonded molecules would be if the central one is sitting in an interstitial site. Reproduced from [75].

the same energy megabasin has been long debated.
Fig. 2.6 reports the trend of the densities of well relaxed[4] amorphous ices as a function of pressure. Three distinct linear regimes can be spotted in connection to the three general AI families. As a support, Fig. 2.7 is a 2D-CEL synthesis of a large number of experiments concerning the mutual transformations of the AI families into one another upon changing T at different pressures. The energy landscape comprises only two megabasins at ambient pressure (namely LDA and HDA) and 1.2 GPa (namely HDA and VHDA), but three distinct megabasins at 0.5 GPa.
But precisely, what objective criterion has to be used in order to make a distinction between two different AI states?
One possibility is the existence of first-order-like transitions between the two states, that is, discontinuous changes in thermodynamics properties. Such transitions should also be reversible in some $T - p$ range and accompanied by the coexistence of the two amorphs in a single sample, otherwise the sudden change in thermodynamic properties could just be the result of abrupt relaxation in a single amorphous solid [88]. This way one would conclude that only two different amorphous states exist in water, LDA, and HDA, vHDA being a relaxed form of HDA.
Yet, the amorphous state has an intrinsic non-equilibrium nature. This means that a structural relaxation is always superimposed to the main transition, so that the latter may appear sharp and discontinuous, in fact being sharp, but continuous. Or, alternatively, an apperingly continuous transition might in fact be a first-order one smeared by relaxation effects, so emerging as discontinuous only at higher temperatures. That's why another criterion is implicit in the IUPAP definition of phases, that is, considering transformations accompanied by sudden, but not necessarily discontinuous, changes in thermodynamic properties. These transformations must also be reversible, but not necessarily accompanied by the coexistence of two distinct AIs, which should nevertheless show different thermodynamic properties, such as heat capacity and compressibility. With this choice, one must conclude that water is characterized by three AI states, namely LDA, HDA, and vHDA, as an addition to the 16 different crystalline phases - either stable or metastable, either proton-ordered or disordered - that have been discovered so far.
The neutron scattering experiments described in this monograph have contributed to further clarify this intriguing matter [1].

2.4 Are water AIs glassy?

In other words, are water AIs continuosly connected to the corresponding supercooled liquid by a glass-to-liquid transition? Or must they be regarded as distorted crystalline phases, nano-crystals, or crystal-like states?
From an experimental point of view, answering these questions proves a very hard task, since the AIs crystallize very rapidly above the crystallization temperature

[4]Amorphous materials (especially glasses) usually undergo a slow, T-dependent structural relaxation (the rate of which becomes significant - minutes or seconds - only in the proximity of the glass transition temperature).

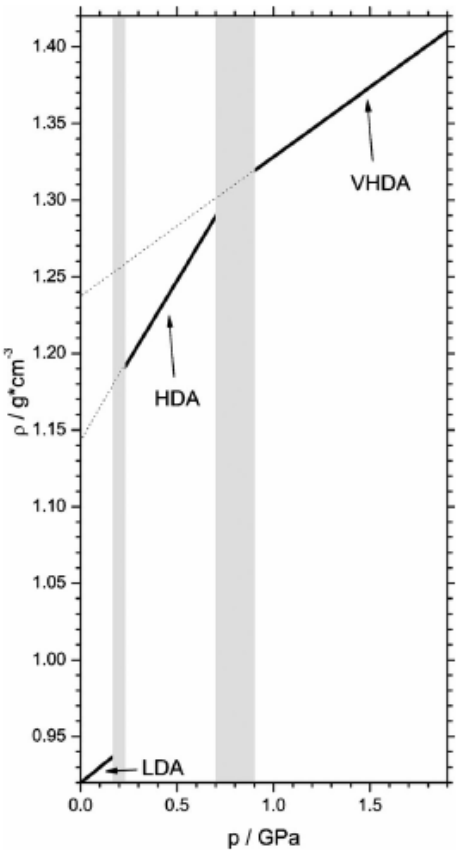

Figure 2.6: A scheme of the densities of well-relaxed water AIs close to the temperature of their crystallization. Grey zones represent the transition regions between one state and another. Reproduced from [75].

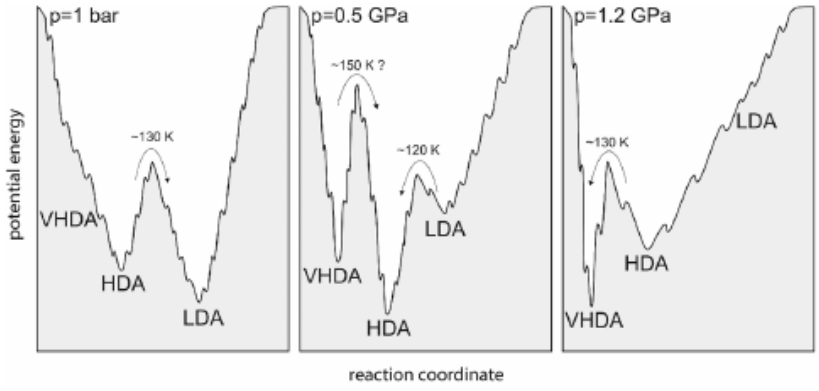

Figure 2.7: Simplified scheme of the changes in the 2D CEL of the AI families upon changing the operational pressure. The order of stability mirrors experimental findings. Crystalline polymorphs are omitted for clarity. Reproduced from [75].

T_X ($140 - 190$ K, depending on applied pressure), whereas the supercooled liquid promptly crystallizes upon cooling below the homogeneous nucleation temperature T_H ($181 - 235$ K, depending on p) [89]. The $30 - 40$ K gap between T_H and T_X is the so-called 'no-man's land', where non-crystalline bulk water cannot be observed on timescales exceeding 1 s (Fig. 1.4). Indeed, extremely refined ultrafast-cooling techniques ($\geq 10^7$ $\frac{K}{s}$) to produce micrometer-sized[5] droplets of water cooled below T_H [19] are needed to explore the matter. For AIs commonly produced via alternative routes - especially for those requiring PIA of crystals in the course of their preparation (such as HDA) - the issue is really hard to manage.
Alternatively, one may think of employing ultrafast heating of the amorphous solid. This has been out of reach so far, even though ultrarapid calorimetry methods (order of 10^5 $\frac{K}{s}$) exist to study whether a glass transition can be observed prior to crystallization and/or transformation to other amorphous ices [91, 92]. This glass transition would lead to an ultraviscous liquid state, called deeply supercooled liquid water.
As to LDA, the point is debated.
In the 80s' it has been postulated that hyperquenched water undergoes a glass-to-liquid transition just before the onset of crystallization to ice I [93]. Various experimental studies have been presented in favor of this scenario [94–96]: for example, differential scanning calorimetry (DSC) recorded from an LDA-II sample prepared from isothermal decompression of vHDA would look consistent with a real - yet very feeble (increase in heat capacity of about 1 $\frac{J}{Kmol}$) - glass transition at approximately $T_g = 137$ K, with calorimetric signatures highly similar to the ones typical of hyperquenched glassy water (HGW) [96].
On the other hand, it has been argued that the true glass-to-liquid transition should be located at considerably higher temperatures (and therefore difficult to access experimentally) [97], while a third scenario would call for the kinetic unfreezing of the reorientation dynamics of the water molecules in order to explain the step in heat capacity observed upon heating LDA [98], as also supported by the similarities in endothermal features observed between LDA-I and pure crystals (namely, ice IV, V and XII) [99]. This would imply no existence of a true glass transition in the sense of a transition from the glass to the highly viscous liquid, in which the molecules undergo translation diffusion processes.
At a first glance, the claim that at least LDA-I is only a defected form of a crystal would seem corroborated by a set of vibrational densities of states (VDoS) for LDA-I, uHDA, I_h and I_c, respectively, recovered by Tulk et al. [100] by inelastic neutron scattering (no boson peak[6] for LDA-I and crystals, even at 5 K).
Pressurized AIs offer no less controversies.
In the late 90s' a crystal-like nature was suggested for the HDA family on the basis of inelastic neutron and X-ray scattering experiments highligthing similarity

[5] That is, droplets of bulk water. Indeed, using nanoscopic volumes of water, where surface effects become significant, makes the thermodynamic relevance to bulk water unclear [18, 90].

[6] Crystalline and glassy materials of the same composition behave differently at low temperature, particularly as related to heat capacity, thermal conductivity and the VDoS $g(\omega)$ (usually in the range $2 - 10$ meV at low T). Above 1 K, for example, a prominent difference is that many amorphs exhibit a non-Debye character ($g(\omega) \propto A\omega^2$ in the limit $\omega \to 0$), which likely results from an excess phonon density of states in the low frequency region. This phenomenon is termed a boson peak.

to high-pressure crystalline polymorphs [101–103]. More recently, Tulk et al. [100] caught a low-T boson peak for uHDA in the VDoS; Mishima estimated the glass transition temperature of HDA for emulsified water as increasing from about 140 K near ambient pressure to 190 K at 1 GPa by calorimetry [104]; whereas, according to [89], Andersson [105] would have even mistaken vHDA for HDA in his dielectric measurements, actually discovering a different glass transition placed 50 K below the one extrapolated by Mishima for HDA at the same operational pressure. This would call for both HDA and vHDA being glasses, and corroborate the concept that HDA and vHDA need to be regarded as two distinct polyamorphic states.

3

Going no-boundary - Supercritical water

Some like it hot

Tony Curtis

3.1 A matter of words

What's exactly a fluid? Literally a substance that continually flows under an applied shear stress with no retention of its shape. That is, a concept encompassing both liquids and gases.
In this view, it's no surprise that water placed at pressures and temperatures exceeding the critical values in the $p - T$ plane is termed a supercritical (SC) fluid, since, according to textbooks, across such region isothermal and isobaric properties change continuously and the features of the material are somehow intermediate between those of a liquid and a gas in terms of density, viscosity and diffusion coefficients[1] [107].
As ever, the peculiarities of the SC domain with respect to the non-critical one are basically ruled by the progressive distortion and disruption of the H-bond network as supercritical pressures and temperatures are approached. According to various IR and X-ray Raman investigations [108–110], moving towards high temperatures along an isobar or towards low pressures along an isotherm causes the (actually slow) disappearance of tetrahedral coordination and oligomers in favor of monomeric water, with significant repercussions on the features of vibrational spectra, especially in terms of both the symmetric and asymmetric stretching band, as well as the librational one (Fig. 3.1).
Most frequently, in a schematic phase diagram the SC region is assumed to lie for $T > T_c$ and $p > p_c$ (Fig. 3.2), with no observable able to make a distinction between different subdomains.
Yet, that's not the whole story.

[1] A delightful video showing water going through its supercritical phase transition along an isochore in a hydrothermal diamond anvil cell [106] can be found at https://www.youtube.com/watch?v=29oy1UCHJIE .

At first, boiling is shown, but at 1:08 min the phase boundary between water vapor and the liquid just disappears while the system is undergoing a supercritical phase transition. Phase separation into liquid + gaseous water is then shown again.

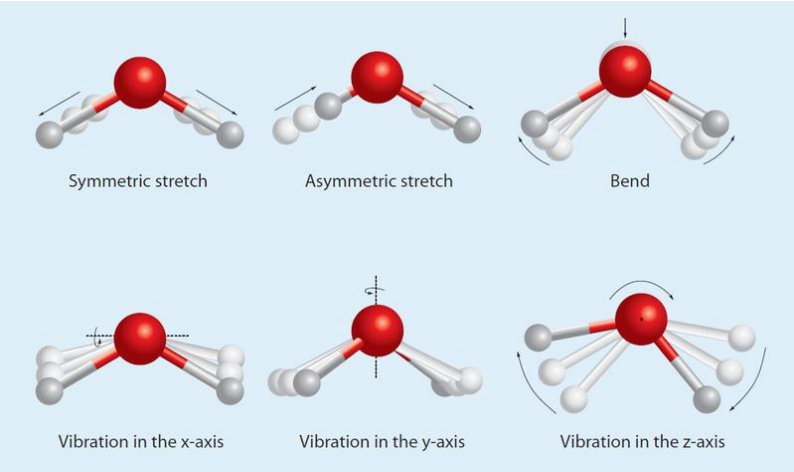

Figure 3.1: A sketch of vibrations in the water molecule: in the top row symmetric and asymmetric stretching, as well as bending; in the bottom row the three possible librations (hindered rotations). Reproduced from https://skcchemistry.wikispaces.com/Infra+red+Spectroscopy .

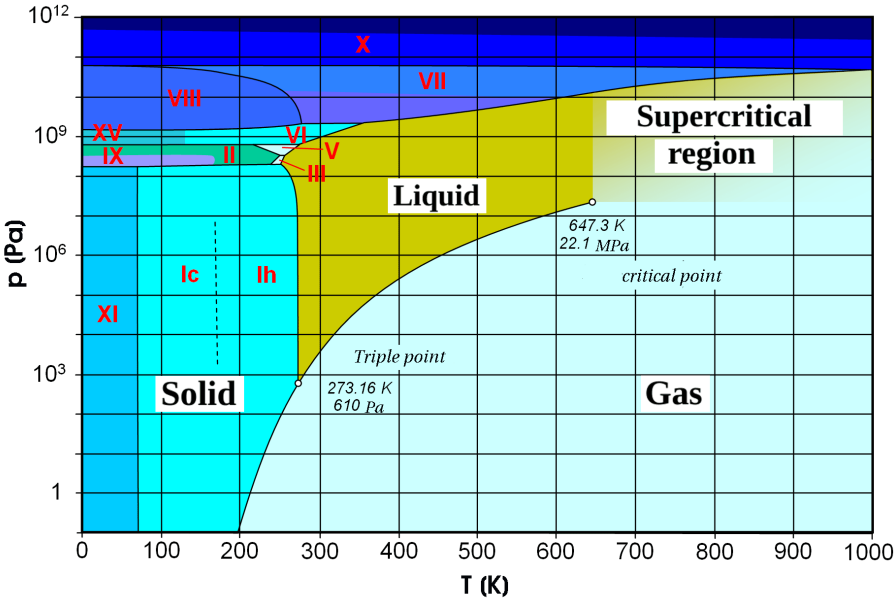

Figure 3.2: Large-scale phase diagram of water. Amorphous states are not reported. Reproduced from http://www.mrbigler.com/moodle with modifications, under a Creative Commons Attribution-ShareAlike 3.0 Unported License.

3.2 The Widom line

For water and other supercritical fluids, the SC region is actually characterized by a peculiar behavior of many thermophysical properties.
Indeed, the correlation length[2] ξ for thermodynamic fluctuations diverges at the critical point (CP) [111], and near the CP a critical behavior is observed for a number of response functions ruled by the second derivatives of the Gibbs thermodynamic potential (such as the isochoric heat capacity C_V and its isobaric counterpart C_p, as well as the isothermal compressibility κ_T or the isobaric thermal expansion α_p), which are experimentally seen to go through extrema and show proportionality to a power function of ξ. This is also the case for density fluctuations $\zeta_T = \frac{<(\Delta N)^2>}{<N>} \sim \left(\frac{\partial \rho}{\partial p}\right)_T$ [112].
Such extrema reside on a set of *loci* - named 'Widom lines' by Eugene Stanley [14] in honor of Benjamin Widom - that merge asymptotically into a single curve[3] (scaling region) when approaching the liquid-gas CP (LGCP) and get more and more distant from one another as one goes several dozen percent away from it. (Fig. 3.3). These 'ridges', which are markedly pronounced around T_c and p_c, become flatter and flatter as the distance from the LGCP is enlarged (see Fig. 3.4 for an example about water's C_p and ρ), actually getting severely blurred at very large temperatures and pressures. Indeed, if one takes a look at Fig. 3.5, the difference of most thermodynamic properties between the fluid states marked by points A and B are much smaller than between those marked by B and C, although B and C are in the supercritical region, whereas A is outside. The same is true for the B–C–D sequence. In fact, the density hardly changes when the traditional supercritical borders are crossed, dropping suddenly by a half for a move within the supercritical region (B to C) [114].
Here's why getting exhaustive experimental information about the SC zone is not a matter of pure academic interest, but crucial from a technological point of view: for example, considering that generation-IV SC-water-cooled nuclear reactors should work in the pressure range $25 - 30$ MPa (i.e., in the proximity of the CP), great attention must be paid to those parts of the system where Widom conditions might be fulfilled, since attempts to control temperature and pressure around a sharp peak might lead to uncontrollable oscillations of the thermodynamic parameters and safety problems [114].
Though Widom lines signaling no 1^{st}-order transition, they are nonetheless thought

[2] If $m(\mathbf{r})$ is the order parameter of a system that undergoes a 2^{nd}-order phase transition when crossing a certain critical thermodynamic point, the correlation function that represents the 'memory persistence' of the spatial fluctuations in the density of $m(\mathbf{r})$ can be defined as

$$\Gamma(\mathbf{r}) =< m(\mathbf{r})m(\mathbf{0}) > - < m(\mathbf{r}) >< m(\mathbf{0}) > . \tag{3.1}$$

The functional form of Γ is $\sim \frac{e^{-\frac{r}{\xi}}}{r}$, where ξ is the associated correlation length, i.e., the typical length scale of fluctuation correlations.

[3] The temperature where all Widom lines converge usually gives an experimental upper limit of the critical temperature T_c.

Interestingly, in [113] Gallo et al. report a perfect superposition of the C_p, α_p and κ_T lines for water in a scaling region whose range extends circa 30 K and 90 bar above the liquid-gas CP, for both experimental data and simulations made via TIP4P/2005 potential, which, among all models available, returns values of T_c and ρ_c closest to the experimental findings.

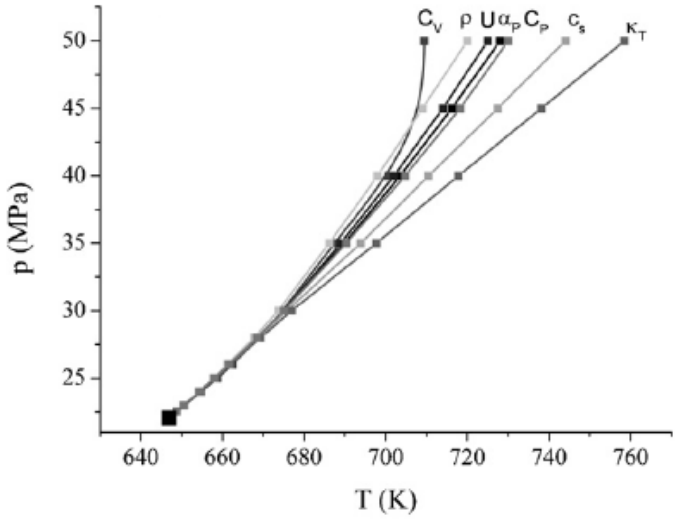

Figure 3.3: A set of Widom lines starting from the critical point of water. Reproduced from [114].

to cause a partition of the supercritical region into sub-regions characterized by different dynamic regimes reminiscent of their parent non-critical phases. A recent work by Simeoni et al. [116] tried to extrapolate the Widom lines for argon into the deep-supercritical region ($p > 1$ GPa) on the basis of experimental data on the positions of the maximum of heat capacity in the isotherms, thus finding a sharp transition in the velocity of nanometric acoustic waves in getting from one subregion to the other, which are termed liquid- and gas-like, respectively. This extrapolation has been somehow argued by Brazhkin et al. [112], due to the maxima of C_p to get severely smeared out at very large temperatures and pressures.

3.3 The Frenkel line

In order to univocally tell apart a 'true' solid-like liquid from a quasigas-like fluid at superhigh pressures, in [112] a dynamic (rather than thermodynamic) criterion is introduced, based on the assumption that in a liquid, as temperature is increased, the relaxation time τ^* between two particle-jumps[4] eventually gets comparable to the period τ_0 of particle vibrations around a local equilibrium position, thus making the time-ruled discrimination between vibrational and hopping behavior disappear. When $\tau^* < \tau_0$, a transition to the ballistic-collision diffusion regime (typical of gases) occurs.
The condition $\frac{\tau*}{\tau^0} \sim 1$, therefore, serves as an effective (smooth) dynamic crossover condition between a rigid-liquid regime to a quasigas soft-fluid one, especially in terms of shear resistance. This condition defines a new curve - named the 'Frenkel

[4] In liquids, the interaction energy is relatively large at low temperatures and the diffusion process, just as in crystals and glasses, is determined by activated jumps of atoms and molecules (vibrational hopping transport) [112]. Within any time interval between two jumps, any particle (harmonically) vibrates near a local equilibrium position.

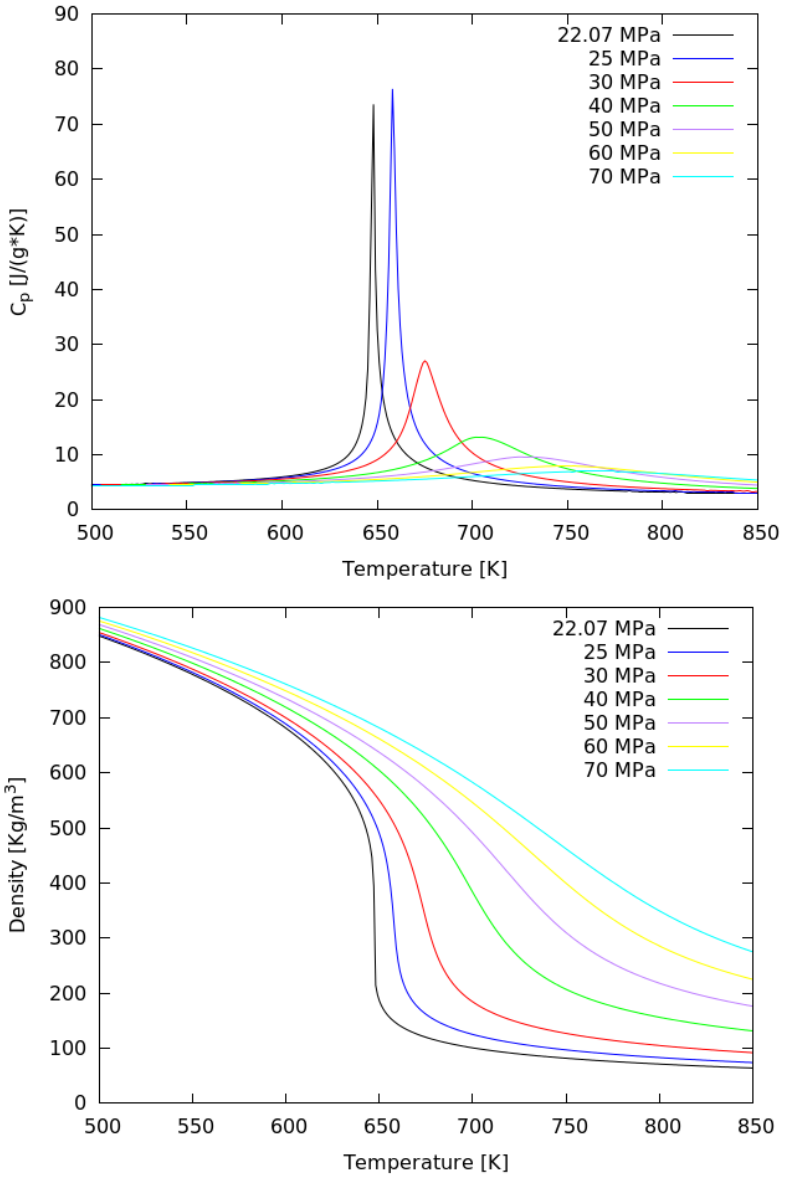

Figure 3.4: Maxima of C_p (top panel) and density (bottom panel) for SC water, calculated with the IAPWS reference equation of state [115] from NIST data. Notice the characteristic peak of C_p at 25 MPa. Generated via Gnuplot 4.6.

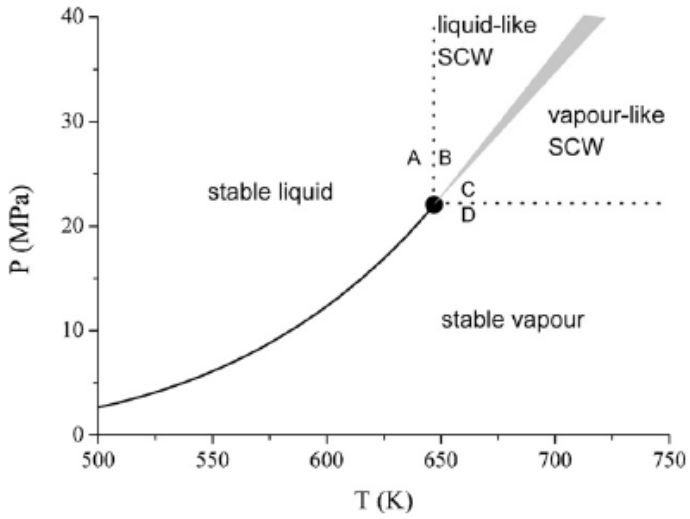

Figure 3.5: A sketch of water's sub- and supercritical domains around the critical point. Reproduced from [114].

line' after Yakov Frenkel (Fig. 3.6) - which is considered sort of 'true Widom line' and in the proximity of which also the thermodynamic functions exhibit specific features, basically due to the disappearance of transverse-phonon type excitations in the short-wavelength part of the spectrum as T and p get higher and higher.
Being not formally related to the liquid-gas transition, the Frenkel line has a universal nature, since it can exist for systems in which the liquid-vapor coexistence curve and the CP are absent (such as some colloidal system).
As a rigorous tool to spot the dynamic crossover in the phase space, the velocity autocorrelation function (VACF) $z(t)$ is suggested (see Appendix C), since a transition from an oscillatory/decaying behavior (typical of liquids and solids near melting) to a monotonic decay (typical of gases) should be observed in passing from the liquid-like to the quasigas-like region [117].
An alternative route is monitoring the diffusion coefficient.
Being the average time of a jump to a distance equal to the interparticle spacing, in a random-walk model τ^* is related to the diffusion coefficient D for the liquid by

$$\tau^* \sim \frac{a^2}{6D} \tag{3.2}$$

where a is the average shortest interparticle distance [112].
Then, condition $\frac{\tau*}{\tau^0} \sim 1$ can be rewritten

$$D \sim \frac{a^2}{6\tau_0}. \tag{3.3}$$

At moderate pressures ($p < (5-10)\ p_c$), the compression of the fluid in the region of quasigas density mainly occurs due to a decrease in the 'free' volume, and τ_0 changes only slightly. While reaching $10^2\ p_c$ the magnitude of τ_0 changes by no more than several dozen percent, whereas D changes by several orders of magnitude in the range from the melting point to the Frenkel crossover temperature.

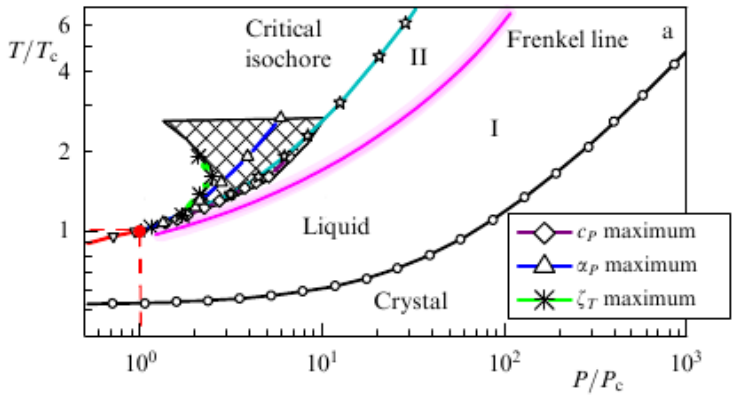

Figure 3.6: Simulated positions of the Frenkel- and various Widom lines in the $p-T$ plane for a Lennard-Jones system. The Frenkel line separates the liquid-like region I from the quasigas-fluid region II. Reproduced from [112].

The magnitude of a^2 also changes insignificantly in the above mentioned range of pressures, whereas both τ_0 and a^2 decrease with increasing pressure, which means that the ratio $\frac{a^2}{\tau_0}$ is modified to an even smaller extent.

Therefore, in the moderate-pressure range, the locus of constant diffusion coefficient can be selected as the conditional line that separates a rigid liquid from a soft, quasigas fluid[5]. If D_c is the magnitude of the diffusion coefficient in the CP, the line determined by the condition

$$D = D_c \tag{3.4}$$

will approximately[6] represent the dynamic continuation of the curve of the LG equilibrium. Across this dynamic line the temperature dependence of the diffusion coefficient - as well as of τ^* itself - changes from exponential ($D \sim e^{-\frac{E_{act}}{k_B T}}$) to power-law ($D \sim T^\alpha$, where α is an index close to $\frac{1}{2}$ and weakly dependent on T).

The reliability of this latter approach has been recently confirmed via TIP4P/2005 simulation [113], which reports strong changes in the slope of D-lines along the isobars in the region close to the Widom line at low pressures.

[5]Brazhkin et al. [112] point out that the condition of constant viscosity, in contrast to the one of constant diffusion, cannot be used as an approximation for the crossover line, since η is not only inversely proportional to D, but also proportional to temperature and rapidly increasing with compression along the line of constant diffusion. As a result, the lines of constant η should move into the region of smaller densities as T gets higher, even reaching the domain of small (down to zero) pressures.

[6]Indeed, the condition $\tau^* \sim \tau_0$ corresponds to an extended crossover, and the relation of the start-point of the dynamic line to the CP is arbitrary. Further, the change in the ratio $\frac{a^2}{\tau_0}$ cannot actually be neglected at very large pressures [112].

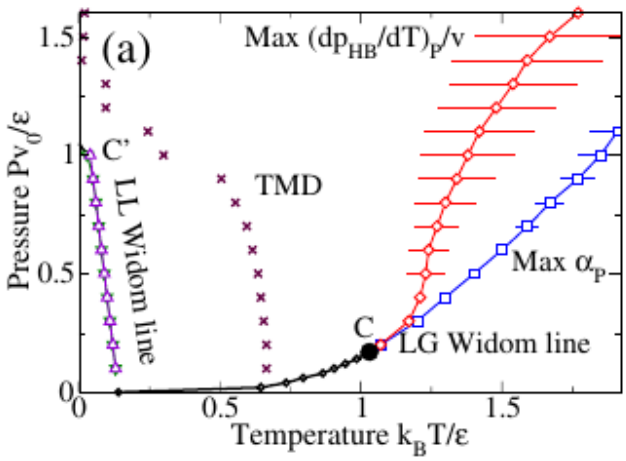

Figure 3.7: The mean-field $p - T$ diagram of a Hamiltonian model presented in [118] showing a set of Widom lines that emanate from the LGCP C and the LLCP C', respectively. p_{HB} is the probability of forming a normal hydrogen bond with local tetrahedral order. The TMD is the line of temperature of maximum density. Reproduced from [118].

3.4 The AIs and supercritical water: which possible connections?

As remarked in the Introduction, one of the possible thermodynamic scenarios to picture water anomalies is the LLPT hypothesis proposed by Poole et al. in 1992 [13] (Fig. 3.7).
Unlike other network-forming substances, water behaves as a fragile material within the experimentally-accessible liquid domain [12, 119]. Based on analogies with other network-forming liquids and with the thermodynamics of the AIs, it has been suggested that, at ambient pressure, liquid water should show a crossover between fragile behavior at high T to strong at low temperatures [97, 120], in the deep supercooled region of the phase diagram below the homogeneous-nucleation line.
This fragility transition is interpreted as arising from crossing the Widom line that emanates from the LLCP [14], which suggests a relation - consistent with expectations from the Adam-Gibbs model of glass-forming liquids [121] - to the behavior of C_p, and the fact that enthalpy or entropy fluctuations may have a strong influence on the dynamic properties of the system (see Appendix A).

3.4.1 Cage effect vs heterogeneity

One typical feature of glass formers is the severe slowing down of dynamics near the glass-transition point (with the time dependence of the relaxation functions changing from exponential to stretched exponential). This feature is shared by other classes of phenomena, for example criticality[7].

[7]Thermodynamic critical behavior is by now well understood and fits into robust frames such as the Ginzburg-Landau theory or renormalization-group formulation. Its dynamic counterpart is

Despite this apparent similarity, these two topics have been long believed disengaged, since either no intrinsic equilibrium nature can be ascribed to the glass phase or, unlike glass formers, no dynamic slowing down at a molecular level occurs for critical systems.
Intuitively, the kinetic arrest experienced by glasses could be related to a 'cage effect' (literally, a molecular-surroundings effect), which is already present in the normal liquid but should become more pronounced at lower temperature, due to cage restructuring in a more and more cooperative manner. However, the apparent stretching of the relaxation functions can also be explained by spatial heterogeneity, with relaxation occurring exponentially in each spatial domain, and the establishing of a complex hierarchy of relaxation times that are different in each domain [122]. Such heterogeneity would call for the existence of fluctuations and a diverging length scale[8] also for glass formers.
The issue is highly debated.
One puzzling feature concerning the origin of dynamic heterogeneity is the static structure factor $S(\mathbf{Q})$ (or the radial distribution function $g(r)$) showing very small changes across T_g, which would apparently signal the absence of a mesoscopic structure (with no room for spatial density correlation) [123]. The physical factors controlling the link between the growing dynamic correlation length and the slowing down of the structural relaxation near T_g remain, in fact, elusive.
That said, with the scientific landscape still lacking robust bulk-water experiments able to cross the hypothesized LL coexistence line and measure a sudden discontinuity in the local density of the system [18], the study of the Widom line above the LGCP could represent a useful way to get ideas about the inaccessible part of the supercooled phase diagram of water, so returning further information on the 'vitrified forms' of the two supposed low-T liquids, namely LDL and HDL.

more complicated to manage, even though all important concepts (universality, scaling properties, crossover phenomena) are preserved. For this latter class of events the existence of critical slowing down (i.e., the divergence of the characteristic relaxation time τ_c when one approaches the critical point) has been recognized, as well as of a separation of timescales, even though no exact understanding of how the diverging correlations of the static fluctuations affect the transport coefficients has been reached yet.

[8] For example, Sillescu [122] proposes a simplified treatment of energy fluctuations at constant volume, based on a set of *ad hoc* assumptions (existence of independent metastable subvolumes of equal size V_{SV}, each with its own T_g and relaxation time; Gaussian distribution of subsystem fluctuating variables, with $< \Delta E^2 >= k_B T^2 C_V$; decoupling of the vibrational energy of the glass from the component due to the slowing-down process; energy difference between two subvolumes proportional to the temperature difference, and its square related to $< \Delta E^2 >$), thanks to which he derives the relation $\xi = V_{SV}^{\frac{1}{3}}$.

4

A special cue game - Inelastic neutron scattering

Stroke it, don't poke it

Billiards saying

4.1 Don't lose your memory

A common way to characterize the statistical relationship between two variables A and B is defining a joint probability distribution, $P(A, B)$.
Nevertheless such a statistical relationship can also emerge from moments of $P(A, B)$. From this point of view, an important quantity is the so-called (cross) correlation function $C_{AB} =< AB >$, which returns the extent to which A and B depend the same way on a common internal variable, most often time or space.
In case no statistical relationship exists between the two distributions, then they are uncorrelated and $< AB >=< A >< B >$.
No coincidence that the quantity $< AB > - < A >< B >$ just returns the covariance of A and B, which is a traditional measure of how much the two random variables change together, and whose normalized version is the well-known Pearson's correlation coefficient

$$\rho_{AB} = \frac{< AB > - < A >< B >}{\sigma_A \sigma_B}. \tag{4.1}$$

These definitions hold true both in the classical and quantum-mechanical case (if A and B are observables), with averages taken over the ensemble.
Correlation functions are widely used in physics, since they represent an intuitive way of describing the dynamics of a system near equilibrium in the frame of linear response theory. On the other hand, neutron scattering offers - in the elegant formalization by van Hove [124] - an effective method to quantify several correlations functions that are of relevance to condensed-matter systems.
As to inelastic techniques, for example, direct access is given to either the dynamic structure factor $S(\mathbf{Q}, \omega)$ or the intermediate scattering function $F(\mathbf{Q}, t)$ (and, thus, to the van Hove function $G(\mathbf{r}, t)$), as well as to the velocity auto-correlation function, as described in details in paragraph 4.3 and in Appendices B and C.

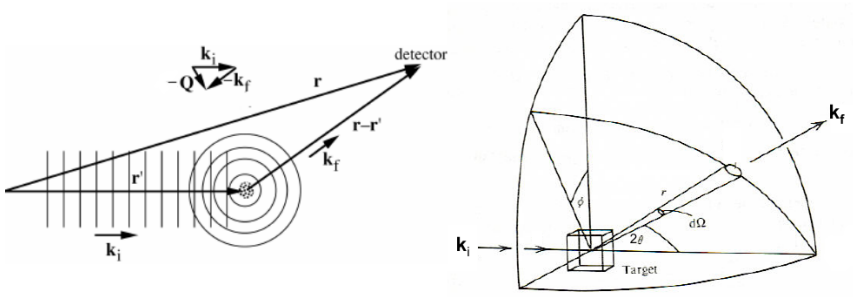

Figure 4.1: Wave- and position vectors in neutron scattering. Reproduced from [125] with modifications.

4.2 Nuts and bolts

One formal way to treat neutron scattering (Fig. 4.1) prescribes to start from Fermi's golden rule [31,125], that is, to evaluate, within first-order perturbation theory[1], the transition rate

$$W_{\mathbf{k_i}\sigma_i\tau_i\rightarrow\mathbf{k_f}\sigma_f\tau_f} = \frac{2\pi}{\hbar}| < \mathbf{k_f}\sigma_f\tau_f|V|\mathbf{k_i}\sigma_i\tau_i > |^2\rho_{\mathbf{k_f}\sigma_f}(E_f) \tag{4.2}$$

with final and initial states including coordinates for both neutron and scatterer, V the interaction potential, $\mathbf{k_{i,f}}$ scattering wavevectors, $\sigma_{i,f}$ neutron spin states, $\tau_{i,f}$ target states, and $\rho_{\mathbf{k_f}\sigma_f}(E_f)$ the density of final neutron scattering states per unit energy interval[2] .
If one: a) models wave functions as plane waves (reasonable when source, target and detector are far from one another); b) works with normalized states and quantities; c) takes into account energy conservation for both neutron and target; d) and, once calculated the double-differential cross-section, sums over all final target- and neutron-spin states, and performs an average over homologous initial states; then a very general expression is retrieved for $\left(\frac{d^2\sigma}{d\Omega dE}\right)_{\mathbf{k_i}\rightarrow\mathbf{k_f}}$

$$\left(\frac{d^2\sigma}{d\Omega dE}\right)_{\mathbf{k_i}\rightarrow\mathbf{k_f}} = \frac{1}{N}\frac{k_f}{k_i}\left(\frac{m_n V_0}{2\pi\hbar^2}\right)^2 \sum_{\tau_i\sigma_i} p_{\tau_i}p_{\sigma_i}\sum_{\tau_f\sigma_f}| < \mathbf{k_f}\sigma_f\tau_f|V|\mathbf{k_i}\sigma_i\tau_i > |^2\delta(E+E_{\tau_i}-E_{\tau_f}). \tag{4.3}$$

with V_0 the volume of the scattering system.
If now V is replaced by a sum of Fermi pseudopotentials ($4\pi\frac{\hbar^2}{2m_n}\sum_j b_j\delta(\mathbf{r}-\mathbf{R_j})$, with m_n the neutron mass, b_j the j^{th} scattering length, and $\mathbf{R_j}$ the j^{th} crystal vector) centered at any $\mathbf{R_j}$ (or, in general, at point nuclei in case of no periodicity), the master formula 4.3 reads

[1]First-order perturbation theory is a reliable approximation here, since neutron-nucleus interaction potential is short-range and energies are small enough to guarantee that only zero-orbital-angular momentum (s-wave) scattering applies (provided that we are far from resonances) [126].

[2]The condition $|\mathbf{k_i}| \neq |\mathbf{k_f}|$ ensures inelasticity of the scattering and consequent scatterer motion. We are conversely neglecting any excitation of the internal structure of the target.

$$\left(\frac{d^2\sigma}{d\Omega dE}\right)_{\mathbf{k_i}\to\mathbf{k_f}} = \frac{1}{N}\frac{k_f}{k_i}\sum_{\tau_i\sigma_i} p_{\tau_i} p_{\sigma_i} |\sum_{\tau_f\sigma_f}\sum_j b_j < \sigma_f\tau_f|e^{\mathbf{Q}\cdot\mathbf{R_j}}|\sigma_i\tau_i > |^2 \delta(E + E_{\tau_i} - E_{\tau_f}) \tag{4.4}$$

which, in the case of unpolarized neutrons (neutron-spin states equally probable for both incident and scattered waves), gets reduced to

$$\left(\frac{d^2\sigma}{d\Omega dE}\right)_{\mathbf{k_i}\to\mathbf{k_f}} = \frac{1}{N}\frac{k_f}{k_i}\sum_{\tau_i} p_{\tau_i} |\sum_{\tau_f}\sum_j b_j < \tau_f|e^{\mathbf{Q}\cdot\mathbf{R_j}}|\tau_i > |^2 \delta(E + E_{\tau_i} - E_{\tau_f}). \tag{4.5}$$

A useful info, when a computer simulation must be built up, is the time evolution of positions[3] $\mathbf{R_j}$.
If final target states form a complete set (that is, $\sum_{\tau_f}|\tau_f >< \tau_f| = 1$), initial target states are thermally averaged, and the delta function in Eq. 4.5 is replaced with its integral representation

$$\delta(E + E_{\tau_i} - E_{\tau_f}) = \frac{1}{2\pi\hbar}\int_{-\infty}^{+\infty} e^{-i\frac{t}{\hbar}(E+E_{\tau_i}-E_{\tau_f})} dt, \tag{4.6}$$

then one finally retrieves

$$\left(\frac{d^2\sigma}{d\Omega dE}\right)_{\mathbf{k_i}\to\mathbf{k_f}} = \frac{1}{N}\frac{k_f}{k_i}\frac{1}{2\pi\hbar}\int_{-\infty}^{+\infty}\sum_{jj'}\left\langle b_j^* b_{j'} e^{-i\mathbf{Q}\cdot\mathbf{R_j}(0)} e^{i\mathbf{Q}\cdot\mathbf{R_{j'}}(t)}\right\rangle e^{-\frac{iEt}{\hbar}} dt \tag{4.7}$$

which is sort of 'real-time representation' of the double-differential cross section as containing information on the spatial and temporal evolution of scatterer pairs, weighted by pair products of nuclear scattering lengths b.
In cases when the atomic state is independent of nuclear variables (i.e, nuclear spins and isotopes for a given element are randomly distributed[4]), Eq. 4.7 can be averaged over initial nuclear-spin and isotope distributions

$$\left(\frac{d^2\sigma}{d\Omega dE}\right)_{\mathbf{k_i}\to\mathbf{k_f}} = \frac{1}{N}\frac{k_f}{k_i}\frac{1}{2\pi\hbar}\int_{-\infty}^{+\infty}\sum_{ll'}\sum_{j\in l, j'\in l'}\overline{b_j^* b_{j'}}\left\langle e^{-i\mathbf{Q}\cdot\mathbf{R_j}(0)} e^{i\mathbf{Q}\cdot\mathbf{R_{j'}}(t)}\right\rangle e^{-\frac{iEt}{\hbar}} dt \tag{4.8}$$

with l and l' referring to different elements and the bar representing the above-mentioned average.

4.2.1 Individual vs. collective

If nuclear spins and isotopes are uncorrelated, then $\overline{b_j^* b_{j'}} = \overline{b_l^*}\,\overline{b_{l'}} + (\overline{|b_l^2|} - |\overline{b_l}|^2)\delta_{jj'}\delta_{ll'}$.
Once defined

$$S_{jj'}(\mathbf{Q}, E) = \int_{-\infty}^{+\infty}\left\langle e^{-i\mathbf{Q}\cdot\mathbf{R_j}(0)} e^{i\mathbf{Q}\cdot\mathbf{R_{j'}}(t)}\right\rangle e^{-\frac{iEt}{\hbar}} dt \tag{4.9}$$

[3] For example, when one is interested in the computation of neutron cross-sections.
[4] Significant exceptions are molecular hydrogen and $\frac{^3He}{^4He}$ mixtures.

Eq. 4.8 can be rewritten

$$\left(\frac{d^2\sigma}{d\Omega dE}\right)_{\mathbf{k_i}\to\mathbf{k_f}} = \frac{1}{N}\frac{k_f}{k_i}\left[\sum_{ll'}\overline{b_l^* b_{l'}}\sum_{j\in l, j'\in l'} S_{jj'}(\mathbf{Q},E) + \sum_l (|\overline{b_l^2}| - |\overline{b_l}|^2)\sum_{j\in l} S_{jj}(\mathbf{Q},E)\right] \tag{4.10}$$

with the first term containing interference contributions (coherent scattering) and the second representing a correlation between the position of any atom at $t = 0$ and the one of the same atom at time t (incoherent scattering).
Coherent scattering is sensitive to the relative arrangement of atom pairs in the target, incoherent scattering to one-particle spatial correlations[5].
Accordingly, coherent ($\sigma_{coh} = 4\pi|\overline{b_l}|^2$) and incoherent ($\sigma_{inc} = 4\pi(|\overline{b_l^2}| - |\overline{b_l}|^2)$) scattering cross sections can be identified.

4.3 Simply inelastic

Let's go back to Fig. 1.9.
The typical output of INS experiments is the so-called dynamic structure factor[6] $S(\mathbf{Q},\omega)$, which can be related to the double-differential cross-section by Eq. 4.10.
$S(\mathbf{Q})$ can be represented as the result of a double Fourier transformation (FT) performed on the van Hove correlation function $G(\mathbf{r},t)$ (see Appendix B), once towards the momentum- and once towards the frequency domain.
The former operation returns the so-called intermediate scattering function[7]

$$F(\mathbf{Q},t) = \int d\mathbf{r} G(\mathbf{r},t) e^{i\mathbf{Q}\cdot\mathbf{r}}. \tag{4.11}$$

$F(\mathbf{Q},t)$ is an interesting object, which gives info about correlations between density fluctuations of the wave vectors. Indeed, according to the definition of G given in Appendix B

$$F(\mathbf{Q},t) = \frac{1}{\rho}\int d(\mathbf{r}-\mathbf{r}') < \rho(\mathbf{r}',0)\rho(\mathbf{r},t) > e^{i\mathbf{Q}\cdot(\mathbf{r}-\mathbf{r}')} = \frac{1}{N} < \rho_{-\mathbf{Q}}(0)\rho_{\mathbf{Q}}(t) >, \tag{4.12}$$

that is, $F(\mathbf{Q},t)$ is the configurational FT of the density correlation function.
The latter transformation on G gives the final dynamic structure factor

$$S(\mathbf{Q},\omega) = \frac{1}{2\pi}\int_{-\infty}^{+\infty} F(\mathbf{Q},t) e^{-i\omega t} dt. \tag{4.13}$$

[5]Incoherent scattering arises from the random distribution of scattering lenghts around its mean value. Those species with only one scattering length for all possible nucler-spin states are, therefore, subject to coherent scattering alone. This is the case of all nuclides with zero nuclear spin (such as ^{12}C, ^{16}O, or ^{32}S).

[6]Frequency integration of $S(\mathbf{Q},\omega)$ at any fixed $\mathbf{Q}$ returns the static structure factor $S(\mathbf{Q})$, which is usually obtained by diffraction.

[7] From an experimental point of view, $F(\mathbf{Q},t)$ is usually obtained directly via spin-echo scattering.

which returns the frequency spectrum of correlations between density fluctuations of wave vector $\mathbf{Q}$

$$2\pi S(\mathbf{Q},\omega)\delta(\omega+\omega') =< \rho_{-\mathbf{Q}}(\omega')\rho_{\mathbf{Q}}(\omega) > \tag{4.14}$$

whose peaks are centered on the frequencies of intrinsic modes of the system.
As seen in the case of the van Hove correlation function, self and distinct contributions can be defined for both F and S.
However, it is worth noticing here that, while G_s gives life to the incoherent part of the scattering described in paragraph 4.2.1, it is the the entire G function to account for the coherent part [124]. This explains why experimentally telling coherent scattering apart from incoherent not rarely proves an arduous task.
Also notice how $S(\mathbf{Q},\omega)$, unlike $G(\mathbf{r},t)$, is a real function (i.e., an experimental observable) [31].
The dynamic structure factor obeys a list of sum rules that concern its frequency moments and can be very useful to the experimentalist as a way to normalize data. By a simple Taylor series expansion, one finds [127, 128]

$$\left[\frac{d^n}{dt^n}F(\mathbf{Q},t)\right]_{t=0} = (-i)^n\int_{-\infty}^{+\infty}\omega^n S(\mathbf{Q},\omega)d\omega \doteq (-i)^n < \omega^n > \tag{4.15}$$

from which

- 0^{th} moment: $< \omega^0 >_{coh} = S(\mathbf{Q})$ and $< \omega^0 >_{inc} = 1$
- 1^{nd} moment: $< \omega^1 >_{coh} =< \omega^1 >_{inc} = \frac{\hbar^2 Q^2}{2M}$ (i.e., zero for any theory with distinguishable particles and symmetric wavefunctions)
- 2^{th} moment: $< \omega^2 >_{coh} =< \omega^2 >_{inc} = \frac{k_B T Q^2}{M} + O(\hbar^2)$

with M the scatterer mass.
Spectral moments of order higher than one depend on the details of the microscopic interactions, and can be analytically derived for additive pairwise interatomic potentials [128, 129].

4.3.1 The VDoS within the harmonic approximation

One important piece of information one can retrieve by INS is the phonon (PDoS) or, more commonly, vibrational density of states (VDoS), which is that function $g(\omega)$ returning, when multiplied by $d\omega$, the fraction of normal modes of the system with frequencies in the range $(\omega, \omega+d\omega)$. This object is pretty important in chemical physics, since statistical kinetic theories of dynamic processes - for example, energy transfer or reactivity - depend on it in their formulation.
In order to link the VDoS to the double-differential cross-section, let's start, as costumary, from a high-symmetry crystal with only one atom per unit cell (Bravais lattice). Undoubtly, this traditional approach has many merits, but, considering that much of the current scientific interest is focused on disordered and amorphous systems, it's convenient to introduce a somewhat 'operational' definition of a general solid, that is, the idea of a system where - irrespective of any lack of long-range order

or periodicity - each atom has a well-defined and fixed equilibrium position $\mathbf{j}$ over the duration of a measurement [31].
Accordingly, the atom position $\mathbf{R_j}(t)$ around this site can be expressed in terms of the instantaneous displacement from equilibrium $\mathbf{u_j}(t)$, i.e., $\mathbf{R_j}(t) = \mathbf{j} + \mathbf{u_j}(t)$, $j = 1, ..., n$.
If the oscillations around the equilibrium position are small with respect to interatomic distances, then the system can be formalized as a set of coupled harmonic oscillators, and the displacement $\mathbf{u_j}$ becomes a superposition of $3N$ crystal's normal modes.
Introducing the harmonic approximation means assuming the potential energy surface to behave like a harmonic potential in the local neighborhood of a minimum, directly deriving vibrational frequencies from the second derivatives of this potential energy. Although this method works very well in many cases, it neglects anharmonicities, so that empirical scaling factors are often introduced to overcome this issue.
That said, the dynamic structure factor takes the form

$$S(\mathbf{Q},\omega) = \frac{1}{2\pi N\hbar}\sum_{jj'} e^{i\mathbf{Q}\cdot(\mathbf{R_j}-\mathbf{R_{j'}})}\int < e^{-i\mathbf{Q}\cdot(\mathbf{u_{j'}}(0)-\mathbf{u_j}(t))} > e^{-i\omega t}dt, \tag{4.16}$$

which can be rewritten

$$S(\mathbf{Q},\omega) = \frac{1}{2\pi\hbar}\sum_{j} e^{i\mathbf{Q}\cdot\mathbf{R_j}}\int < e^{U}e^{V} > e^{-i\omega t}dt \tag{4.17}$$

if $\mathbf{R_{j'}} = \mathbf{0}$ and $U = -i\mathbf{Q}\cdot\mathbf{u_0}(0)$, $V = -i\mathbf{Q}\cdot\mathbf{u_j}(t)$.
Making use of the Baker-Hausdorff formula[8] and assuming a Gaussian profile for $< e^{U+V} >$, at thermal equilibrium one gets

$$< e^{U}e^{V} >= e^{<U^2>}e^{<UV>} \tag{4.18}$$

where the former multiplicative term is the so-called Debye-Waller factor[9] and the exponent of the latter is the pair correlation function for the displacement from equilibrium position (phonon cross-section).
For small (harmonic) displacements, $e^{<UV>}$ undergoes a 'multi-phonon expansion'

$$e^{<UV>} = 1 + < UV > + \frac{1}{2} < UV >^2 + ... \tag{4.19}$$

where the zero-order term returns the elastic scattering (Bragg scattering), the 1^{st}-order term the 1-phonon contribution including all events that cause either the

[8]The Baker-(Campbell)-Hausdorff formula is a very useful tool to disentangle exponentials of operators. In the general case, this formula reads $e^A e^B = e^{A+B+[A,B]/2} + ...$ for non-commuting operators A and B. In the special case when $[A, B] = C$, with $[C, A] = 0$ and $[C, B] = 0$, the exact formula $e^A e^B = e^{A+B+[A,B]/2}$ holds true.

[9] The Debye-Waller factor $e^{<U^2>} = e^{-2W}$ is commonly used in condensed-matter theory to describe the attenuation of scattering intensity due to the thermal motion of scatterers. For isotropic systems (e.g., polycrystalline samples), it simplifies to $e^{-2W} = e^{-\frac{1}{3}Q^2<u^2>}$, where $< u^2 >$ is the mean square displacement [31].

creation or the annihilation of one phonon, the 2^{nd}-order term the 2-phonon contribution (at different $\mathbf{Q}$ and frequency) and so on.
As seen earlier, the incoherent cross-section is proportional to the space-time FT of the self-component of $G(\mathbf{r},t)$. In particular, truncating the multiphonon expansion after the first order one is able to recover the one-phonon incoherent cross-section, which amounts to

$$\left(\frac{d^2\sigma}{d\Omega dE'}\right)_i^{\pm 1} = \frac{\sigma_i}{4\pi}\frac{k_f}{k_i}\frac{1}{2M}e^{-2W}\sum_j \frac{|\boldsymbol{Q}\cdot\boldsymbol{\epsilon}_j|}{\omega_j}[< n_j+1 > \delta(\omega-\omega_j)+ < n_j > \delta(\omega+\omega_j)], \tag{4.20}$$

where $< n_j >$ is the Bose occupation number for the j^{th} phonon mode and $\epsilon_{\mathbf{j}}$ the associated polarization vector.
That means, when replacing the j-sum with an integral (continuous ensemble of final momenta) and making an average over all orientations,

$$\left(\frac{d^2\sigma}{d\Omega dE'}\right)_i^{\pm 1} = \frac{\sigma_i}{4\pi}\frac{k_f}{k_i}\frac{3N}{2M}e^{-2W} < |\boldsymbol{Q}\cdot\boldsymbol{\varepsilon}|^2 > \int_0^{\omega_{max}} d\omega' \frac{g(\omega)}{\omega'}[< n+1 > \delta(\omega-\omega')+$$

$$+ < n > \delta(\omega+\omega')] \tag{4.21}$$

with $g(\omega)$ the above-mentioned VDoS.
Of course, when there is more than one atom per unit cell, there will be more than one solution of the dynamic equation for the system, that is, more than one phonon mode. In this case, different phonon branches (acoustic and optical) appear in the spectrum and they can be treated independently, with the final expression for the density of states written as the sum over all of the mentioned modes.
In principle, Eq. 4.21, suitably simplified according to the symmetry properties of the system under study[10], offers a direct tool to retrieve the VDoS from $S(\mathbf{Q},\omega)$ in the $\mathbf{Q}\to\mathbf{0}$ limit[11]. Yet, from a practical point of view, working out the VDoS from the measured double differential cross section may prove a non-trivial task.
Indeed, only when the system can be reasonably represented as an incoherent scatterer the incoherent 1-phonon approximation can be safely used to get the VDoS in the limit where the multiphonon contributions are negligible or correctly accounted for and subtracted. That's why selecting the lowest $\mathbf{Q}$-values available is always a recommendable practice in the extrapolation of the VDoS, since at high $\mathbf{Q}$s' the relevant 1-phonon features are often masked and swamped by multiphonon contributions. In any case, the experimental neutron spectra recorded at higher $\mathbf{Q}$-values (backscattering) may be utilized, at a later time, to perform an independent check of the VDoS-extraction procedure [130].

[10] For example, in the case of a cubic Bravais lattice ($< |\boldsymbol{Q}\cdot\boldsymbol{\epsilon}|^2 >= \frac{1}{3}Q^2$), Eq. 4.21 is reduced to

$$\left(\frac{d^2\sigma}{d\Omega dE'}\right)_i^{\pm 1} = \frac{\sigma_i}{4\pi}\frac{k_f}{k_i}\frac{N}{4M}e^{-2W}Q^2\frac{g(\omega)}{\omega}(coth(\frac{\hbar\omega}{2k_BT})\pm 1), \tag{4.22}$$

being $< n+\frac{1}{2}\pm\frac{1}{2} >= \frac{1}{2}(coth(\frac{\hbar\omega}{2k_BT})\pm 1)$.
[11] In the case of water, 'tradition' suggests that the $\mathbf{Q}\to\mathbf{0}$ limit is satisfied when $Q < 10\ nm^{-1}$.

If the one-phonon approximation holds, in the framework of decoupled molecular translations, rotations and vibrations [131], one can write the total incoherent cross-section as proportional to the product of a Debye-Waller term (usually exactly recoverable from a comparison of the Q-dependence of the INS elastic line to diffraction data, provided that the harmonic assumption can be applied) times the incoherent dynamic structure factor, from which the VDoS is usually retrieved by means of self-consistent iterative routines [132].
From this point of view, INS is suitable for the study of hydrogen-atom dynamics in water. In fact, the scattering cross-section for (bound) ^1H is > 80 barn (much larger than the one of oxygen and typical metals used for the sample holder) and essentially incoherent. Thus, the INS spectrum basically mirrors the self-dynamics of hydrogens in the sample.
Notice how, as long as the harmonic approximation applies, the multiphonon expansion doesn't lose its validity, which means that that Eq. 4.21 is of general use even in case of no long-range order (as in an amorph), even though all the inelastic scattering becomes diffuse.

4.4 Deep inelastic

Inelastic neutron scattering at high energy ($\geq$ 1 eV) and momentum ($\geq$ 25 Å^{-1}) transfers - known as the DINS or Neutron Compton Scattering (NCS) regime - represents an *unicum* in the spectroscopy scene, since it's the only technique now available to measure the zero-point mean kinetic energy $< E_k >$ and the one-particle momentum distribution $n(\mathbf{p})$ of the scattering nuclei in condensed matter[12] in the absence of specific approximations[13] other than the impulse approximation (IA) [133]. This kind of experimental information proves pretty relevant, since the behavior of light nuclei in condensed phases is significantly affected by quantum effects even at room temperature [37, 134, 135].
When DINS conditions are met, scattering is well described within the framework of the IA, which assumes that the scatterers recoil freely from the collision, with inter-particle interaction in the final state being negligible (i.e., the wave function of the particle in its final state is a plane wave). The IA can be regarded as a special case of the incoherent approximation, where, in the case of high energy collisions, a short-time expansion ($t \to 0$) of the atomic position operator, $\mathbf{R}(t)$, is applied to the position operator of any scatterer of mass M and momentum $\mathbf{p}$, i.e., $\mathbf{R}(t) = \mathbf{R}(0) + \frac{t}{M}\mathbf{p}$ [134]. In other words, one is assuming that, after collision, the scatterer travels freely over short enough times, over which its interaction with other particles can be neglected.
Under the IA, if one applies momentum- and energy-conservation laws, the energy distribution of the scattered neutrons gets directly related to the distribution of particle momenta parallel to the wave vector transfer, since

[12] This experimental method is analogous to the measurement of the electronic momentum distribution through Compton scattering of high-energy photons from electrons, or the nucleon momentum distribution via quasi-elastic electron scattering from nuclei.

[13] In optical scattering and INS, for example, both harmonicity and decoupling between the degrees of freedom of translation, rotation and vibration are of common use.

$$\hbar\omega = \frac{(\mathbf{p_n} - \mathbf{p_{n'}})^2}{2M} + \frac{(\mathbf{p_n} - \mathbf{p_{n'}})\cdot\mathbf{p}}{M} = \frac{(\hbar\mathbf{Q})^2}{2M} + \frac{\hbar\mathbf{Q}\cdot\mathbf{p}}{M} \tag{4.23}$$

with M and $\mathbf{p}$ mass and momentum, respectively, of the scatterer, whereas $\mathbf{p_n}$ and $\mathbf{p_{n'}}$ represent the momenta of the incident and scattered neutron, respectively.
In this case, if one applies the short-time expansion of $\mathbf{R}(t)$ to the self-component $F_i(Q,t) =< e^{-i\mathbf{Q}\cdot\mathbf{R}(0)}e^{-i\mathbf{Q}\cdot\mathbf{R}(t)} >$ of the intermediate function, the resulting (incoherent) dynamic structure factor takes the form

$$S_{IA}(\mathbf{Q},\omega) = \hbar \int n(\mathbf{p})\delta\left(\hbar\omega - \hbar\omega_r - \frac{\hbar\mathbf{Q}\cdot\mathbf{p}}{M}\right) d\mathbf{p} \tag{4.24}$$

with first moment given by the recoil energy $\hbar\omega_r = \frac{\hbar^2Q^2}{2M}$.
Notice how the position of the recoil energy depends on M, which means that different elements (and isotopes!) in the sample can be easily told apart from each other by direct inspection of the spectrum.
Further, the two dynamic variables ω and $\mathbf{Q}$ can be coupled into the West-scaling parameter[14] $y = \frac{1}{\hbar}\mathbf{p}\cdot\hat{\mathbf{Q}} = \frac{M}{\hbar^2Q}(\hbar\omega - \hbar\omega_r)$ [136], so that Eq. 4.24 can be re-written as

$$S_{IA} = \frac{M}{\hbar q} J_{IA}(y, \hat{\mathbf{Q}}), \tag{4.25}$$

$J_{IA} = \hbar \int n(\mathbf{p}')\delta\left(\hbar y - \hat{\mathbf{Q}}\cdot\mathbf{p}'\right) d\mathbf{p}'$ just being the projection of the momentum distribution $n(\mathbf{p})$ onto the y-space - or neutron Compton profile (NCP) - which represents the probability for a scatterer to have a momentum parallel to $\hat{\mathbf{Q}}$ and of magnitude between $\hbar y$ and $\hbar(y + dy)$.
What's remarkable in J_{IA} is this function no longer depending on $\mathbf{Q}$ and ω, but on y alone. Another notable property is the scaling $J(y) = \hbar J(\hbar y)$, which can be smartly utilized in calculations.
In the isotropic case, if one introduces polar coordinates for the component of $\mathbf{p}$ that is perpendicular to the $\mathbf{Q}$-direction, J_{IA} simplifies to $2\pi\hbar \int_{|\hbar y|}^{\infty} pn(p)dp$, from which

$$n(p) = -\frac{1}{2\pi\hbar^3 y}\left[\frac{dJ_{IA}(y)}{dy}\right]_{\hbar y = p}. \tag{4.26}$$

An important information retrievable from $J_{IA}(y)$ is the one-particle mean kinetic energy $< E_k >$, which is proportional to its second moment

$$< E_k >= \frac{3\hbar^2}{2M}\int_{-\infty}^{+\infty} dy\, y^2 J_{IA}(y). \tag{4.27}$$

The IA is exact in the limit of infinite momentum transfer only. At finite values of $\mathbf{Q}$ deviations occur, which are caused by the localization of the scatterer in its final state due to surrounding atoms, and termed final state effects (FSEs). This causes a broadening of J_{IA} that resembles an instrumental-resolution effect.

[14] Notice how $\hbar y$ corresponds to the momentum of the scatterer along the $\mathbf{Q}$-direction before the scattering event. The variable y vanishes for either the target nucleus being stationary or moving perpendicularly to $\mathbf{Q}$.

In the presence of FSEs, the J function gets dependent on the momentum transfer again, and can be described, in the isotropic case, via a $\frac{1}{Q}$ power series developed by Sears [137]

$$J(y,Q) = J(y) - \frac{A_3}{Q}\frac{d^3J(y)}{dy^3} + \frac{A^4}{Q^2}\frac{d^4J(y)}{dy^4} + ... \tag{4.28}$$

with coefficients A_n linked to the interatomic potential[15].
Also the NCP obeys a group of sum rules, which descend from the general sum rules valid for S_i. According to them, the J-function is a probability density distribution (longitudinal momentum distribution), with unitary 0^{th} moment, zero first moment, and second moment equal to $\frac{2M<E_k>}{3\hbar^2}$. On the other hand, the FSE corrections must have 0^{th}, first, and second moments equal to zero [134].

4.4.1 The point

The NCP from a harmonically bound atom in an isotropic system is Gaussian, and, as seen above, a measurement of its width yields an assessment of its mean kinetic energy. Essentially the same information obtainable, for example, via vibrational spectroscopy. So what's the point here?
Indeed, where the NCS technique for bound scatterers comes into its own is in its potential to directly monitor the *anharmonicity* of the binding potential, at least in cases where it is legitimate to treat the struck atom in terms of single-particle motion in an effective potential [138]. In fact, that's the only technique that is able to measure the Born–Oppenheimer potentials directly, being the extraction of the potential from the momentum distribution simply a matter of inverting the Schroedinger equation of the system[16].

[15]For example, the coefficient of the leading term after the zero-order is given by $A_3 = \frac{M<\nabla^2 V>}{36\hbar^2 Q}$, where the average is statistical. In case of a harmonic potential, $< \nabla^2 V >= \frac{12\hbar^2\overline{\sigma}^4}{M}$, where $\hbar\overline{\sigma} = \frac{2\hbar^2\overline{\sigma}^4}{M}$ represents the mean curvature of the potential, intended as the average of directional curvatures $\hbar\sigma_\alpha = \frac{2\hbar^2\sigma_\alpha^4}{M}$ characterizing a multivariate momentum distribution.

[16]Remember that $\psi(\mathbf{r})$ and $\psi(\mathbf{p})$ are Fourier transforms of each other, and the latter is obtained from $n(\mathbf{p}) = |\psi(\mathbf{p})|^2$. The phase ambiguity in extracting the momentum-space wave function from $n(\mathbf{p})$ does not constitutes a trouble, since $\psi(\mathbf{p})$ can always be chosen as real.

5

Tech paraphernalia - A look at neutron spectrometers

Isis, oh Isis, you mystical child

Bob Dylan

5.1 Fission vs. spallation

In the context of neutron production for scientific purposes, fission- and spallation reactors are the most common sites available today [139].
As to the former process, let's take into account a typical ^{235}U reactor.
When thermal neutrons collide with ^{235}U, this isotope of uranium undergoes fission producing on average 2.5 fast neutrons (apart from the two fission fragments) and about 180 MeV of energy per event.
In a critical system the reaction becomes self-sustained: precisely, out of the 2.5 above-mentioned neutrons, one triggers another fission, 0.5 is absorbed in other materials, and one escapes the core surface and is available for other scopes.
Fig. 5.1 reports the energy spectrum for our ^{235}U reactor. Three fundamental regions can be spotted. The fast region is the one where neutrons are produced, and is described via a Lamb distribution

$$\Phi(E)dE = \Phi_f e^{-Esinh(2E)}dE, \;\; E > 0.5\, MeV \tag{5.1}$$

with its peak falling between 1 and 2 MeV of energy.
The intermediate epithermal region is formalized by the distribution

$$\Phi(E)dE = \frac{\Phi_{epi}}{E}dE, \;\; 200\, meV < E < 0.5\, MeV \tag{5.2}$$

and describes the process of neutron moderation.
Finally, in the thermal region, the spectrum goes towards thermodynamic equilibrium with the moderator via collisions. The resulting distribution is a typical Maxwell-Boltzmann

$$\Phi(E)dE = \Phi_{th}\frac{E}{K_B T_n}e^{-\frac{E}{K_B T_n}}dE, \;\; E < 200\, meV \tag{5.3}$$

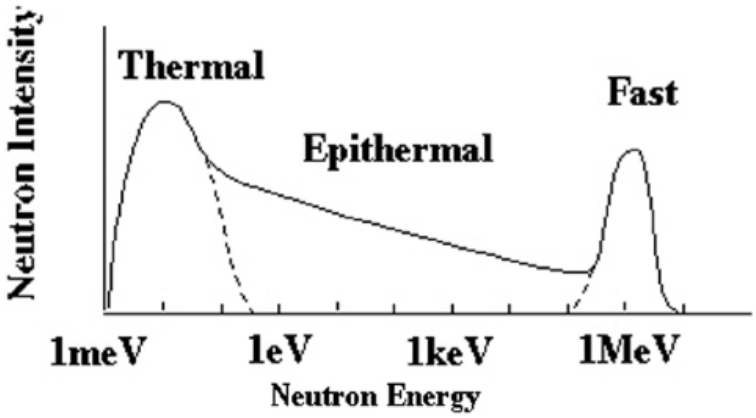

Figure 5.1: Energy spectrum for a ^{235}U reactor. Not to scale as to intensities. Reproduced from [139].

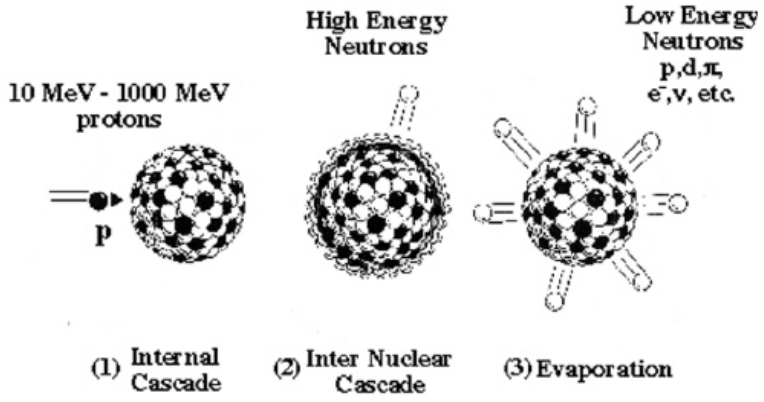

Figure 5.2: A schematic spallation reaction. Reproduced from [139].

characterized by an effective temperature[1] $T_n \sim 300$ K and a peak around 25 meV for room-T moderators.
Spallation is an intrisically different process, which is triggered by very energetic particles - exclusively beyond an energy threshold of 5-15 MeV - bombing heavy nuclei (Fig. 5.2).
This sequential reaction includes the incorporation of the incident particle into the target, then an internal nuclear cascade characterized by the ejection of highly ergetic neutrons, and, finally, sort of 'evaporation' phenomenon during which the heavy nucleus leaves its excited state while emitting many low-energy neutrons, other nucleons, photons and neutrinos. Incident particles are usually highly energetic ($\sim$ 1 GeV) protons produced by linear or circular accelerators at pulsed sources (Fig. 5.3).
In a spallation reaction $20 - 30$ neutrons per incident particle are produced, with

[1] T_n is always a bit higher than the moderator temperature, since full equilibrium is never reachable in a moderator of finite size.

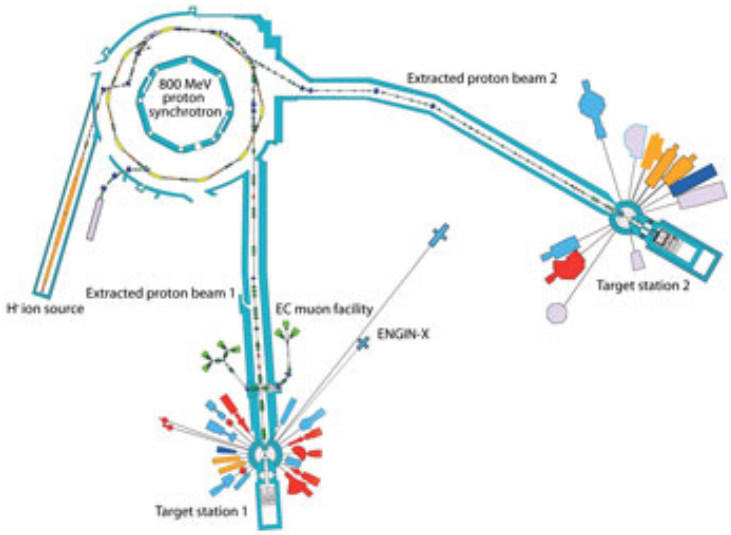

Figure 5.3: Layout of the ISIS spallation source (RAL, UK) with the corresponding beamline arrangement at Target Station 1 and 2. Reproduced from the IRC website.

Table 5.1: Major differences between spallation- and fission reactors. Reproduced with modifications from [139].

Spallation	Fission
More high-E neutrons	More low-E neutrons
Pulsed operations	Continuous operations
Sharp pulses $\rightarrow$ high resolution	Resolution adaptable to the problem
Asymmetric resolution function	Gaussian resolution function
Must use ToF techniques	Complete flexibility
Environmentally friendly	Environmentally unfriendly
Still to explore and improve	Basically tested and not improvable

low released energy per neutron (about 55 MeV).

Fig. 5.4 shows the emission spectrum for an 800 MeV spallation reactor whose target is partly Pb (no fission) and partly ^{238}U (fast fission). Cascade reactions are responsible for a mere 3% of source neutrons, but this minor percentage is produced at as large energies as those of incident neutrons, so that such processes become dominant as to shielding issues.

A comparison of spallation- to fission reactors in terms of assets and disadvantages is available in Table 5.1.

At pulsed sources, spectrometers must rely on Time-of-Flight (ToF) techniques, which measure the change in interacting-neutron velocity via retrieval of the time interval spent by a neutron to arrive to a detector and be revealed.

ToF spectrometers encompass two major families: direct- and inverted-geometry spectrometers.

Direct-geometry machines fix the initial neutron energy by chopper or monochromator, whereas the final energies are measured via time of flight. Inverted-geometry machines, which are radiated by a wide-energy-band neutron beam (white beam)

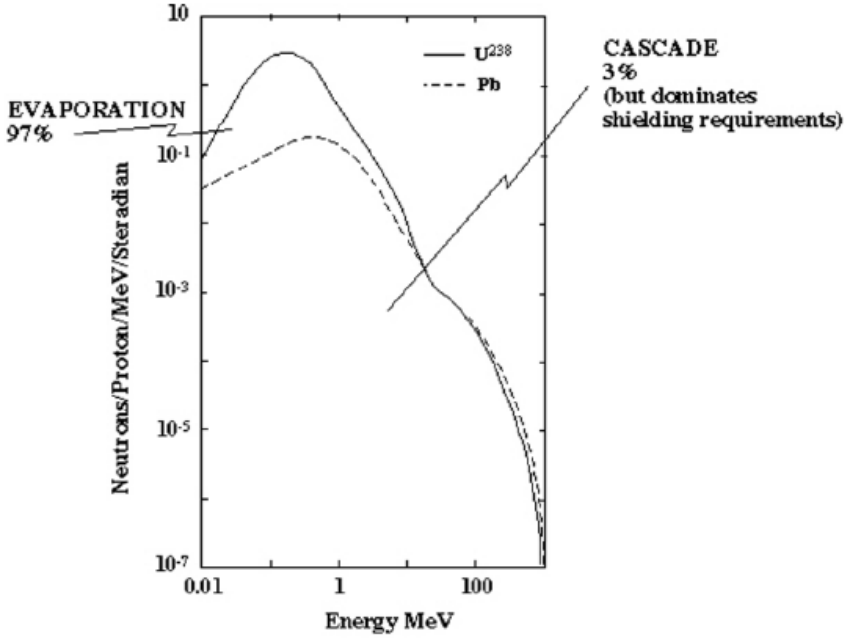

Figure 5.4: Emission spectrum of an 800 MeV spallation reactor with Pb+^{238}U target. Reproduced from [139].

and fix final energy via analyzer, make use of a reversed arrangement (Figs. 5.5 and 5.6) that guarantees high intensity with a relaxed Q-resolution, but at the expense of high background caused by neutrons scattered by structures behind the analyzers [31].
The accessible region of $(\mathbf{Q}, \omega)$-space (obtained from the momentum- and energy conservation conditions) is clearly different for the two configurations (Fig. 5.7). In particular, the inverted-geometry allows for the access to much higher energy transfers[2], which is usually associated to very good resolution at the elastic peak.
A ubiquitous feature of direct-geometry spectrometers is the presence of a chopper at the entrance of the beam.
If the source is non-pulsed (fission), the chopper only has to transform the incident beam into a pulsed one, while the energy selection is obtained via crystal-monochromator (for ex., IN5 at ILL) or chopper array (for ex., IN6 at ILL). Conversely, when the source is pulsed (spallation), the beam can be monochromated via Fermi chopper[3] (for ex., MARI at ISIS) [139].
Conversely, on inverse-geometry instruments operating in the range of epithermal energies the neutron energy-selection of common use consists of a foil analyzer, made

[2] The limitations in the kinematical space accessed are the main reason for the scarce use of direct-geometry instruments for scattering in the multi-eV range (DINS regime). At present the resolution on inverse-geometry resonance spectrometers is narrower by a factor between 15 and 60 with respect to direct-geometry choppers [140].

[3] Fermi choppers are shutters able to both pulse and monochromate the incident beam. They consist of sort of a collimator that rotates around an axis perpendicular to the beam direction, and possesses curved blades suitable to generate a straight collimation in the reference system of the beam neutrons.

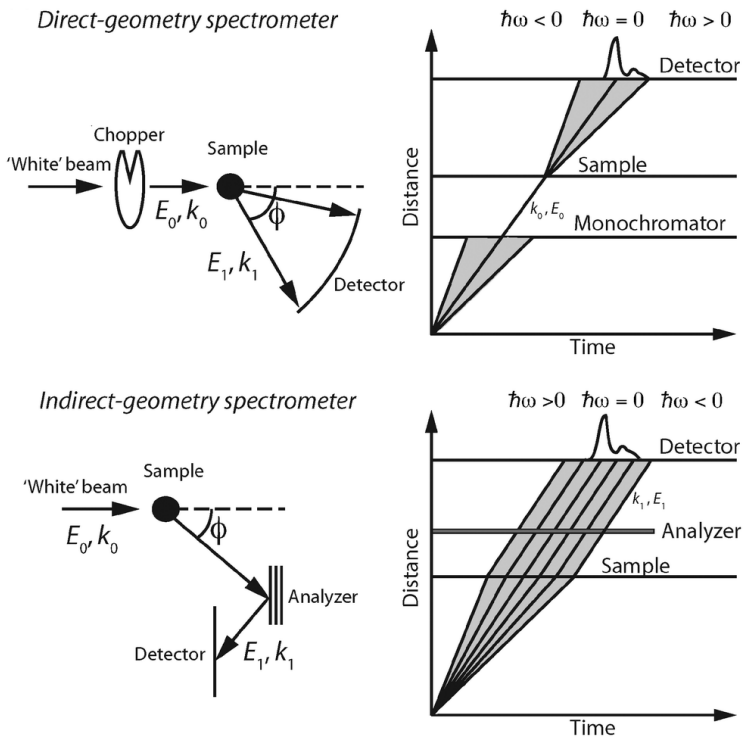

Figure 5.5: Left: Schematic representation of a direct- and inverse-geometry ToF spectrometer. Right: Distance-time plot for a direct- and inverse-geometry ToF spectrometer. Reproduced from [141].

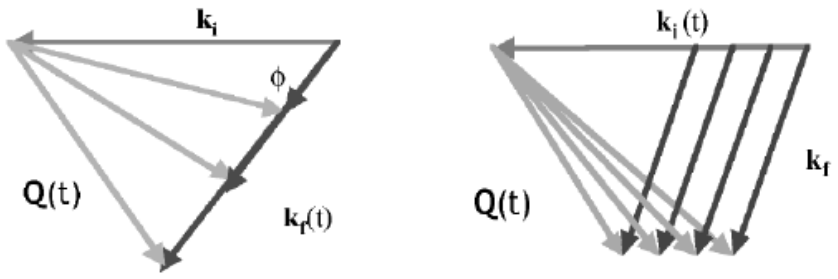

Figure 5.6: Scattering triangles for a direct- (left) and an inverted-geometry (right) ToF spectrometer. Reproduced from [139].

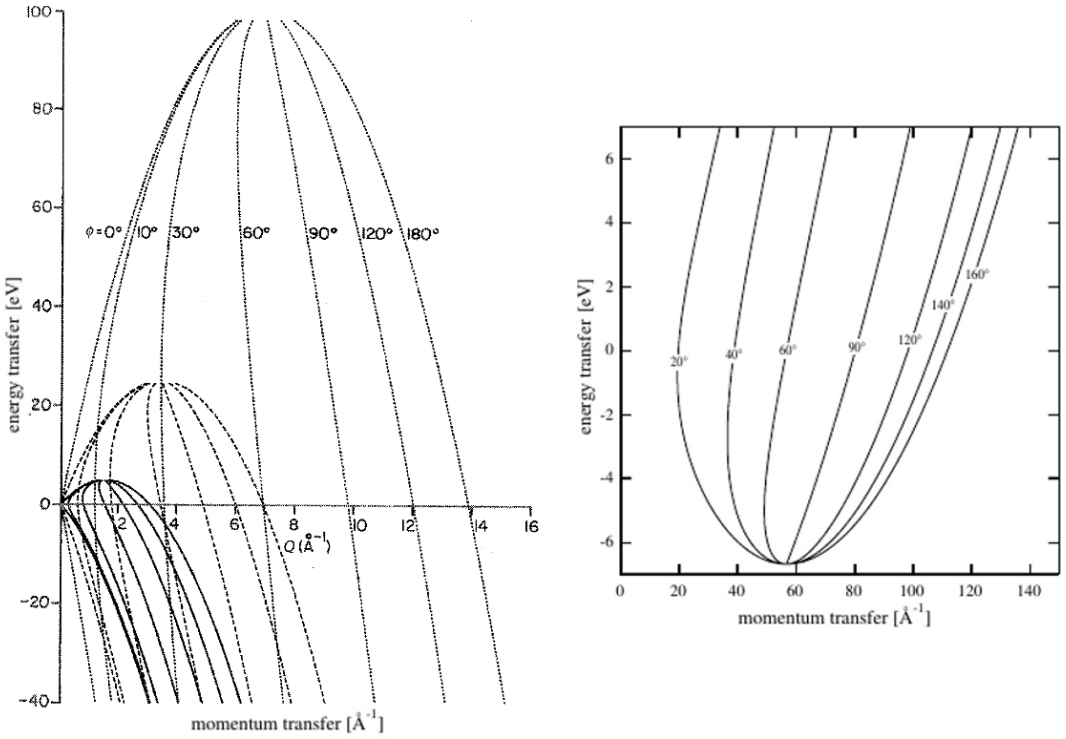

Figure 5.7: Accessible region of $(\mathbf{Q}, \omega)$-space in direct- (left) and inverted (right) configurations. Each radial line is the locus for a detector at a certain angle. Reproduced with modifications from [31] and [140].

of a material with narrow neutron resonance absorption peaks, that is placed in the scattered beam and acts as a filter, since better resolution and count rates can be obtained this way [140].

5.2 Chopper instruments: the case of MARI

The Multi-Angle Rotor Instrument (MARI), whose operations were established at the ISIS spallation neutron source of the Rutherford Appleton Lab (RAL), UK, in the 90s', is a highly versatile Fermi-chopper device (Fig. 5.8) characterized by a large neutron incident-energy range ($7 - 1000$ meV) and a modulable energy resolution ($(1.5 - 8)\%$), which makes it the ideal tool to investigate VDoSs in crystalline and disordered systems, as well as collective excitations in magnetic materials.

A detailed technical sheet of the instrument is available in Fig. 5.9.

In spite of its relatively low incident neutron flux ($10^4 \frac{n}{cm^2 s}$), this machine boasts the lowest instrumental background of the ISIS suite of chopper spectrometers, which makes the instrument highly sensitive all the same.

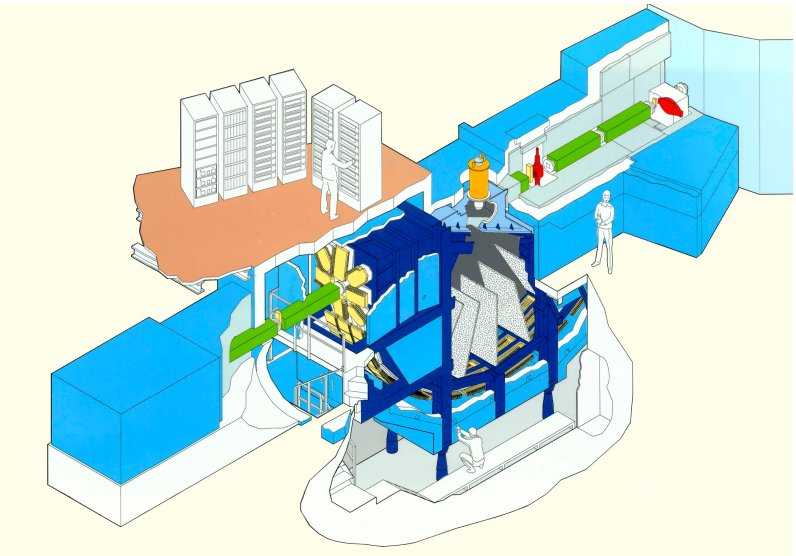

Figure 5.8: Schematic layout of MARI. Reproduced from the ISIS website.

5.3 Inverted-geometry instruments: the case of VESUVIO

Designed to exploit the DINS technique at energy- and momentum transfers in excess of 1 eV and 25 Å^{-1}, respectively, the inverted-geometry electron volt spectrometer (eVS) started its operations in mid 80s' at the ISIS spallation neutron source of the RAL, UK. The VESUVIO spectrometer has been upgrading the eVS instrument since 2002 (Fig. 5.10), definitely expanding the instrument capability[4], since the techniques set up in the last decade have allowed more than a 2-fold improvement in the instrumental resolution, and a factor-of-ten improvement in signal-to-background ratio [133, 140].

On average VESUVIO operates in a typical range $30 - 200$ Å^{-1} in terms of momentum transfer and $2.5 - 65$ eV in terms of recoil energy [133, 143], that is, at incident neutron wavelengths much smaller than the interatomic spacing (incoherent scattering ensured) and energy transfers that largely exceed binding molecular energies, respectively.

Raw data are recorded in the form of neutron countrates as a function of their ToFs from the source to the detectors, and the reconstruction of the scattering kinematics is performed by

$$t = t_0 + \frac{L_0}{v_0} + \frac{L_1}{v_1} \tag{5.4}$$

where t_0 is an offset due to delays in the electronic counting chain (-0.40(2) μs), L_0 is the path length from the source to the sample (11.005(1) m), L_1 the one from

[4] At present the incident neutron flux at the sample position, in the energy range 0.4 eV $\leq E_0 \leq$ 100 keV, is about $6.5 \cdot 10^6$ $\frac{n}{cm^2 s}$. This represents an incident flux comparable with the one in the thermal region available for INS spectrometers at both continuous and pulsed sources [140].

Moderator	liquid-methane (CH_4) at 105K (poisoned with Gd at 2.5 cm)				
Incident energy	7 - 1000 meV				
Energy resolution	Depends on the choice of Fermi chopper, incident energy and energy transfer D hw /E_i = 1.5-8 %				
Primary flight path	11.739 m				
Secondary flight path	4.020 m				
Fermi Chopper	10.050 m 50-600 Hz phased to ISIS pulse ± 0.1 µs 4 chopper packages are commonly used on MARI optimised for different incident energy and resolution requirements • **G-Chopper** - Gd slits, 7-200 meV, $\Delta E/E_i$ 2-5% • **S-Chopper** - "Sloppy", 7-1000 meV, $\Delta E/E_i$ 3-8% • **A-Chopper** - "High res", 100-1000 meV, $\Delta E/E_i$ 1.5-3% • **R-Chopper** - "Relaxed", 200-1000 meV, $\Delta E/E_i$ 2-7%				
Detectors	**Low Angle Bank** 4.020 m from sample 256 10 atm ^{3}He tubes in 8 fold array covering 3 - 13° scattering angle				
	High Angle Bank 4.020 m from sample 10 atm ^{3}He tubes covering 12° - 135° scattering angle				
Monitors	Monitor 1: 07.000 m from moderator Monitor 2: 10.297 m from moderator Monitor 3: 17.559 m from moderator				
Flux at Sample	[× 10^4 n cm^{-2} s^{-1}]				
		7 meV	**25 meV**	**100 meV**	**500 meV**
	G-Chopper 4% ΔE/E	0.5	1.4	0.9	n/a
	S-Chopper 5% ΔE/E	0.5	1.5	0.9	1.3
	A-Chopper 2.5% ΔE/E	n/a	n/a	0.3	0.4
	R-Chopper 4% ΔE/E	n/a	0.8	0.5	0.7

Figure 5.9: Technical sheet of MARI spectrometer. Reproduced from the ISIS website.

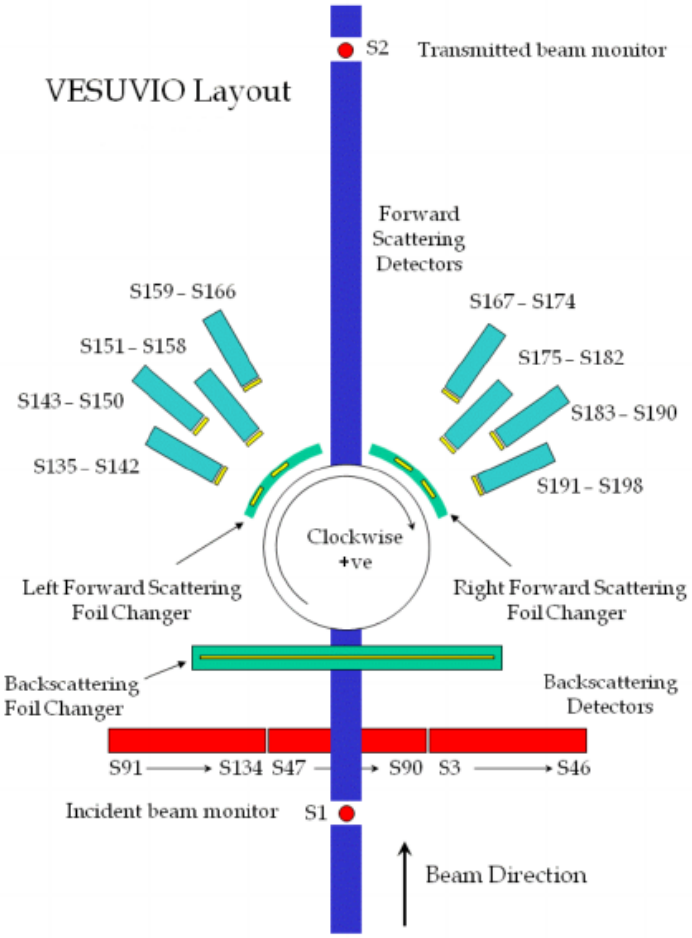

Figure 5.10: Schematic layout of VESUVIO. The spectrometer comprises 196 detectors, plus an incident (S1) and transmitted (S2) beam monitor. Forward-scattering YAP detectors ($S135 - S198$) have a vertical alignment and cover an angular range of 32.75° to 72.50°. Backscattering ^{6}Li-doped detectors ($S3 - S134$) are arranged into 3 horizontal banks perpendicular to the beam direction, and work in the angular range $(130 - 163)°$. Incoming neutrons are moderated by a water bath at $T = 295$ K. Reproduced from [142] with modifications.

the sample to any detector, v_0 is the velocity of the incident neutron, and v_1 the velocity of the scattered one [144].

Neutron velocities can be related to associated energies; as such, and through the knowledge of t, t_0, L_0, L_1 and v_0, both energy- and momentum transfers can be determined.

At each scattering angle the energy of the scattered neutrons is selected by Au analyzers (outcoming neutrons' energy upon calibration: 4897 meV) with the aid of resonance detection (RD) and foil cycling (FC) techniques [140] providing for notable resolution improvements, as to both energy resolution (32% narrowing of FWHM) and counting statistics (1% error at the center of the overall NCP and 15% at $\frac{1}{15}$ of the peak height, respectively), as well as to separation between proton and heavy-atom peaks in the sample and container, which prevents spectra from including distortions due to an inaccurate subtraction of non-^{1}H contributions. This way the uncertainty in the retrieved mean kinetic energies is reduced down to about 2% [145].

In backscattering, with detector banks equipped with ^{6}Li-doped glass scintillators only sensitive to neutrons, each ToF spectrum (at fixed angle) is retrieved by a set of three measurements: one with no filter, one with a filter of thickness d_1 and absorption $A_1(E_1)$, and one with a filter of the same material, but thickness d_2 and absorption $A_2(E_1)$ (being E_1 the final neutron energy).

This double-difference (DD) technique is intended to the improvement of energy resolution. Indeed, when the neutron-absorption cross-section σ_A is negligibly small (as in the tail regions of the foil resonance), $A_{1,2}(E_1) = 1 - e^{-Nd_{1,2}\sigma_A(E_1)}$ can be approximated with $Nd_{1,2}\sigma_A(E_1)$ (with basic suppression of the long exponential tails) and the resulting DD signal $A_1(E_1) - \frac{d_1}{d_2}A_2(E_1)$ goes null at large offsets from the resonance maximum [146].

The detector banks at forward scattering were upgraded in 2008 (Fig. 5.11), now consisting of γ-ray detecting cerium-doped Yttrium Aluminium Perovskite (YAP) scintillators. E_1 is still determined by the primary gold resonance at 4897 meV, but they are the ejected γ-rays that are detected in this case. The energy resolution here is increased by FC technique, with a primary gold foil fixed on the surface of any YAP detector, and a movable secondary gold foil of identical thickness placed close to the sample. The secondary foils get 'cycled', that is, moved many times between the two positions within a data collection period. This cycling removes drifts in detector efficiency with time (due, for example, to temperature changes), and returns a $\frac{1}{\sqrt{2}}$-shrinking of the resolution FWHM, with a loss in statistics of only about 10% [147] (Fig. 5.12).

Yet, the cycling of the secondary foils produces a sample-dependent γ-background of $\sim 5\%$. This unwanted contribution to the signal must be subtracted from spectra as part of the data analysis process [142].

At present VESUVIO spectrometer remains the only instrument providing a user programme for DINS research. Its most important limitation does not concern design, but rather flux. If an upgrade to the ISIS target and moderators were undertaken, that would result in a higher incident flux (and thus countrate), with experimental durations scaling down from the current average 18 hours for routine

Figure 5.11: A photograph of forward-scattering YAP-detector banks at VESUVIO spectrometer. Reproduced from [143].

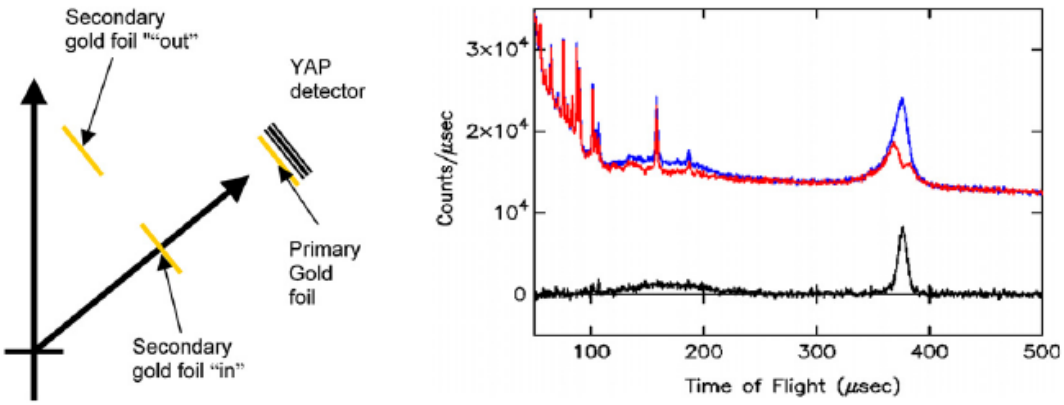

Figure 5.12: Left: A scheme of the FC method currently used on VESUVIO. Right: An example of FC-technique applied to a CH_2 sample at an angle of 67°: foil-out data are in blue, foil-in data in red, and the resulting difference is shown as the black line. Reproduced from [147] with modifications.

measurements to those of inelastic or quasi-elastic neutron scattering[5].
Still, the extension of the angular coverage at higher forward-scattering and lower backscattering regions would extend DINS to a range of partially-deuterated samples that are currently difficult to measure on VESUVIO, but potentially important for the isolation and examination of nuclear quantum effects involved in H/D substitutions.
Finally, the redesign of vertical detector-geometry in forward scattering, in the sense of moving to a conical array relative to the transmitted-beam axis, not only would improve angular resolution by a factor of ∼2, but even make the γ-background from the secondary analyser foils be averaged to zero [142].

5.3.1 Tips on reduction and analysis of VESUVIO raw data

In the only case of forward scattering, VESUVIO raw data must be, first of all, corrected for sample-dependent γ-background affecting YAP-detector countrates. This is usually done by a routine available on the instrument [148].
Next, sample- and container-dependent multiple-scattering (MS) contribution is usually accounted for and corrected by

- the simulation of single and multiple scattering up to the 4^{th} order [145];
- the subsequent normalization of the simulated spectra to the area of the corresponding experimental ToF data, and the multiplication of the simulated spectra by the recovered normalization constant;
- the final subtraction of simulated data from the experimental countrates.

Once γ- and MS-corrections are performed, every contribution other than the investigated nucleus is subtracted from each spectrum. This is not done directly, but fitting all 'unwanted' lines to a multi-Voigt profile (which is suitable to reproduce DINS ToF signals typical of Gaussian momentum distribution functions [145]), and subtracting the fit. This trick allows for skipping an enhancement of noise that would severely impact the assessment of the mean kinetic energy after y-transformation.
Constraints for the sample-holder signal are usually retrieved from empty-can experimental data[6].
Reduced ToF spectra are then transformed to the y-domain. From a practical point of view, every fixed-angle experimental NCP $F_n(Q, y)$ is obtained through

$$F_n(Q, y) = \frac{BM}{E_0 \Phi(E_0)} QC(t) \tag{5.5}$$

where E_0 is the incident neutron energy, $\Phi(E_0)$ the incident neutron spectrum, M the scatterer mass, $C(t)$ the fixed-angle neutron countrate, and B a constant that takes into account the detector solid angle, the detector efficiency at final energy

[5] An increase in flux would either need to be attenuated in backscattering to avoid detector saturation or be compensated by an increase of L_1. Alternatively, replacing ^{6}Li-doped detectors with YAPs, for which saturation is not an issue, would overcome this problem all together.

[6] If the signal from the sample-holder is strong (which is common with metals other than aluminum), the spectral contribution from the second Au resonance ($E_1 \sim 60.6$ eV) becomes non-negligible at short ToFs, and must be taken into account when fitting data against the background.

E_1, the time-energy Jacobian, the free-atom neutron/scatterer cross section, and the number of scatterers hit by the beam [147].
All $F_n(Q,y)$ hystograms are then rebinned and normalized to unit area according to the zero-order sum rule for the incoherent dynamic structure factor [137].
Given the generic n^{th} detector, the connection of $F_n(Q,y)$ to J_{IA}(y) is given by

$$F_n(Q,y) = [J_{IA}(y) + \Delta J_n(Q,y)] \otimes R_n(Q,y) = F_{IA}(y) + \Delta J_n(Q,y) \otimes R_n(Q,y) \quad (5.6)$$

where $\Delta J_n(Q,y)$ is the Q-dependent (usually at the lowest order) deviation from the impulse approximation (FSEs), whereas $R_n(Q,y)$ represents the fixed-angle instrumental resolution function the NCP is convoluted to. This latter function is usually recovered by means of a modified DINSMS Monte Carlo code[7] [140], which is employed to simulate DINS scattering from a polycrystalline Pb sample (currently used as a resolution calibration standard on VESUVIO [144]) since dominated by the spectrometer's resolution.
The following sum rules apply to any $R_n(Q,y)$ [134]

$$\int_{-\infty}^{+\infty} dy R_n(Q,y) = 1 \quad (5.7)$$

$$\int_{-\infty}^{+\infty} dy y^2 R_n(Q,y) = \sigma_n^2. \quad (5.8)$$

On the other hand, taking into account the properties of the moments of the convolution between two real functions, the sum rules for the experimental NCP $F_n(Q,y)$ look like

$$\int_{-\infty}^{+\infty} dy F_n(Q,y) = 1 \quad (5.9)$$

$$\int_{-\infty}^{+\infty} dy y^2 F_n(Q,y) = \sigma^2 + \sigma_n^2 = \frac{2M < E_k >}{3\hbar^2} + \sigma_n^2 \quad (5.10)$$

which prove valid for any momentum distribution lineshape, since they derive from the definition of probability density distributions with finite variance.
All fixed-angle F_ns' are finally averaged into an overall

$$\overline{F}(Q,y) = \sum_n \frac{1}{n} F_n(Q,y) \approx \overline{F}(y), \quad (5.11)$$

for which most of the Q-dependence gets smeared out as the contributions from different detectors accessing different Q-values associated to the same y are averaged. This average operation is intended to ease visual representation of the NCP, and can be exploited for a non-parametric determination of $< E_k >$ [134].
Accordingly, one finds

[7] This code provides a ToF neutron transport for scattering from model scattering kernels in the eV range, which include the main characteristics of the spectrometer: the transfer matrices of the energy analyzers, the velocity-dependent emission time from the moderator, a Gaussian probability distribution for the geometrical parameters, and multiple scattering [140].

$$\int_{-\infty}^{+\infty} dy\overline{F}(y) = 1 \tag{5.12}$$

$$\int_{-\infty}^{+\infty} dyy^2\overline{F}(y) = \sigma^2 + < \sigma_n^2 >= \frac{2M < E_k >}{3\hbar^2} + < \sigma_n^2 > \tag{5.13}$$

that is, $\overline{F}(y)$ accounts for both the variance of the global momentum distribution and the ones from single detectors.
The $J_{IA}(y)$ can be described according to different formalizations.
A well assessed picture to interpret the experimental J_{IA} curve in a quasi-harmonic context [46, 133, 145, 149, 150] consists of assuming the emergence of the momentum distribution from the spherical average of a multivariate anisotropic Gaussian distribution[8] (see Appendix D), i.e., an $n(p)$ shaped as

$$= \frac{1}{4\pi}\frac{1}{(2\pi)^{\frac{3}{2}}}\frac{1}{\sigma_x\sigma_y\sigma_z}\int_0^{2\pi} d\phi \int_0^{\pi} sin(\theta) e^{-\frac{1}{2}p^2(\frac{sin^2(\theta)cos^2(\phi)}{\sigma_x^2}+\frac{sin^2(\theta)sin^2(\phi)}{\sigma_y^2}+\frac{cos^2(\theta)}{\sigma_z^2})} d\theta \tag{5.14}$$

with the three directional variances directly related to the principal oscillation frequencies through

$$\sigma_i^2 = \frac{M\omega_i}{2\hbar} coth \frac{\beta\hbar\omega_i}{2} \tag{5.15}$$

and the ω_is' mainly consisting of weighted averages of stretching (ω_z), librational (ω_x), and a mix of bending and librational frequencies (ω_y), with redshifts due to additional network mode contributions, as well as softening caused by anharmonicity [47].
The corresponding J_{IA} is given by

$$J_{IA}(y) = \frac{\hbar}{2}\frac{1}{(2\pi)^{\frac{3}{2}}}\frac{1}{\sigma_x\sigma_y\sigma_z}\int_0^{2\pi} d\phi \int_0^{\pi} sin(\theta)\frac{1}{S(\theta,\phi)} e^{-\frac{S(\theta,\phi)}{2}\hbar^2y^2} d\theta \tag{5.16}$$

or, equivalently

$$F_{IA}(y) = \left[\frac{\hbar}{2}\frac{1}{(2\pi)^{\frac{3}{2}}}\frac{1}{\sigma_x\sigma_y\sigma_z}\int_0^{2\pi} d\phi \int_0^{\pi} sin(\theta)\frac{1}{S(\theta,\phi)} e^{-\frac{S(\theta,\phi)}{2}\hbar^2y^2} d\theta\right] \otimes R_n(Q,y) \tag{5.17}$$

where $S(\theta,\phi) = \frac{sin^2(\theta)cos^2(\phi)}{\sigma_x^2} + \frac{sin^2(\theta)sin^2(\phi)}{\sigma_y^2} + \frac{cos^2(\theta)}{\sigma_z^2}$.
On the other hand, $\forall n$ $\Delta F_n(Q,y)$ can be accounted for by a term [46, 137]

$$\Delta F_n(Q,y) = -A_3(Q)\frac{\partial^3 F_{IA}(y)}{\partial y^3} =$$

[8] A common choice in cases when anisotropy is more important, or more simple to measure, than potential deviations from harmonicity. A classical occurrence is ordinary ice I_h, where anisotropy stemming from the molecular orientations in the crystal has a larger effect on the momentum distribution than anharmonicity [149]. Yet ice does not behave like a harmonic crystal as the principal frequencies of the distribution differ from those of a harmonic crystal: anharmonicity, enhanced by H-bonding, is especially appreciable in librations and stretching.

$$= -A_3(Q)\left[\frac{\hbar^5}{2(2\pi)^{\frac{3}{2}}}\frac{1}{\sigma_x\sigma_y\sigma_z}\int_0^{2\pi}d\phi\int_0^{\pi}sin(\theta)e^{-\frac{S(\theta,\phi)}{2}\hbar^2y^2}[3S(\theta,\phi)y-\hbar^2S^2y^3]d\theta\right]\otimes R_n(Q,y) \tag{5.18}$$

with $A_3(Q)=\frac{m\nabla^2V}{36\hbar^2Q}$, as seen in paragraph 4.4.
The resulting ΔF_n term causes F_n to be non-symmetric about the origin (centroid of F_n slightly shifted to negative y-values), with an overall modulation in $F_{IA}(y)$.
A popular and alternative model-independent expression for J_{IA} is the one expressed in terms of a harmonic and isotropic 1D Gaussian curve modulated by a set of Hermite polynomials [133, 151]

$$J_{IA}(y)=\frac{e^{-\frac{y^2}{2\sigma^2}}}{\sqrt{2\pi}\sigma}\left[1+\sum_{n=2}^{\infty}\frac{a_n}{2^{2n}n!}H_{2n}\left(\frac{y}{\sqrt{2}\sigma}\right)\right]. \tag{5.19}$$

As above, the FSE-correction terms $\Delta J_n(Q,y)$ are formalized just retaining the lowest order ($O(\frac{1}{Q})$) of Sears' expansion[9] ($-A_3(Q)\frac{\partial^3 J_{IA}(y)}{\partial y^3}$), with

$$A_3(Q)=\frac{m\nabla^2V}{36\hbar^2Q} \tag{5.20}$$

and

$$-\frac{\partial^3 J_{IA}(y)}{\partial y^3}=J_{IA}(y)\frac{1}{\sigma^3 2^{\frac{3}{2}}}H_3\left(\frac{y}{\sqrt{2}\sigma}\right), \tag{5.21}$$

$H_3=8x^3-12x$ being the orthogonal Hermite polynomial [10] of order 3 [137, 151].
Whichever model is selected, the resulting $F_n(Q,y)$ gets numerically fitted [11] to all fixed-angle experimental data at the same time (in order not to neglect mutual effects due to unavoidable FSEs), taking into account all fixed-angle transformed resolutions, so to recover both the J_{IA}(y) lineshape and $< E_k >$.
Notice how the latter, Gauss-Hermite (GH) formalization has the virtue to require a very small computational time if compared to the 3D Gaussian (G3) model. Yet, the loss of info about anisotropy in the 1D Gaussian factor does not generally allow for a clear discrimination between anharmonic and anisotropic contributions globally included into the appended Hermite expansion.

5.3.2 The IP-file saga

As seen in paragraph 5.3.1, the asymmetric ΔF_n term causes a slight shift of the centroid of the NCP to negative y-values due to small, unavoidable FSEs.

[9] Indeed, the $\frac{1}{Q^2}$-contribution is generally so small that it can be safely neglected in analyzing data.

[10] Notice how, in the isotropic case, the FSE-terms from the two presented models coincide, apart from a multiplication factor.

[11] By the minimization of the statistical $\chi^2=\sum_{np}\frac{(F_n^{theo}(q_p,y_p)-F_n(q_p,y_p))^2}{\epsilon_{np}^2}$, where n is referred to any detector, p to any bin, and ϵ_{np}^2 is the error associated to each experimental point [152].

In the course of all our DINS measures, a suspicious large centroid deviation from zero - actually resembling a systematic error - was repeatedly found, which (being physics reasonably stable!) was immediately assigned to some unexpected modification in some of the instrumental parameters included in Eq. 5.4.
It is worth noticing here that data-reduction steps on VESUVIO require an input-parameter (IP) file, which contains info about all single-detector values for t_0, L_0, L_1 and scattering angle θ. The IP file is usually constructed making use of a self-consistent iterative procedure [144], which allows for the retrieval of θ and L_1 (once t_0, L_0 and E_1 are known) from both DINS and Bragg data for scattering from lead at room temperature. Precisely, under the IA the conservation of kinetic energy and momentum returns

$$\frac{v_1}{v_0} = \frac{cos\theta + \sqrt{\left(\frac{M}{m}\right)^2 - sin^2\theta}}{\frac{M}{m} + 1} \tag{5.22}$$

where M is the mass of the scatterer (Pb), m the neutron's, and $E_1 = \frac{1}{2}mv_1^2$.
On the other hand, VESUVIO's YAP detectors are covered with a thin foil of cadmium, which absorbs neutrons in the thermal region. The γ-ray emission associated with this absorption allows for the detection of neutrons with energies < 200 meV. The result is that scattering from Pb also produces Bragg peaks at very large ToFs ($> 2000\ \mu s$). Therefore, Bragg's law

$$2dsin\vartheta = \lambda \tag{5.23}$$

can be coupled to Eq. 5.22 in order to recover the above-mentioned parameters, once the tabulated lattice d-spacings for lead are known from the scientific literature.
I manually repeated the calibration procedure many times on Pb and other heavy elements in order to check the situation, more or less fixing the problem.
And direct inspection of the YAPs has recently spotted some dislocation of a few Cd foils from detector surfaces.
Stability monitoring and recalibrations are underway.
Life as an experimentalist.

6

Another perspective - Potential of mean force

Paix se fait à deux - et l'amour aussi

Charles de Leusse

6.1 The PMF

According to statistical mechanics, the probability of finding a system in one state or another is governed by the difference in free energy between those states. The advent of robust computational power has allowed for the systematic exploitation of computer-generated ensembles of system configurations for the computation of free-energy differences [153]. However, this task is not straightforward since it requires the sampling of the most probable configurations belonging to the states of interest, which may be hampered by a broad range of length- and time scales involved[1].
In the last 20 years a variety of methods has been proposed to efficiently skip this problem [154–156]. In one particular class of such techniques, when the potential of the intermolecular force consists of a sum of terms depending upon the relative coordinates of molecular pairs, the two states of interest are connected by a pathway, often referred to as the reaction coordinate, along which the free-energy profile can be determined, yielding the difference in free energy between the end states. This free-energy profile is usually called a potential of mean force (PMF), which is defined as the potential energy arising from the average force acting between any two fixed particles, where the average is taken over the ensemble of configurational states for the remaining $n-2$ particles.
The implementation of the PMF formalism dates back to the work set up by Kirkwood about liquid mixtures in mid 30s' [157].
Given the Helmoltz free energy $F = -k_B T ln Z$ of a system, with

$$Z = \frac{1}{h^{3N} N!} \int \int e^{-\frac{\mathcal{H}(\mathbf{p},\mathbf{q})}{k_B T}} d\mathbf{p} d\mathbf{q} \tag{6.1}$$

[1] For example, a polymer chain typically exhibits length scales ranging from the bond length ($\sim$ 1 Å) to the size of the chain ($O(10\,nm)$), and corresponding time scales ranging from a few femtoseconds for the bond vibrations up to the order of milliseconds or even seconds for the whole chain relaxation. For entangled systems the relaxation times can be even much longer [154].

the partition function - which is represented by a $6N$-dimensional integral over all generalized coordinates $\mathbf{q} = (q_1, ..., q_{3N})$ and their conjugate momenta $\mathbf{p} = (p_1, ..., p_{3N})$ - the probability of finding the system in a configuration defined by $\mathbf{p}$ and $\mathbf{q}$ is proportional to the Boltzmann factor

$$\pi(\mathbf{p}, \mathbf{q}) = \frac{e^{-\frac{\mathcal{H}(\mathbf{p},\mathbf{q})}{k_B T}}}{\int e^{-\frac{\mathcal{H}(\mathbf{p},\mathbf{q})}{k_B T}} d\mathbf{p}d\mathbf{q}} \tag{6.2}$$

so that the ensemble average $< A >$ of a quantity $A(\mathbf{p}, \mathbf{q})$ defined in terms of phase-space configurations $(\mathbf{p}, \mathbf{q})$ is simply

$$< A >= \frac{\int\int A(\mathbf{p}, \mathbf{q}) e^{-\frac{\mathcal{H}(\mathbf{p},\mathbf{q})}{k_B T}} d\mathbf{p}d\mathbf{q}}{\int\int e^{-\frac{\mathcal{H}(\mathbf{p},\mathbf{q})}{k_B T}} d\mathbf{p}d\mathbf{q}} = \int\int A(\mathbf{p}, \mathbf{q})\pi(\mathbf{p}, \mathbf{q}) d\mathbf{p}d\mathbf{q}. \tag{6.3}$$

The entire partition function is only computable for the smallest systems. Nonetheless, if one is only interested in differences in free energy, the problem gets tractable, because a *relative* free energy between two (metastable) states of a system may be expressed as an ensemble average the (easier) way we can witness in the right-hand side of Eq. 6.3.

In this case, following Trzesniak et al. [153], one can determine how the free energy changes as a function of the positions of a subset of system particles, expressing it as a function of a specific reaction coordinate, $R(\mathbf{q}) = R(q_1, ..., q_{3N})$, be it an H-bond distance, a torsional angle, or linear combinations of similar quantities [154].

The use of the coordinate R is a smart trick, since it allows for restricting the system to a hypersurface in the phase space, so that the free energy, F_R, the partition function, Z_R, and the end-to-end reaction-coordinate distribution function, P_R, become the relevant quantities to be determined on such a hypersurface.

The phase-space probability, $\pi_R(\mathbf{p}, \mathbf{q}; R')$, to find the system at a particular value R' of the reaction coordinate is given by

$$\pi_R(\mathbf{p}, \mathbf{q}; R') = \pi(\mathbf{p}, \mathbf{q})\delta(R' - R(\mathbf{q})) \tag{6.4}$$

which means, after integration over the phase space,

$$P_R(R') = \frac{\int\int e^{-\frac{\mathcal{H}(\mathbf{p},\mathbf{q})}{k_B T}} \delta(R' - R(\mathbf{q})) d\mathbf{p}d\mathbf{q}}{\int\int e^{-\frac{\mathcal{H}(\mathbf{p},\mathbf{q})}{k_B T}} d\mathbf{p}d\mathbf{q}} \tag{6.5}$$

or

$$Z_R(R') = \frac{1}{h^{3N} N!} \int\int e^{-\frac{\mathcal{H}(\mathbf{p},\mathbf{q})}{k_B T}} \delta(R' - R(\mathbf{q})) d\mathbf{p}d\mathbf{q} \tag{6.6}$$

from which

$$P_R(R') = \frac{Z_R(R')}{Z} \tag{6.7}$$

is retrieved, as well as

$$F_R(R') = -k_B T ln P_R(R') - k_B T ln Z. \tag{6.8}$$

$F_R(R')$ is our PMF along the reaction coordinate R, so that

$$F_R(R') = F_R(\infty) + \int_{\infty}^{R'} \frac{dF_R(R'')}{dR''} dR''; \tag{6.9}$$

whereas $f = -\frac{dF_R(R'')}{dR''}$ is the associated mean force (MF).

6.2 The MF and the neutron Compton profile

In the last ten years the interpretation of DINS observations about water has been based on extensive *ab initio* molecular-dynamics simulations [158], which show a good agreement between theory and experiment, but at the price of a large computational cost.
Indeed, be

$$\frac{1}{(2\pi\hbar)^3 Z} \int d\mathbf{r} d\mathbf{r}' e^{\frac{i}{\hbar}\mathbf{p}\cdot(\mathbf{r}-\mathbf{r}')} \rho(\mathbf{r},\mathbf{r}') = \frac{1}{(2\pi\hbar)^3} \int d\mathbf{x} e^{\frac{i}{\hbar}\mathbf{p}\cdot\mathbf{x}} \tilde{n}(\mathbf{x}) \tag{6.10}$$

the expression for the momentum distribution $n(\mathbf{p})$ in terms of the density matrix $\rho(\mathbf{r},\mathbf{r}') = \left\langle \mathbf{r}|\mathbf{e}^{-\beta H}|\mathbf{r}' \right\rangle$, where $\tilde{n}(\mathbf{x}) = \frac{1}{Z}\int d\mathbf{r} d\mathbf{r}' \delta(\mathbf{r}-\mathbf{r}'-\mathbf{x})\rho(\mathbf{r},\mathbf{r}')$; and

$$Z = \int d\mathbf{r} \rho(\mathbf{r},\mathbf{r}') \tag{6.11}$$

the one for the partition function Z. One immediately sees that the former involves the off-diagonal terms of ρ, while the latter is only determined by diagonal contributions.
In a condensed system statistical sampling is the only viable computational strategy. A common choice is using the Feynman path integral (PI) representation, within which $\tilde{n}(\mathbf{x})$ is an end-to-end distribution of a sum over open paths, while closed ones determine Z (see Appendix F). Sampling is usually done on the closed paths and it is challenging from these simulations to estimate the open-path distribution that determines $n(\mathbf{p})$ [159].
One approach is to artificially open a fraction of the paths [160], but this implies a balance of two contradictory requirements: on the one hand, the number of open paths has to be large enough to make statistics for $\tilde{n}(\mathbf{x})$ good; on the other hand, if that number is too large the sampling gets incorrect.
Yet, a good trick to save both sampling accuracy and statistics is given in [159].
In the Feynman's PI representation the density matrix is expressed as

$$\rho(\mathbf{r},\mathbf{r}') = \int_{\mathbf{r}(0)=\mathbf{r},\mathbf{r}(\beta\hbar)=\mathbf{r}'} \mathfrak{D}\mathbf{r}(\tau) e^{-\frac{1}{\hbar}\int_0^{\beta\hbar} d\tau \left(\frac{m\dot{\mathbf{r}}^2(\tau)}{2} + V[\mathbf{r}(\tau)]\right)} \tag{6.12}$$

while the end-to-end distribution is given by

$$\tilde{n}(\mathbf{x}) = \frac{1}{Z}\int d\mathbf{r} d\mathbf{r}' \delta(\mathbf{r}-\mathbf{r}'-\mathbf{x})\rho(\mathbf{r},\mathbf{r}') = \frac{\int_{\mathbf{r}(0)-\mathbf{r}(\beta\hbar)=\mathbf{x}} \mathfrak{D}\mathbf{r}(\tau) e^{-\frac{1}{\hbar}\int_0^{\beta\hbar} d\tau \left(\frac{m\dot{\mathbf{r}}^2(\tau)}{2} + V[\mathbf{r}(\tau)]\right)}}{\int_{\mathbf{r}(\beta\hbar)-\mathbf{r}(0)} \mathfrak{D}\mathbf{r}(\tau) e^{-\frac{1}{\hbar}\int_0^{\beta\hbar} d\tau \left(\frac{m\dot{\mathbf{r}}^2(\tau)}{2} + V[\mathbf{r}(\tau)]\right)}}. \tag{6.13}$$

If the following linear transformation in the path space is performed

$$\mathbf{r}(\tau) = \tilde{\mathbf{r}}(\tau) + y(\tau)\mathbf{x} \tag{6.14}$$

where $y(\tau) = C - \frac{\tau}{\beta\hbar}$ and C is any real constant[2], the numerator in Eq. 6.13 is changed to

$$\int_{\mathbf{r}(0)-\mathbf{r}(\beta\hbar)=\mathbf{x}} \mathfrak{D}\mathbf{r}(\tau) e^{-\frac{1}{\hbar}\int_0^{\beta\hbar} d\tau \left(\frac{m\dot{\mathbf{r}}^2(\tau)}{2} + V[\mathbf{r}(\tau)]\right)} =$$

$$= e^{-\frac{m\mathbf{x}^2}{2\beta\hbar^2}} \int_{\tilde{\mathbf{r}}(\beta\hbar)=\tilde{\mathbf{r}}(0)} \mathfrak{D}\mathbf{r}(\tau) e^{-\frac{1}{\hbar}\int_0^{\beta\hbar} d\tau \left(\frac{m\dot{\mathbf{r}}^2(\tau)}{2} + V[\tilde{\mathbf{r}}(\tau)+y(\tau)\mathbf{x}]\right)}. \tag{6.15}$$

The sense of transformation 6.14 is reshaping the open path $\mathbf{r}(\tau)$ into the closed path $\tilde{\mathbf{r}}(\tau)$, with the free particle contribution coming naturally from the derivative of $y(\tau)$.
On the other hand, given our NCP

$$J = \hbar \int n(\mathbf{p}')\delta\left(\hbar y - \hat{\mathbf{Q}}\cdot\mathbf{p}'\right) d\mathbf{p}', \tag{6.16}$$

the momentum distribution can be expressed in terms of the end-to-end distribution

$$n(\mathbf{p}) = \frac{1}{2\pi\hbar^3} \int d\mathbf{x} e^{\frac{i}{\hbar}\mathbf{p}\cdot\mathbf{x}} \tilde{n}(\mathbf{x}) \tag{6.17}$$

or, equivalently, if $x_\parallel = \mathbf{x}\cdot\hat{\mathbf{Q}}$ is the projection of $\mathbf{x}$ along $\hat{\mathbf{Q}}$ [159],

$$J = \frac{1}{2\pi\hbar} \int dx_\parallel \tilde{n}(x_\parallel \hat{\mathbf{Q}}) e^{\frac{i}{\hbar}x_\parallel y}. \tag{6.18}$$

Being

$$\tilde{n}(\mathbf{x}) = e^{-\frac{m\mathbf{x}^2}{2\beta\hbar^2}} e^{-\beta U(\mathbf{x})}, \tag{6.19}$$

with U the PMF, along the $\mathbf{Q}$-direction one finds

$$U(x_\parallel\hat{\mathbf{Q}}) = -\frac{mx_\parallel^2}{2\beta^2\hbar^2} - \frac{1}{\beta}\ln\int dy' J(y', \hat{\mathbf{Q}}) e^{\frac{i}{\hbar}x_\parallel y'}. \tag{6.20}$$

The gradient of the PMF returns the projection the MF along the same direction

$$\hat{\mathbf{Q}}\cdot\mathbf{F}(x_\parallel\hat{\mathbf{Q}}) = -\frac{mx_\parallel}{\beta^2\hbar^2} + \frac{1}{\beta\hbar}\frac{\int_0^\infty y' \sin(\frac{x_\parallel y'}{\hbar}) J(y', \hat{\mathbf{Q}}) dy'}{\int_0^\infty dy' \cos(\frac{x_\parallel y'}{\hbar}) J(y', \hat{\mathbf{Q}})} \tag{6.21}$$

that is, taking into account the scaling property of the J-function,

$$\hat{\mathbf{Q}}\cdot\mathbf{F}(x_\parallel\hat{\mathbf{Q}}) = -\frac{mx_\parallel}{\beta^2\hbar^2} + \frac{1}{\beta}\frac{\int_0^\infty y \sin(x_\parallel y) J(y, \hat{\mathbf{Q}}) dy}{\int_0^\infty dy \cos(x_\parallel y) J(y, \hat{\mathbf{Q}})}. \tag{6.22}$$

[2] C influences the variance of the free energy perturbation and thermodynamic integration estimators. Lin et al. found [159] that the lowest variance is achieved when $C = \frac{1}{2}$, since this choice returns the smallest displacement from the closed path configuration.

6.3 Anisotropy vs anharmonicity

As seen in paragraph 5.3.1 (and Appendix D), the NCP associated to the spherical average of a momentum distribution modeled as a 3D anisotropic multinormal function is given by

$$J_{IA}(y) = \frac{\hbar}{2}\frac{1}{(2\pi)^{\frac{3}{2}}}\frac{1}{\sigma_x\sigma_y\sigma_z}\int_0^{2\pi} d\phi \int_0^{\pi} sin(\theta)\frac{1}{S(\theta,\phi)}e^{-\frac{1}{2}S(\theta,\phi)\hbar^2y^2}d\theta, \tag{6.23}$$

where $S(\theta,\phi) = \frac{sin^2(\theta)cos^2(\phi)}{\sigma_x^2} + \frac{sin^2(\theta)sin^2(\phi)}{\sigma_y^2} + \frac{cos^2(\theta)}{\sigma_z^2}$.
That means that, in the special case of an isotropic system, J_{IA} becomes a simple univariate Gaussian: indeed, being $S(\theta,\phi) = \frac{1}{\sigma^2}$ and exploiting our usual scale invariance, one finds

$$J_{IA}(y) = \frac{\hbar}{2}\frac{1}{(2\pi)^{\frac{3}{2}}}\frac{1}{\sigma}e^{-\frac{\hbar^2y^2}{2\sigma^2}}\int_0^{2\pi} d\phi \int_0^{\pi} sin(\theta)d\theta = \frac{\hbar}{\sqrt{2\pi}\sigma}e^{-\frac{\hbar^2y^2}{2\sigma^2}} = \frac{1}{\sqrt{2\pi}\sigma}e^{-\frac{y^2}{2\sigma^2}}. \tag{6.24}$$

When this happens, the MF turns out linear; precisely, in this case Eq. 6.22 returns

$$\hat{\mathbf{Q}}\cdot\mathbf{F}(x_\parallel\hat{\mathbf{Q}}) = -\frac{mx_\parallel}{\beta^2\hbar^2} + \frac{1}{\beta}\frac{\frac{\sqrt{\pi}}{4}(2\sigma^2)^{\frac{3}{2}}x_\parallel e^{-\frac{\sigma^2}{2}x_\parallel^2}}{\frac{\sqrt{\pi}}{2}(2\sigma^2)^{\frac{1}{2}}e^{-\frac{\sigma^2}{2}x_\parallel^2}} = \left(-\frac{m}{\beta^2\hbar^2} + \frac{\sigma^2}{\beta}\right)x_\parallel, \tag{6.25}$$

which clearly establishes an analytic linearity in the reaction coordinate $x_\parallel$.
But what about the anisotropic case?
In principle, if *no* spherical average of the NCP were performed, a decoupled 3D harmonic potential would still produce a linear MF, being any deviation from linearity safely ascribable to the anharmonic behavior of the local potential itself.
Yet, from an experimental point of view, the spherically averaged $n(p)$ is usually the only available information in DINS (see Appendix D), and, in such a situation, telling truly anharmonic- from averaged anisotropic contributions to the the NCP can prove an uneasy task.
A taste of this problem can be gotten by a simple concept test involving the numerical evaluation and comparison - at fixed temperature (100 K) - of the MFs of two hypothetical systems, namely one marked by the spherical average of a 3D Gaussian momentum distribution characterized by a robust anisotropy (with average variance $\overline{\sigma}_{aniso}$), and one completely isotropic with $\sigma_{iso} = \overline{\sigma}_{aniso}$ (Fig. 6.1).
Fig. 6.2 shows how, while the numerical evaluation performed on the isotropic system returns a linear MF overlapping the analytic result from Eq. 6.22, the MF for the anisotropic harmonic system only follows the linear trend for small values of $x_\parallel$, then shifting to a smoother increase due to the spherical-averaging process.
So, how to get a hint of anharmonicity beyond anisotropy by inspection of MF data?
To answer this question, another test was made starting from the same strongly anisotropic system at 100 K, whose momentum distribution was this time reconstructed as the spherical average of one anharmonic contribution along the direction of the O-H stretch (z axis; see Fig. 7.7) and two harmonic components along x and y, respectively.

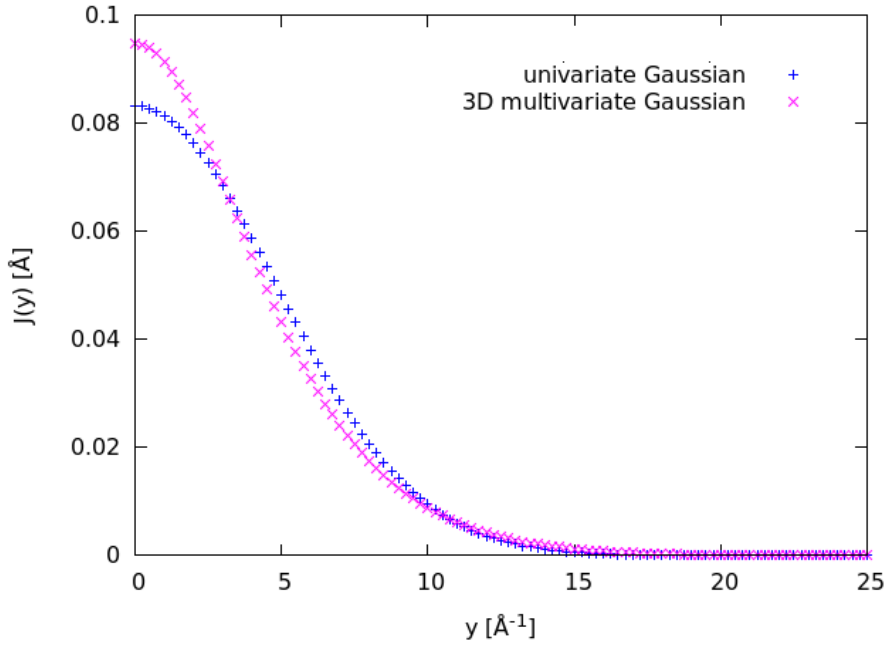

Figure 6.1: Reconstructed half NCPs (at 100 K) for: a) a hypothetical system with (sperically averaged) multivariate Gaussian momentum distribution, having $\sigma_x = 2.0$ Å^{-1}, $\sigma_y = 4.0$ Å^{-1}, $\sigma_z = 7.0$ Å^{-1}, and $\overline{\sigma}_{aniso} = 4.796$ Å^{-1} (magenta); b) a hypothetical system with univariate Gaussian momentum distribution, having $\sigma_{iso} = 4.796$ Å^{-1} (blue). Generated via Gnuplot 4.6.

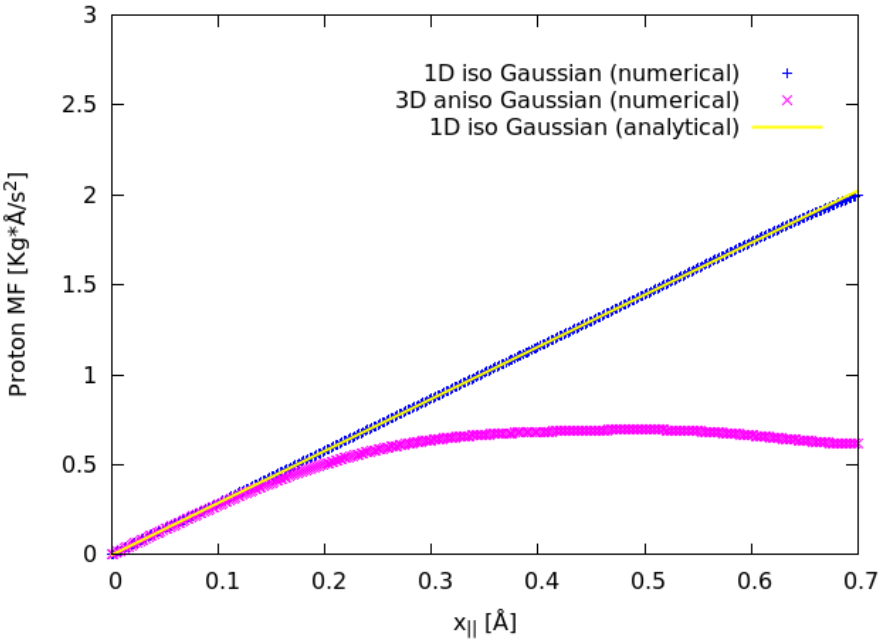

Figure 6.2: Reconstructed MFs at 100 K for: a) a hypothetical system with (spherically averaged) 3D multivariate Gaussian momentum distribution, having $\sigma_x = 2.0$ Å^{-1}, $\sigma_y = 4.0$ Å^{-1}, $\sigma_z = 7.0$ Å^{-1}, and $\overline{\sigma}_{aniso} = 4.796$ Å^{-1} (magenta); b) a hypothetical system with univariate Gaussian momentum distribution, having $\sigma_{iso} = 4.796$ Å^{-1} (blue). The yellow line represents the analytical result from Eq. 6.22. Generated via Gnuplot 4.6.

If one reasons in terms of single-nucleus motion in an effective potential, if the three components of the wavefunction of the system are decoupled, and if the anharmonic contribution to the eigenfunction $\overline{\psi}(\mathbf{p})$ of the ground state in the momentum space is modeled as resulting from a Morse-oscillator motion (see Appendix E), then the $\hat{p}$ spherical average of the momentum distribution at fixed orientation $\mathbf{\Theta_d}$ is given by

$$n(p) =< n(\mathbf{p}, \mathbf{\Theta_d}) >_{\hat{p}} = \frac{1}{16\pi^3} \frac{2^{\lambda_z - 1}}{\sigma_x \sigma_y \alpha_z \hbar} \frac{2\lambda_z - 1}{\Gamma(2\lambda_z)} \int_0^{2\pi} d\phi \times$$

$$\times \int_0^{\pi} d\theta sin(\theta) e^{-\frac{p^2}{2}\left(\frac{sin^2(\theta)cos^2(\phi)}{\sigma_x^2} + \frac{sin^2(\theta)sin^2(\phi)}{\sigma_y^2}\right)} \left|\Gamma\left(\lambda_z - \frac{1}{2} + i\frac{pcos(\theta)}{\alpha_z \hbar}\right)\right|^2 \qquad (6.26)$$

from which

$$J_{IA}(y) = 2\pi\hbar \int_{|\hbar y|}^{\infty} p < n(\mathbf{p}, \mathbf{\Theta_d}) >_{\hat{p}} dp = \frac{\hbar}{8\pi^2} \frac{2^{\lambda_z - 1}}{\sigma_x \sigma_y \alpha_z \hbar} \frac{2\lambda_z - 1}{\Gamma(2\lambda_z)} \int_0^{2\pi} d\phi \int_0^{\pi} sin(\theta) d\theta \times$$

$$\times \int_{|\hbar y|}^{\infty} p e^{-\frac{p^2}{2}\left(\frac{sin^2(\theta)cos^2(\phi)}{\sigma_x^2} + \frac{sin^2(\theta)sin^2(\phi)}{\sigma_y^2}\right)} \left|\Gamma\left(\lambda_z - \frac{1}{2} + i\frac{pcos(\theta)}{\alpha_z \hbar}\right)\right|^2 dp, \qquad (6.27)$$

to be evaluated numerically.
That said, if m is the mass of the scatterer (hydrogen nucleus) and $D_z\alpha_z^2$ is recovered from

$$\sigma_z = \left[\frac{m}{2\hbar}\sqrt{\frac{2D_z\alpha_z^2}{m}} coth\left(\frac{\beta\hbar}{2}\sqrt{\frac{2D_z\alpha_z^2}{m}}\right)\right]^{\frac{1}{2}}, \qquad (6.28)$$

one can use values of α_z or D_z tabulated in the literature [149, 161] in order to get the other parameter separately, as well as λ_z.
The numerical computation from $J_{IA}(y)$ of the MF for our anharmonic and anisotropic system is reported in Fig. 6.3. In comparison to the anisotropic harmonic case, the trend of this MF in case of mild anharmonicity ($x_e = 0.032$) is only slightly different. Conversely, a strong anharmonicity ($x_e = 3.19$) clearly induces a change in the slope of the curve for small values of the reaction coordinate already.
Yet, it must be noticed that, in spite of its ability to accurately reproduce important quantum effects in water - such as experimentally observed H/D fractionation ratios [41] - this Morse modeling of the covalent O−H bond completely neglects anharmonic effects along the hydrogen-bond direction, which could actually have non-trivial influence on the overall shape of the mean force.

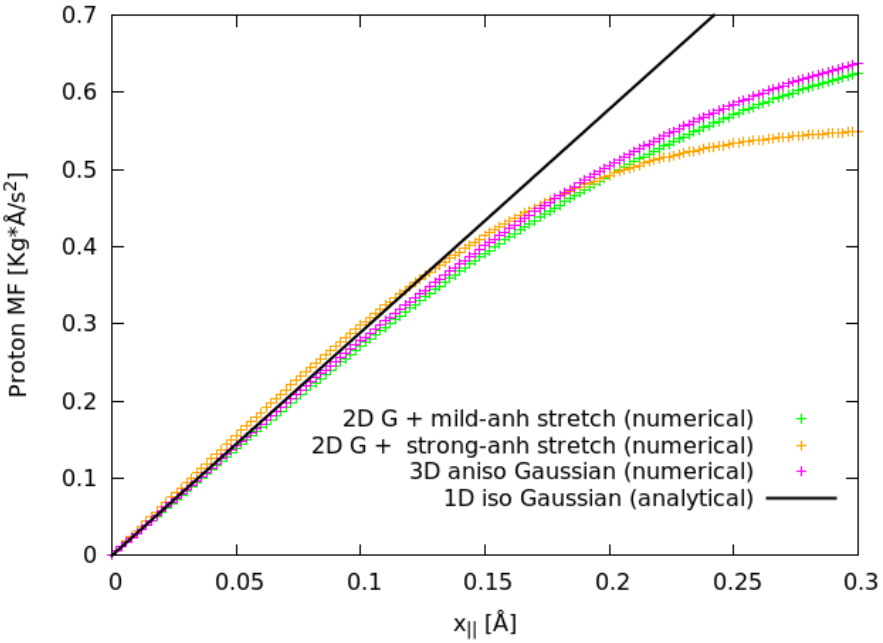

Figure 6.3: Reconstructed MFs at 100 K for: a) a hypothetical system with (spherically averaged) 3D multivariate Gaussian momentum distribution, having $\sigma_x = 2.0$ Å^{-1}, $\sigma_y = 4.0$ Å^{-1}, $\sigma_z = 7.0$ Å^{-1}, and $\overline{\sigma}_{aniso} = 4.796$ Å^{-1} (magenta); b) same system with (spherically averaged) momentum distribution consisting of two harmonic contributions (along x and y directions) and a mild anharmonic component (anharmonic constant $x_e = 0.032$) along the direction of the O-H stretch (green); c) same system with (spherically averaged) momentum distribution consisting of two harmonic contributions and a strong anharmonic component ($x_e = 3.19$) along the direction of the O-H stretch (orange). The black line represents the analytical result from Eq. 6.22. Generated via Gnuplot 4.6.

7

Ok, what then? - Experimental results

Experience is the adornment of rigpa

Tulku Urgyen Rinpoche

7.1 The AIs

The experiment described in this paragraph includes a set of DINS and INS measurements.
The batch of samples comprised three bulk-ice specimens, namely vHDA, uHDA, and LDA-I.
Part of the experimental team prepared uHDA by isothermal (77 K) compression of ice I_h inside a pyston cylinder with the aid of a hydraulic press, while vHDA was recovered by isobaric (1.1 GPa) heating of uHDA according to the routes signaled in Table 2.1. After recovery in liquid nitrogen at standard pressure and characterization by powder X-ray diffraction and Raman spectroscopy[1], the refrigerated cans were filled and shipped to ISIS in a liquid-N_2 transport dewar, in order to be mounted on the instrument under cryogenic conditions using a closed-cycle refrigerator.
Conversely, LDA-I was prepared *in-situ* at ISIS by isobaric heating of uHDA (Table 2.1) inside the cryostat [1].
A $(5.00 \times 5.00 \times 0.25)$-cm^3 copper can was chosen in order to ensure an optimal separation of recoil peaks from Cu and oxygen. A flat plate was the selected geometry, with a pierced 1.5-mm-thick Al spacer (Fig. 7.1). The plate was placed orthogonal to the neutron beam.
No indium wire was inserted into the can groove in order to allow the vaporized nitrogen shell to escape the can at 80 K and give no signal contribution to the spectra.
At the end of the experiment, a weight assessment of the content of the can was performed for vHDA by absorption of the liquefied ice on a paper tissue of known weight and subsequent weighing of the soaked object: by difference (0.9298 ± 0.0002) g of net material were retrieved, corresponding to 0.1 mol hydrogen $(0.6 \cdot 10^{23}$ atoms)

[1] Raman spectra were recorded by a Renishaw Ramascope spectrometer (632.8 nm) at 80 K in an Oxford Microstat^N cryostat. Calibration was performed using the sharp emission lines of a neon discharge lamp [162].

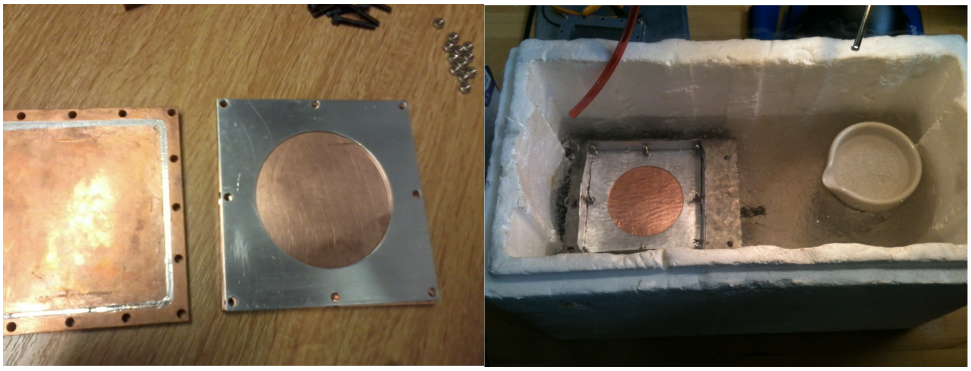

Figure 7.1: Left: Empty copper can with Al spacer used for DINS measurements on AIs. Right: Same can with ice sample in liquid nitrogen.

and 0.05 mol oxygen ($0.3 \cdot 10^{23}$ atoms), with propagated uncertainties of the order of 10^{-5} and 10^{18} for moles and numbers of atoms, respectively. A subsequent estimate of sample amounts for the remaining AIs was obtained by comparison of simulated- to experimental raw data and the aid of density ratios between sample pairs.
All DINS scans were performed at (80.00 ± 0.01) K at standard pressure.
Each AI measurement called for a total integrated proton[2] current of 4500 μAh.
Being interested in the ^{1}H-signal, the response from the forward-scattering detectors only was taken into account[3].
All fixed-angle (i.e., single-detector) ToF spectra,then corrected for γ- (minor correction) and multiple-scattering (MS) background, were retrieved by the procedure described in paragraph 5.3.1.
An example of the comparison of experimental γ-corrected- to simulated spectra is reported in Fig. 7.2 for a large- and small-angle detector, respectively, in the case of vHDA.
Next, every non-^{1}H line was subtracted with the aid of a multi-Voigt fit procedure (see Fig. 7.3 for an example on vHDA), with constraints for the Cu signal recovered from empty-can data and in the presence of a non-negligible contribution from the second gold resonance around 100 μs.
The resulting hydrogen ToF spectra were then transformed to the y-domain to recover an equal number of $F_n(Q, y)$ hystograms, which were then rebinned and normalized to unit area. For visual representation, the hystograms were averaged into an overall $\overline{F}(y)$ (Fig. 7.4), whose correspondent radial momentum distribution is given in Fig.7.5 for each AI.
The $F_n(Q, y)$'s were simultaneously fitted to a multivariate Gaussian model[4], with

[2] From the synchrotron.

[3] Being nearly isobaric with the neutron, hydrogen does not backscatter this probe in the epithermal region for kinematic reasons, provided that only single-scattering events are considered.
Indeed, the backscattering detector banks prove of interest for measurements on heavier masses, and particularly for systems containing multiple masses one needs to examine simultaneously [142].

[4] Just out of curiosity, a parallel, isotropic multi-fit was performed via the alternative model-independent formalization of the F_n curves described in paragraph 5.3.1. Only the purely Gaussian term of the expansion was retained, corresponding to a Maxwell-Boltzmann distribution in terms of $n(\mathbf{p})$. This caused a severe underestimation of the variance, seemingly due a miscounting of quantum effects in ice as theoretically anticipated in [149].

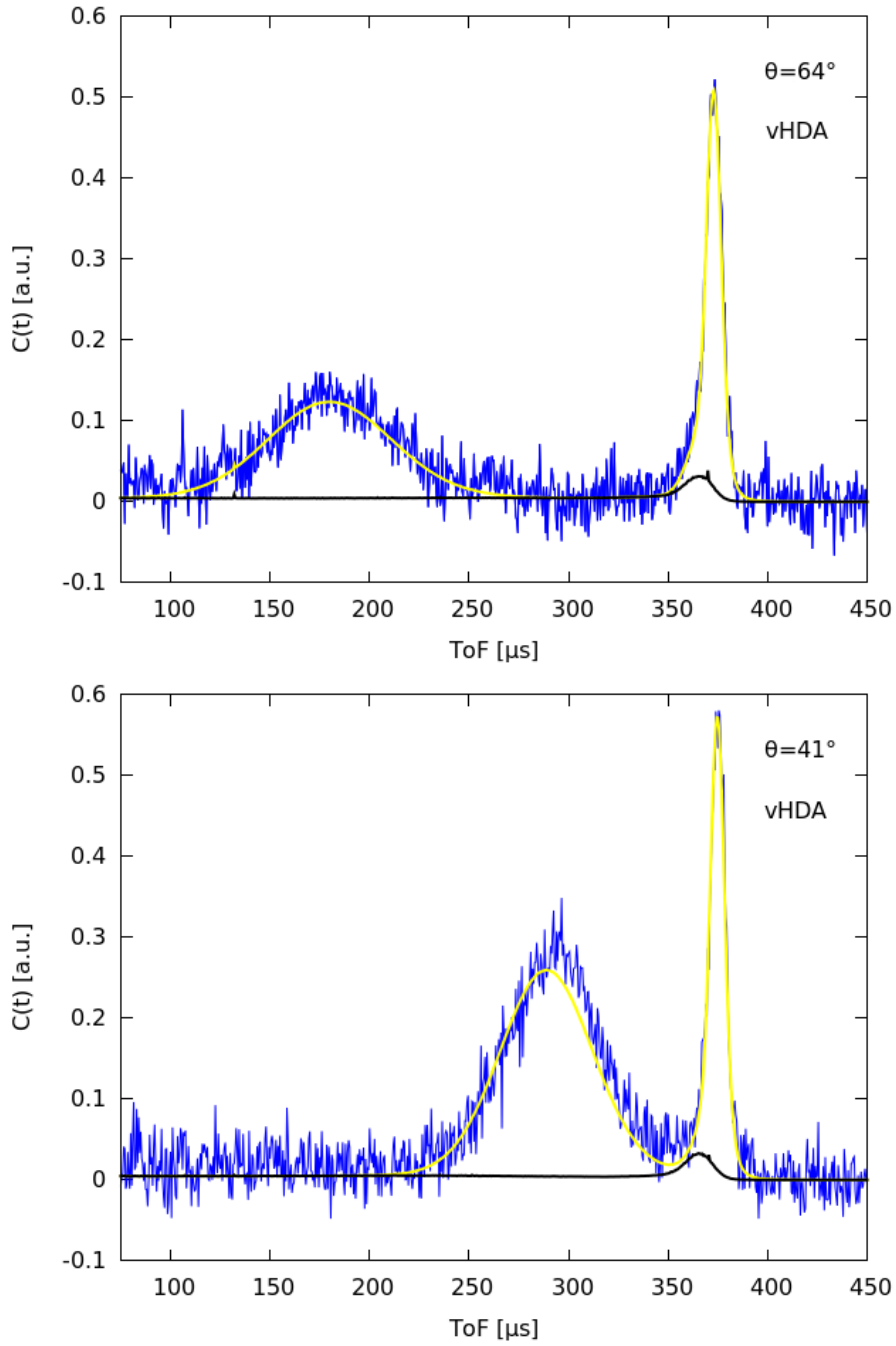

Figure 7.2: Top: Experimental γ-corrected spectrum at a scattering angle $\theta = 64°$ (blue), overall signal simulation up to the fourth order of scattering (single scattering + MS, yellow), and MS up to the fourth order of scattering (black). Bottom: Same plot at a scattering angle $\theta = 41°$. Notice how the ^{1}H signal at the smaller angle is shifted towards larger ToFs if compared to the simulated counterpart: this depends on the simulation code not taking FSEs into account (the effect looks negligible on heavier masses). Nevertheless, the features of ^{1}H scattering orders higher than the first are no way affected, so that MS can be correctly subtracted anyway. Generated via Gnuplot 4.6.

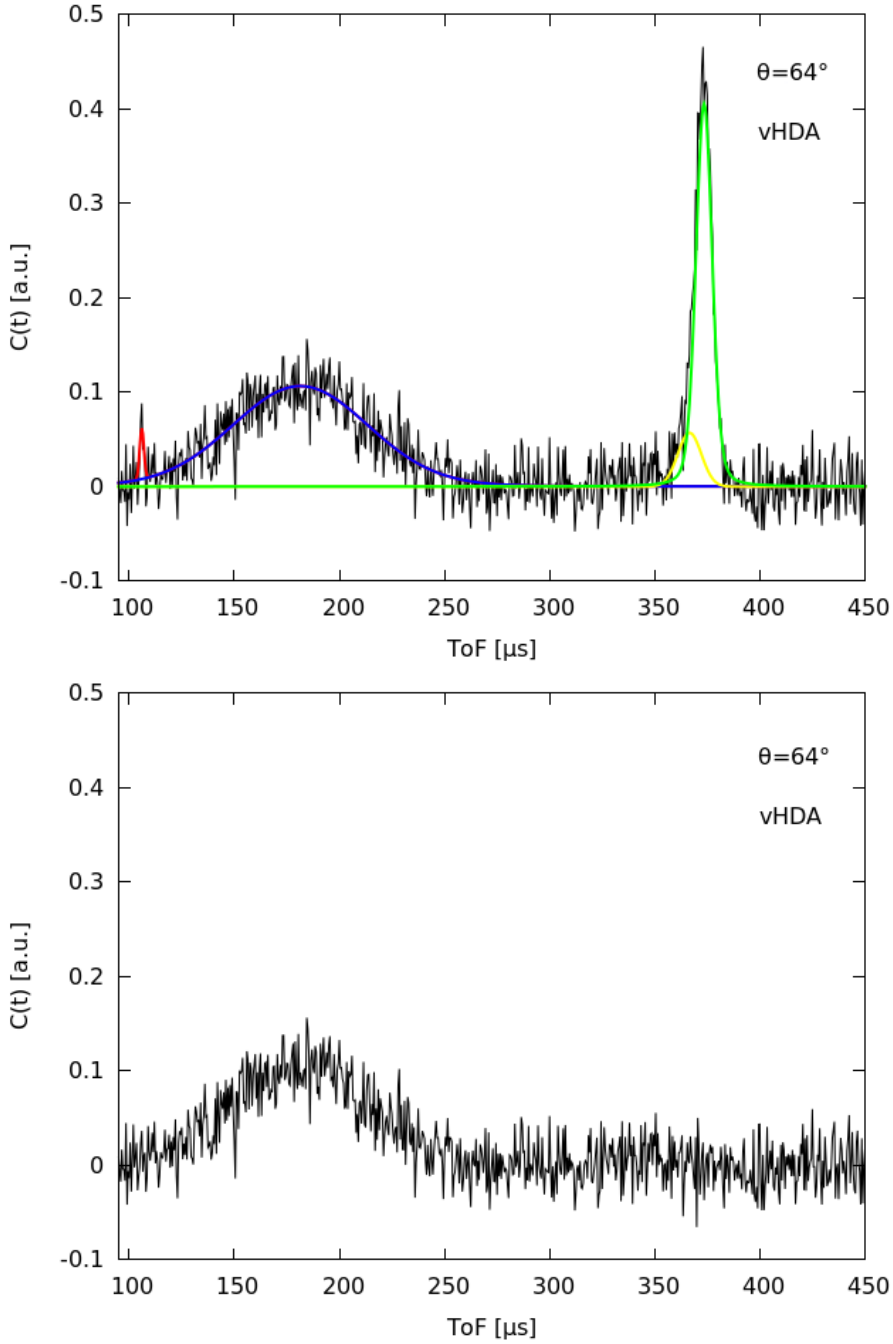

Figure 7.3: Top: Experimental γ- and MS-corrected spectrum at a scattering angle $\theta = 64°$ (black) superimposed to the Voigt fit of the 2^{nd} Au resonance (red), hydrogen (blue), oxygen (yellow), and copper (green) lines. Bottom: Same experimental spectrum after subtraction of all non-^{1}H fit curves. Generated via Gnuplot 4.6.

average results given in Fig. 7.4 for the three of the AI samples (resolutions shown in this figure come from an analogous average over single-detector terms retrieved by simulation[5]).
Table 7.1 reports related energy- and directional-variance estimates, with Fig. 7.6 visually conveying the increase in σ_α-anisotropy as density gets higher.

[5]Precisely, the resolution was determined by a 10^9-event Monte Carlo simulation of a hydrogen-containing sample having an isotropic Gaussian momentum distribution with $\sigma_{res} = (5 \times 10^{-3})$ Å^{-1} [134].

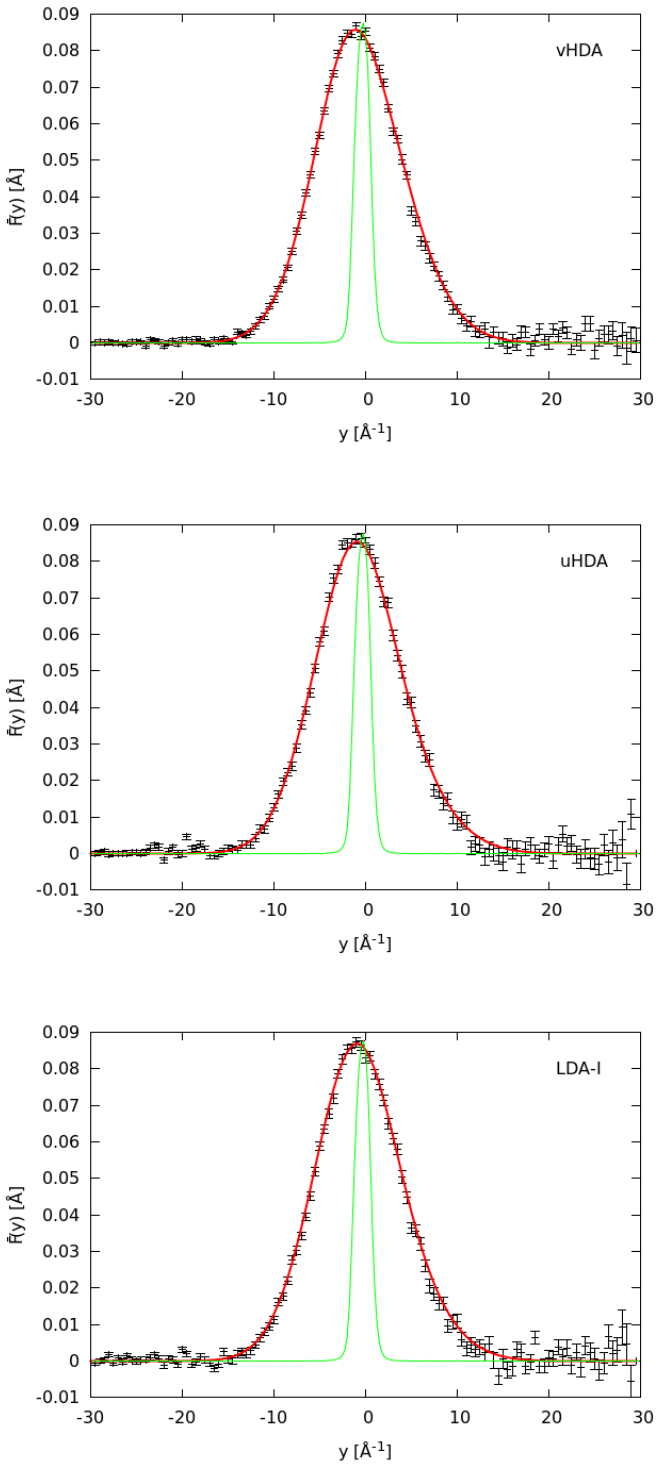

Figure 7.4: Experimental NCP (black) + multivariate-Gaussian fit (red) + (rescaled) simulated resolution curve (green) for vHDA (top), uHDA (center), and LDA-I (bottom), respectively. Generated via Gnuplot 4.6.

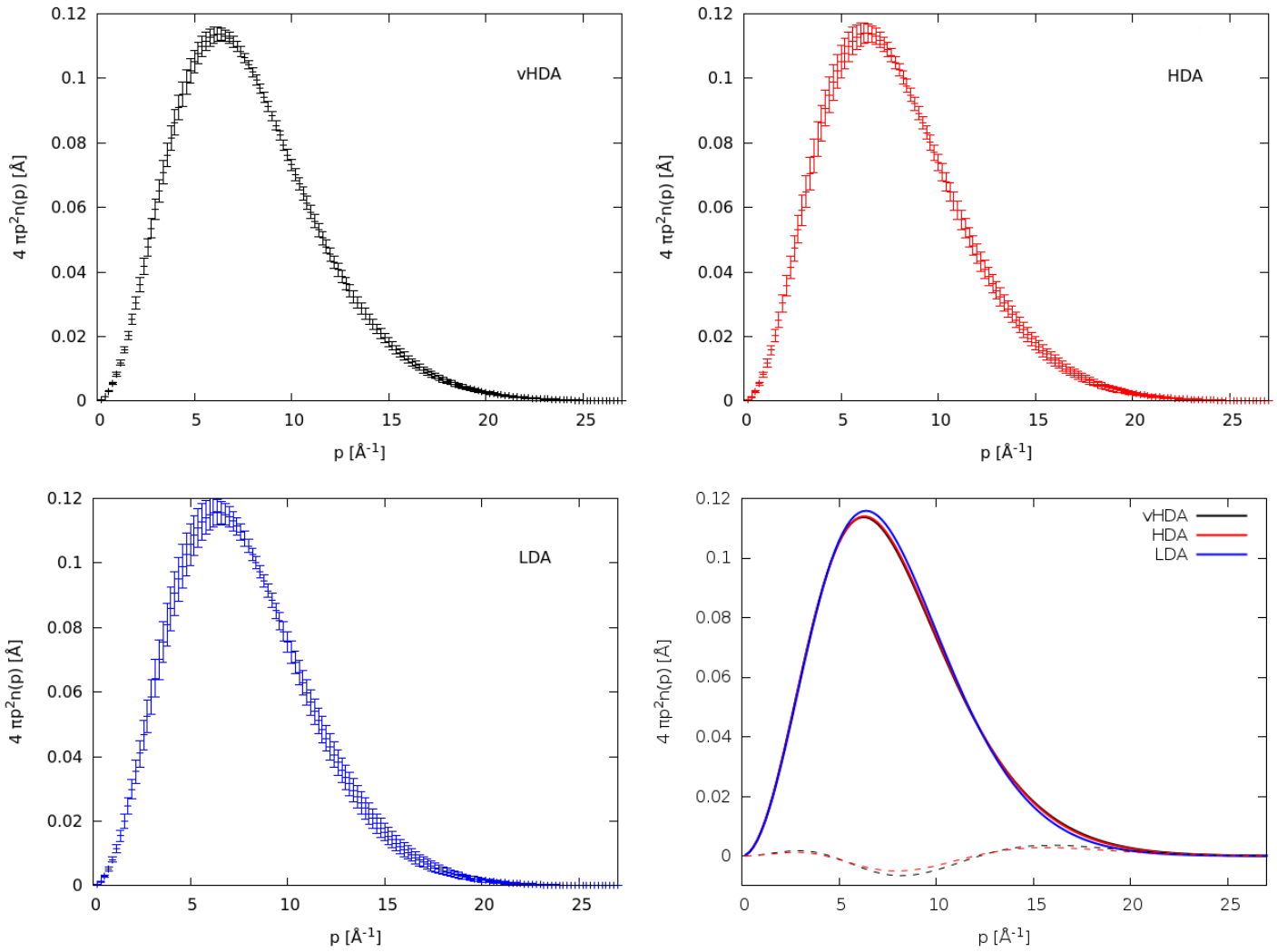

Figure 7.5: Radial momentum distribution for vHDA (top left), uHDA (top right), and LDA-I (bottom left). The three distributions are superimposed (bottom right) to highlight differences (no errorbars shown to preserve clarity). Dashed lines represent differences of vHDA and uHDA with respect to LDA-I (2X magnification). Generated via Gnuplot 4.6.

Table 7.1: Total + directional energy- and variance estimates for DINS and INS AI data. DINS estimates for the AIs come from the multivariate-Gaussian fit of y-data described in paragraph 5.3.1. DINS estimates for ice I_h are from [163] with density value from [164]. INS estimates for the whole of ice data have been recovered via the harmonic model described in [47].

	I_h DINS	I_h INS	LDA DINS	LDA INS	uHDA DINS	uHDA INS	vHDA DINS	vHDA INS
ρ $[\frac{g}{cm^3}]$	0.934	0.934	0.94	0.94	1.15	1.15	1.25	1.25
T [K]	71	80	80	80	80	80	80	80
$< E_k >_x$ [meV]	-	20.5 ± 1.0	19.5 ± 2.0	18.8 ± 1.0	18.5 ± 2.0	17.9 ± 1.0	18.7 ± 1.0	17.8 ± 1.0
$< E_k >_y$ [meV]	-	33.4 ± 1.0	49.6 ± 3.0	33.4 ± 1.0	44.1 ± 3.0	33.1 ± 1.0	41.4 ± 1.0	33.0 ± 1.0
$< E_k >_z$ [meV]	-	98.9 ± 1.0	83.3 ± 6.0	99.2 ± 1.0	94.8 ± 5.0	100.0 ± 1.0	98.7 ± 3.0	101.0 ± 1.0
$< E_k >$ [meV]	152.8 ± 1.6	153.0 ± 3.0	152.0 ± 3.0	151.0 ± 2.0	157.0 ± 3.0	152.0 ± 2.0	159.0 ± 3.0	151.0 ± 2.0
σ_x [Å^{-1}]	-	-	3.07 ± 0.14	-	2.99 ± 0.14	-	3.00 ± 0.10	-
σ_y [Å^{-1}]	-	-	4.89 ± 0.16	-	4.61 ± 0.12	-	4.47 ± 0.08	-
σ_z [Å^{-1}]	-	-	6.34 ± 0.22	-	6.76 ± 0.17	-	6.90 ± 0.12	-
σ [Å^{-1}]	-	-	4.95 ± 0.05	-	5.03 ± 0.05	-	5.05 ± 0.05	-

Following [47], x, y and z for ^{1}H axes are defined as shown in Fig. 7.7. Accordingly, $< E_k >_z$ defines the mean kinetic energy component along the O-H stretching direction, which is the major contribution to the overall increase in the ground-state $< E_k >$ with density signaled[6] in Table 7.1, and the reason for the corresponding increasing curve-width at $p > 12$ Å^{-1} reported in Fig. 7.5.
Such increase is coherent with the AIs' structural differences described in paragraph 2.3: the lower the density, the more compact the structure; the more compact the structure (stronger intermolecular H-bonds), the weaker O-H stretching (due to stronger quantum anharmonic fluctuations of intramolecular covalent bonds [42]); the weaker O-H stretching, the lower the value of the total mean kinetic energy for hydrogen scatterers[7].
Also notice how the difference in $< E_k >$ for LDA-I and I_h is small: this may look in agreement with LDA being just considered a defected form of crystalline ice, and not a true glass (like uHDA and vHDA should seemingly be). Conversely, uHDA and vHDA are far from each other in terms of mean kinetic energy, which seems to suggest the two pressurized AIs to belong to distinct megabasins.
A corroborating piece of information - concerning the transition from the proton ground state to the first excited ones - is provided by INS measurements, as well as the Raman characterization mentioned at the beginning of this paragraph.
Once again the can geometry selected for scans at MARI spectrometer was flat, but orientated at an angle of 45° with respect to the neutron beam in order to minimize multiple scattering, whose contribution to the vibrational spectra actually proved negligible. Conversely, the contribution from the can was subtracted by automated software routines.
The spectra were recorded at an incident energy $E_0 = 600$ meV, so to minimize the momentum transfer at small scattering angles, and consequently reduce the effect of the Debye-Waller factor and multiphonon scattering.
Within the harmonic framework formalized in [47]

$$< E_k >_x = 2S_{lib}\frac{\hbar\omega_{lib}}{4}coth\left(\frac{\hbar\omega_{lib}}{2K_BT}\right) + S_{tra}\frac{1}{2}K_BT \tag{7.1}$$

$$< E_k >_y = S_{lib}\frac{\hbar\omega_{lib}}{4}coth\left(\frac{\hbar\omega_{lib}}{2K_BT}\right) + S_{ben}\frac{\hbar\omega_{ben}}{4}coth\left(\frac{\hbar\omega_{ben}}{2K_BT}\right) + S_{tra}\frac{1}{2}K_BT \tag{7.2}$$

$$< E_k >_z = 2S_{str}\frac{\hbar\omega_{str}}{4}coth\left(\frac{\hbar\omega_{str}}{2K_BT}\right) + S_{tra}\frac{1}{2}K_BT \tag{7.3}$$

with the S parameter representing the mean kinetic energy fraction uptake of the ^{1}H nucleus for each vibrational mode.
Here $S_{str} = 0.472$, $S_{ben} = 0.463$, and $S_{lib} = 0.056$, which are typical values for ice [166]. On the other hand, $S_{tra} = \frac{M_H}{M_{H_2O}}$.

[6] We are intentionally neglecting network modes since they seemingly affect principal frequencies only slightly, as mentioned in [149], with an estimated contribution of $\leq 6\%$ for polycrystalline ice.

[7] Even though this is not true in general: for example, if ice I_h and liquid water at the same temperature are taken into account, one finds that $E_{str}^{ice} < E_{str}^{liq}$ (due to the stronger HB network in ice), but $< E_k >^{ice} > < E_k >^{liq}$ [165].

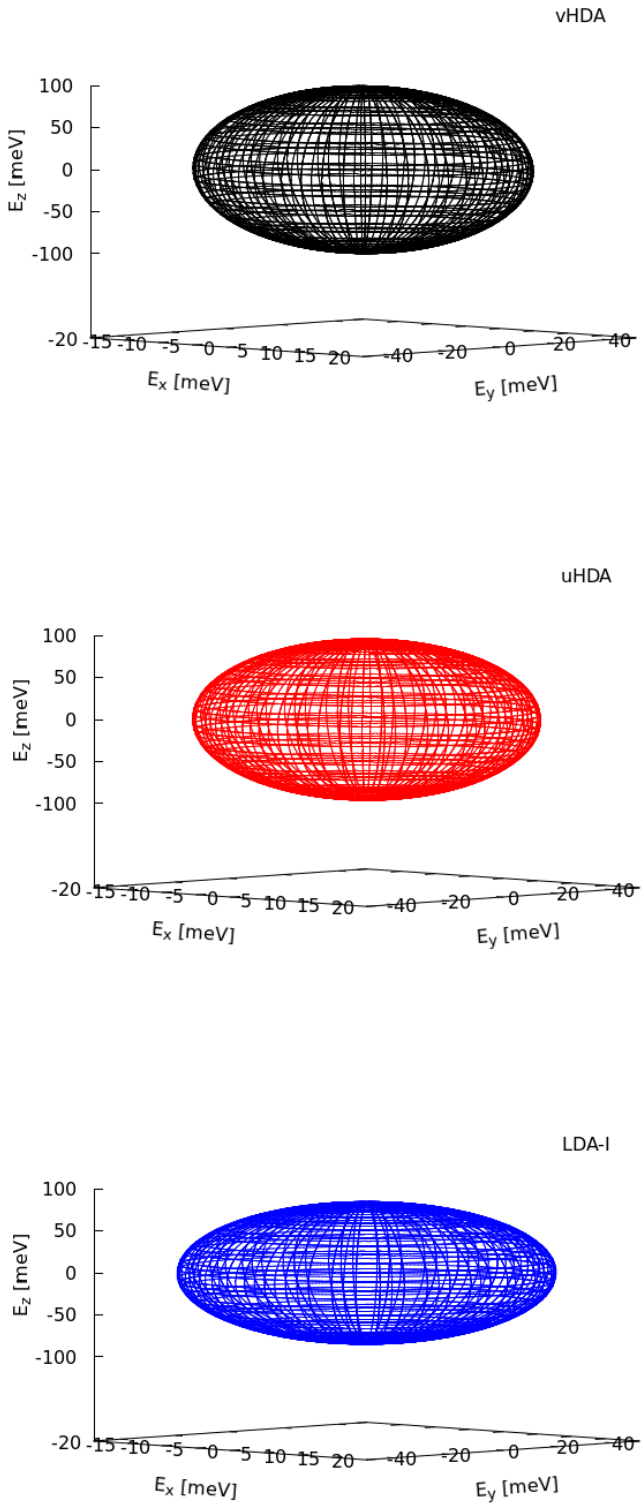

Figure 7.6: Graphical representation of anisotropy for the 3 AIs by an ellipsoid with semiaxes fixed at E_x, E_y and E_z as retrieved from the the multivariate Gaussian fit described in the text. This kind of plot is equivalent to a 3D density plot of an isotropic multinormal distribution (with sigmas replaced by energies) where the fourth dimension is given in color density. Generated via Gnuplot 4.6.

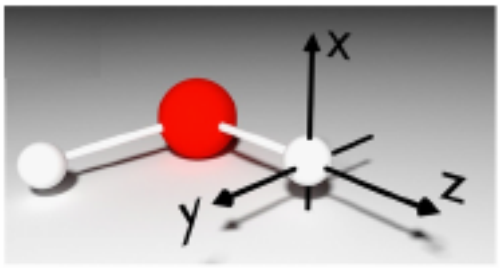

Figure 7.7: Schematic view of the local principal axes associated with hydrogen in the water molecule. Reproduced from [1] with modifications.

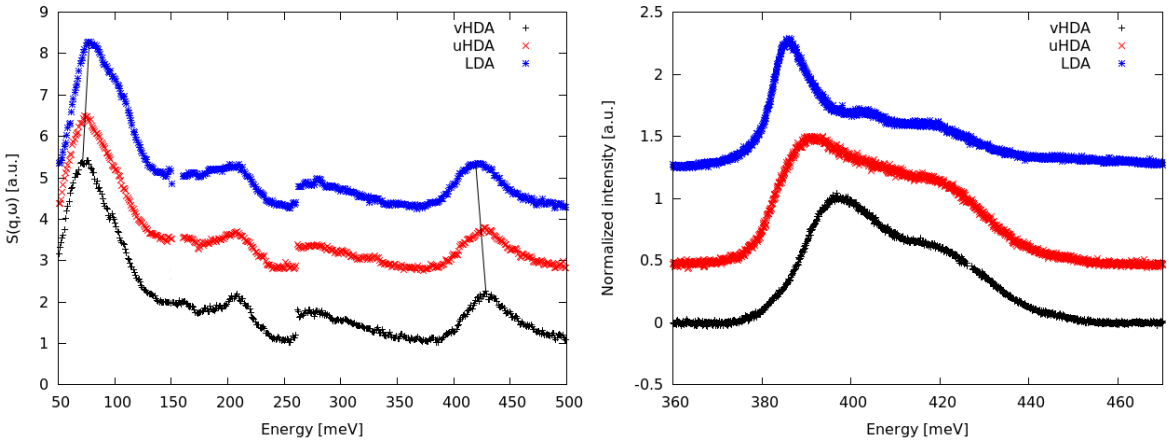

Figure 7.8: Left: Experimental dynamic structure factor of LDA-I (blue), uHDA (red) and vHDA (black) at 80 K. Trend lines superimposed to libration- and stretching maxima are a guide for the eye. Breaks due to integration over different Q-ranges according to the spanned energy region. Right: Raman spectra of the same samples in the coupled ν(O-H) stretching region. Generated via Gnuplot 4.6.

In particular, as to translational modes, notice that the main translational band in ice is typically centered at around $\hbar\omega_{tra} = 7$ meV [167], while at 80 K the translational kinetic energy of a harmonic oscillator is $\frac{\hbar\omega_{tra}}{4} coth\left(\frac{\hbar\omega_{tra}}{2k_BT}\right) = 3.7$ meV. But this latter value is $\sim \frac{1}{2}k_BT = 3.5$ meV, thus the classical approximation proves reasonable.
INS vibrational spectra for the AI triplet are shown[8] in Fig. 7.8a. Fig. 7.8b reports corresponding Raman scans instead.
Unlike INS, which returns the hydrogen-projected density of vibrational states, Raman intensity is associated with a change in polarizability of a specific vibration. For ice, in particular, this means that the in-phase coupled symmetric-stretching vibration of H_2O is the strongest intensity contribution to the spectrum in the O-H region.

[8] The spectra show three different regions (librations, bending and stretching, in ascending order of energy), each obtained via integration over a suitable Q-range ($3.5 - 11.0$ Å^{-1}, $6.0 - 13.2$ Å^{-1}, $9.0 - 15.5$ Å^{-1}, respectively) as a function of the available (Q, ω)-space (see Fig. 7.9 for an example concerning vHDA) in order to maximize the $\frac{signal}{noise}$ ratio.

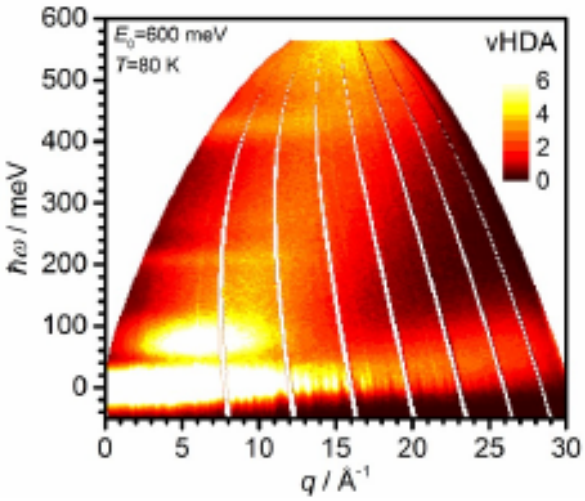

Figure 7.9: Contour plots of the scattering intensity as a function of energy and momentum transfers for vHDA at 80 K and incident energy of 600 meV. Reproduced from [1] (supporting info).

In both INS and Raman data the notable trends are the blue-shifts of the O-H stretching bands and the red-shift of the libration band as density increases. The former are a mark of stronger covalent O-H bonds due to weakening of hydrogen bonds, which is fully consistent with info retrieved from DINS, as well as, in general, with analogous trends observed for the crystalline phases of ice at liquid-nitrogen temperature and ambient pressure [168], or 'normal' water, or supercooled water [169]. Such weakening is equally responsible for the red shift of the librational modes, which are caused by the hindered rotations of water molecules becoming less hindered with respect to their local HB-network.
So far the qualitative picture of the local ^{1}H-dynamics of AIs. But quantitatively speaking?
At a better look (Fig. 7.10), the increase in stretching energy (and $< E_k >$) with density as derived from DINS is much steeper, if compared to the corresponding INS values. Indeed, unlike INS, DINS is able to fully capture the strengthening of covalent bonds in the ground state, as already highlighted by the slope-change visible in the wings of the $n(p)$-lineshapes.
As seen above, the directional energies derived from INS were obtained within a harmonic model of an isolated molecule, under the assumption of decoupling of both inter- and intramolecular modes [47]. Within this framework, local hydrogen dynamics shows poor density/structure dependence. Thus, what Fig. 7.10 suggests us is that DINS has a chance to catch *anharmonicities* through the effective ω_α-frequencies.
From this point of view, a modest degree of anharmonicity is taken to task for libration modes.
As to bending, INS allows for a direct measurement of the related energy, but the coupling of internal modes affects the DINS-derived value as the surrounding network evolves from LDA to vHDA. That's what is likely to cause the observed differences in Fig. 7.10.

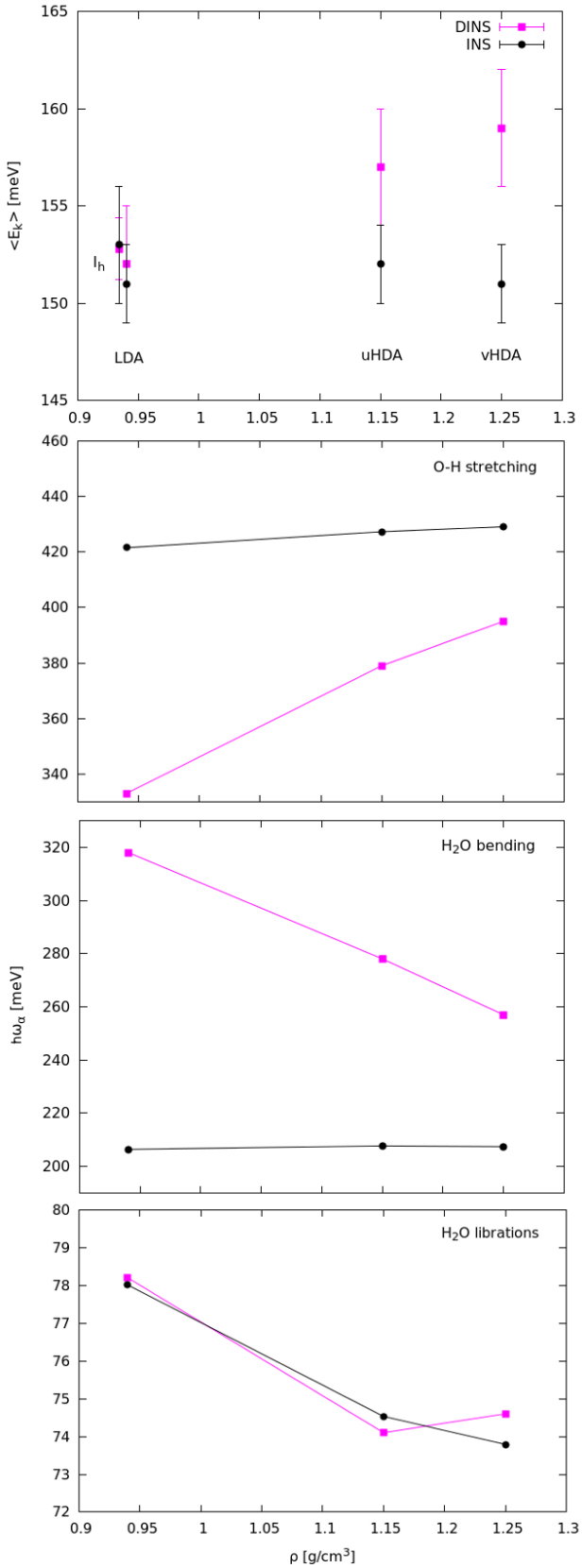

Figure 7.10: Top: $< E_k >$-values for I_h and the AIs; and Bottom: normal-mode energies for the AIs as retrieved from DINS (purple) and INS (black). Trend lines are a guide for the eye. Generated via Gnuplot 4.6.

Speaking in terms of potential, the lower values of $< E_k >$ and $< E_k >_z$ in LDA - compared to uHDA and vHDA - flag a more anharmonic and shallower hydrogen potential-energy surface, since it is the dynamics along the z-direction to capture most the shape of the effective ^{1}H-nucleus potential along the O-H bond direction. Indeed, as the hydrogen bonding weakens with increasing density, the curvature of the effective potential increases and its shape becomes similar to the shapes inferred from INS within the harmonic assumption. Hydrogen bonding can therefore be viewed as the main cause for anharmonicity in AIs. This is strongly coherent with both computational studies addressing the nature of anharmonicity in small water clusters via second-order vibrational perturbation theory [170] and very recent experimental probing of nuclear quantum effects of the hydrogen bond via tip-enhanced inelastic electron tunneling spectroscopy based on a scanning tunneling microscope [56].
Does a way exist of quantifying the degree of anharmonicity of the O-H stretching modes by a combined use of DINS and INS data?
The absolute energy of the first vibrationally excited state can be calculated as the sum of the ground-state energy from DINS plus the experimental excitation energy from INS. This should equal the energy of the first excited state within a harmonic model, suitably corrected by a term containing an anharmonicity constant:

$$\frac{\hbar\omega_{str}^{DINS}}{2} + \hbar\omega_{str}^{INS} = \frac{3}{2}\hbar\omega_{str}^{INS}\left(1 - \frac{3}{2}\chi_{anh}\right). \tag{7.4}$$

This way, χ_{anh} values of 0.046 (LDA), 0.025 (uHDA), and 0.018 (vHDA) are obtained.

7.2 SCW

The scope of this experiment was the DINS assessment of proton quantum dynamics in supercritical water across the Widom line(s) along an isobar close to the liquid-gas critical point. Supporting information came from earlier INS measurements on SCW taken at SEQUOIA (ToF chopper instrument), which is located at SNS spallation source, ORNL, Oak Ridge, U.S.A.
At VESUVIO spectrometer a sample of bulk distilled water was brought to the operating pressure of 25 MPa and scanned across three different temperatures: 553 K (subcritical), 663 K (supercritical), and 733 K (supercritical), corresponding to densities of 0.777, 0.215 and 0.104 $\frac{g}{cm^3}$, respectively (Fig. 7.11).
Due to the strongly oxidating power of SCW, particular attention was paid to the design of the can in order to avoid fluid leaks: precisely, a Ti slab of size 50.00 × 50.00×2.03 mm^3 was employed, enclosing 38 cylindrical holes with diameter (0.990± 0.025) mm. The can was wrapped in a 0.11-mm thick aluminum foil at 733 K in order to prevent any thermal dispersion (Fig. 7.12). The orientation was orthogonal to the neutron beam.
The total integrated proton current amounted to 450 μAh at 553 K, 15570 μAh at 663 K, and 14630 μAh at 733 K.
No empty-can runs available.

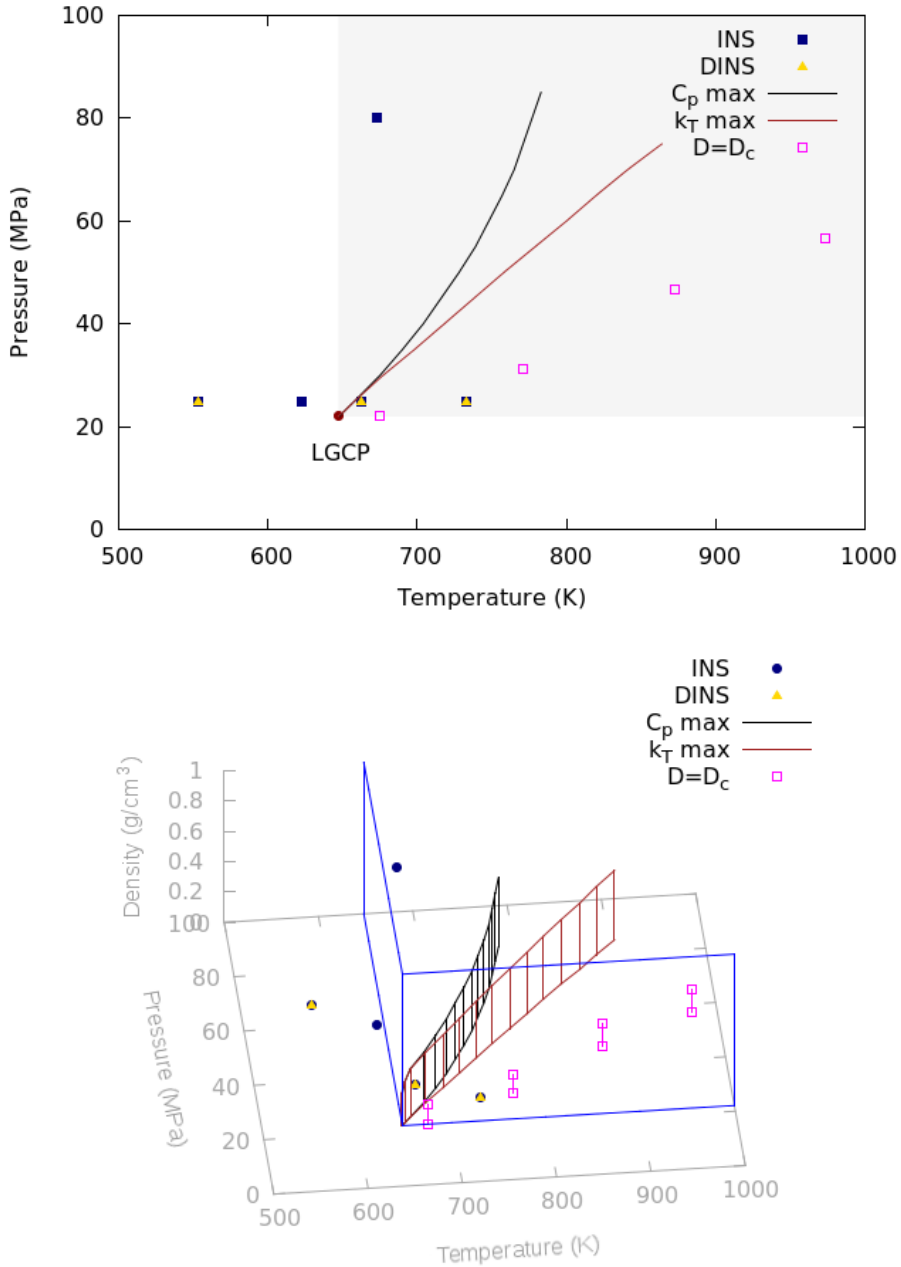

Figure 7.11: Top: A 2D thermodynamic representation of the set of DINS measuments at VESUVIO (yellow points) and earlier INS determinations at SEQUOIA (blue points) with respect to a couple Widom lines emanating from the liquid-gas critical point and the Frenkel line. The locus of C_p maxima (black curve) was reconstructed out of NIST data (http://webbook.nist.gov/chemistry/fluid/), and that of k_T maxima (brown curve) out of ThermoC data (http://thermoc.uni-koeln.de/thermoc/), both via IAPWS-95 formulation [115]. The locus of constant self-diffusion coefficient (approximated Frenkel line, purple points) was reconstructed out of experimental NMR data [171]. The grey box delimits the SC region and is intended as a guide for the eye. Bottom: Same data in a 3D fashion, in order to appreciate variations of density between different points. Generated via Gnuplot 4.6.

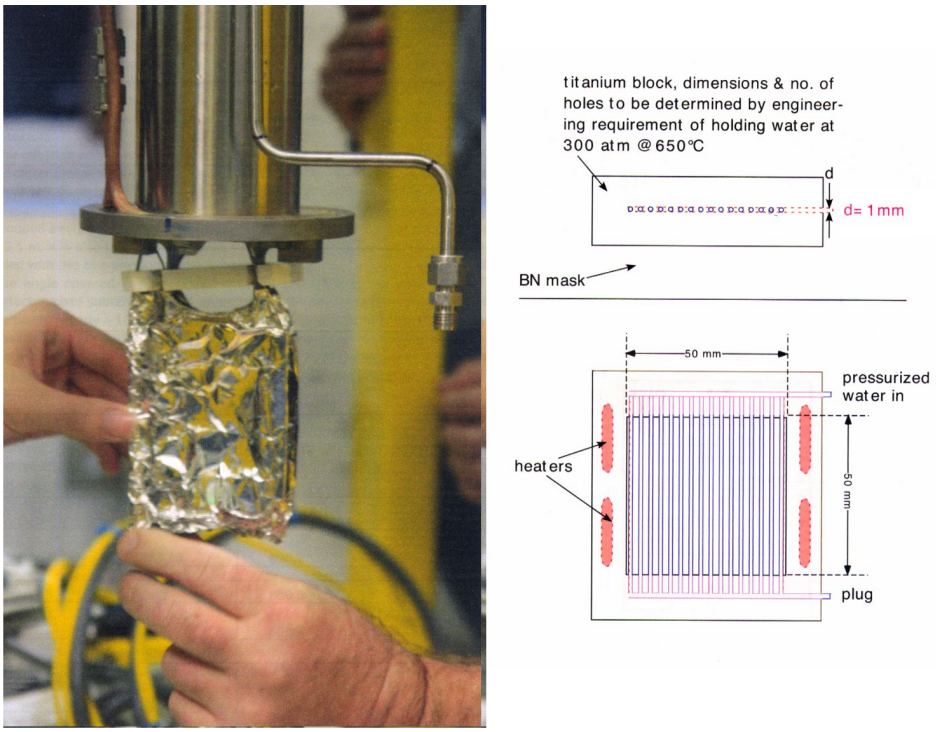

Figure 7.12: Left: The titanium can (wrapped in aluminum) used for DINS measurements on SCW. Right: Can scheme.

The procedure of data reduction basically followed the same path described in the AI case. A notable difference was just a non-negligible contribution from Al at 733 K to take into account during the multi-Voigt fit of ToF spectra.
The final $\overline{F}(y)$ curves at 553, 663, and 733 K are shown in Fig. 7.13.
Though water still retaining a weak, short-ranged structure at the pressure and temperatures investigated - including dimers and even trimers in the medium-density range[9] where the two supercritical determinations are placed [108,109] - the substantial disruption of the tetrahedrally coordinated H-bond network in the SC region calls for actual decoupling of translational, librational and vibrational degrees of freedom under the validity of the harmonic approximation, as verified by earlier DINS experiments on similar systems [172]. Therefore, a multivariate Gaussian fit of the experimental $F_n(q,y) = [J(y) + \Delta J_n(q,y)] \otimes R_n(q,y)$ hystograms was performed, harmonically modeling the lowest order of the FSEs[10]. Fit results are presented in Table 7.2 and Fig. 7.13.
What appears evident here is the large amount of noise[11] especially affecting the highest-T NCP[12], which strongly impacts the uncertainty associated to the mean

[9]Indeed, SC water is usually said low-density when $\rho < 0.1\ \frac{g}{cm^3}$, with the appearance, in vibrational spectra, of a roto-vibronic structure under $0.01\ \frac{g}{cm^3}$, which signals the transition to the monomeric form of the substance under these extreme conditions [108].

[10]A second fit was performed releasing the harmonic constraint on FSEs. Its results turned out consistent with those of the constrained case.

[11]This also caused the calculation of the momentum distributions from the NCPs to be basically unuseful. $n(\mathbf{p})$-noise was so large to prevent any telling comparison between distribution pairs.

[12] In spite of the large number of experimental runs performed at 733 K, the low number of

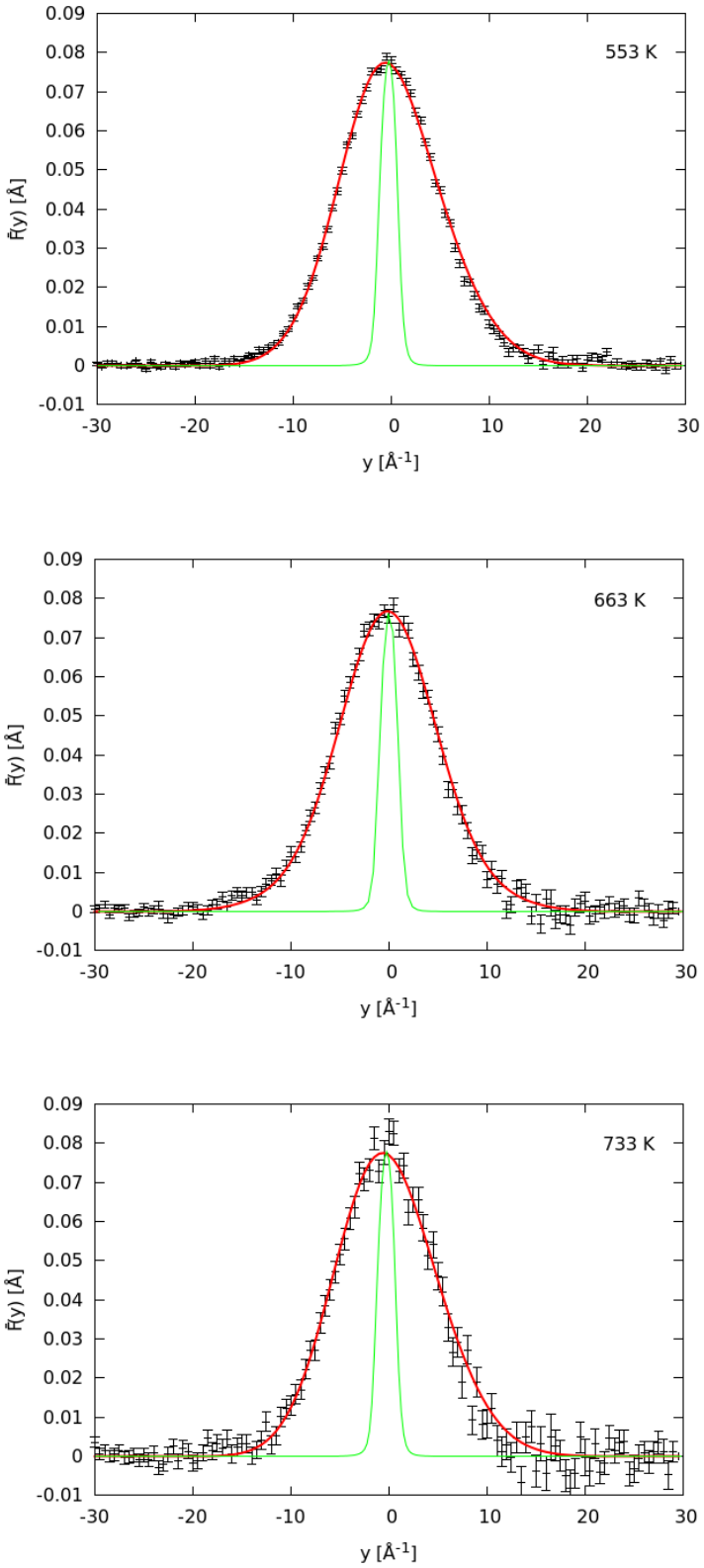

Figure 7.13: Experimental NCP (black) + multivariate-Gaussian fit (red) + (rescaled) simulated resolution curve (green) at 553, 663, and 733 K. Generated via Gnuplot 4.6.

Table 7.2: Results from the multivariate Gaussian fit for SC water at 553, 663, and 733 K.

	553 K	663 K	733 K
σ_x [Å^{-1}]	3.70±0.09	3.74±0.16	4.24±0.47
σ_y [Å^{-1}]	5.87±0.18	6.07±0.30	5.66±0.56
σ_z [Å^{-1}]	5.87±0.15	6.07±0.29	5.66±0.42
$\overline{\sigma}$ [Å^{-1}]	5.24±0.02	5.41±0.05	5.23±0.09
$< E_k >$ [meV]	171.08±1.57	182.01±3.70	170.29±5.92

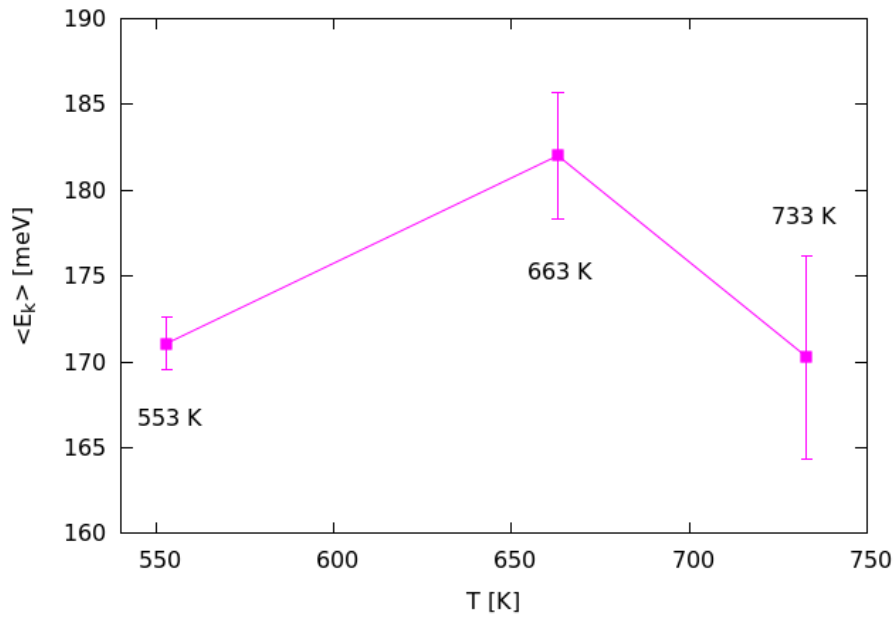

Figure 7.14: $< E_k >$-values for SCW at the three temperatures investigated as retrieved from the multivariate Gaussian fits of related NCPs. Trend lines are a guide for the eye. Generated via Gnuplot 4.6.

kinetic energy (Fig. 7.14).
Another annoying point is the apparent degeneracy of σ_y and σ_z even at the lowest temperature, which gives no chance to put forward any hypothesis on directional energies as seen from the point of view of DINS with respect to INS. The only value to take advantage of is the average $< E_k >$.
That said, an interesting issue emerges anyway, which can be discussed here.
Irrespective of errorbars, the energy trend reported in Fig. 7.14 looks peculiar. While the $< E_k >$-value at 533 K is pretty consistent with various close subcritical DINS determinations reported in [45], one would conversely expect a larger proton mean kinetic energy at 733 K than 663 K, due to the progressive disappearance of oligomers and intermolecular coordination at increasing T, which should favor

scatterers at $\rho \sim 0.1 \frac{g}{cm^3}$ unavoidably produced a low $\frac{signal}{noise}$ ratio.

Table 7.3: Vibrational frequencies of SCW as taken from SEQUOIA data (stretching and bending), experiments by Ricci et al. (stretching) [173] and simulations from Skarmoutsos et al. (librations) [174].

	SUB	SUB	SUPER	SUPER	SUPER
Temperature [K]	553	623	673	663	733
Pressure [MPa]	25	25	80	25	25
Density $[\frac{g}{cm^3}]$	0.777	0.625	0.660	0.215	0.104
ω_{str} [meV]	450.00	454.00	457.50	466.00	472.00
ω_{ben} [meV]	200.00	200.00	200.00	200.00	200.00
ω_{lib} [meV]	39.24	35.36	36.24	27.51	25.93

Table 7.4: Directional energies and $< E_k >$ as deduced from the harmonic decoupled model described in Eqs. 7.1-7.3 for the liquid case.

	SUB	SUB	SUPER	SUPER	SUPER
Temperature [K]	553	623	673	663	733
Pressure [MPa]	25	25	80	25	25
Density $[\frac{g}{cm^3}]$	0.777	0.625	0.660	0.215	0.104
$< E_k >_x$ [meV]	25.20	27.92	30.06	29.23	32.17
$< E_k >_y$ [meV]	37.12	39.00	40.54	40.00	42.15
$< E_k >_z$ [meV]	104.62	105.74	106.70	108.59	110.19
$< E_k >$ [meV]	166.94	172.66	177.30	177.82	184.44

intramolecular (vibrational) motion [42].
Indeed, if one takes ω_{str} and ω_{ben} as derived from either the above-mentioned INS spectra at SEQUOIA or other INS experiments [173], as well as ω_{lib} from simulated VACFs retrievable in the literature [174] as a function of bulk density[13], and puts all these values into the harmonic model described in Eqs. 7.1-7.3, he eventually finds the results enclosed in Tables 7.3 and 7.4, being

$$< E_k >= \frac{3\hbar^2}{2M}\overline{\sigma}^2 = \frac{\hbar^2}{2M}(\sigma_x^2 + \sigma_y^2 + \sigma_z^2) =< E_k >_x + < E_k >_y + < E_k >_z, \quad (7.5)$$

and once chosen $S_{str} = 0.459$, $S_{ben} = 0.463$, $S_{lib} = 0.475$ (values for the liquid state[14] [166]).
That is, the model returns a monotonically increasing set of energies (reasonably in the same range as experimental DINS data) when going from the subcritical region through the supercritical one as density decreases, which is in line with the monotonic increase of stretching energies in row 1 of Table 7.3.
Unfortunately, the trick of repeating the fit on the highest-T point after fixing directional energies at the values set in Table 7.4, in order to assess whether the

[13]Librations in SEQUOIA data were not accessible due to large noise and convolution to resolution.

[14] Remember that the density of the three SCW determinations is medium-range and notice that no experimental point goes significantly beyond the Frenkel line (Fig. 7.11).

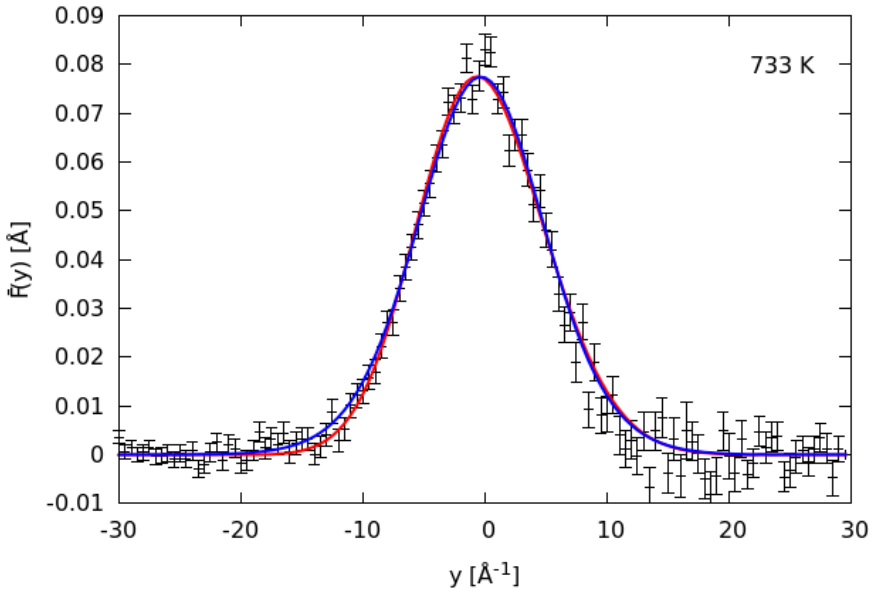

Figure 7.15: Experimental NCP (black) + multivariate-Gaussian fit (red) + constrained (Table 7.4) multivariate Gaussian fit (blue) at 733 K. Generated via Gnuplot 4.6.

resulting curve is better adapted to datapoints, returned no discriminatory criterion, since both fit curves comfortably surf experimental errors (Fig. 7.15).
Just a matter of noisy DINS measurements, then? Could not be the case, at least in part.
Looking at Fig. 7.11, one can observe how close to both the CP and Widom lines the experimental point at 663 K and 25 MPa is. To be precise, the point exactly falls into the scaling region extending circa 30 K and 90 bar above the LGCP, which is the one where all Widom lines merge with one another and density fluctuations become significant [113].
This suggests that the sudden 'jump' in $< E_k >$ associated to the mid DINS determination could be the result of a strong density fluctuation, accompanied by an occasional transition to a ballistic collisional type of motion (typical of gases) as already experimentally observed by inelastic X scattering [175, 176]. Which, associated to the large noise that afflicts the energy value at 733 K, could account for the unexpected trend of Fig. 7.14.
Nice eventuality, which would open the door to the exploitation of DINS as a probe of anomalies of criticality[15].

[15]To my knowledge, no formal link between the proton mean kinetic energy $< E_k >$ and the thermodynamic correlation length ξ of critical-phenomenon theory can be found in the literature.

Yet, an interesting article by Walrafen exists [177], which - by a vast series of Raman experiments on water from the amorphous region up to the dense-SC-steam zone - highlights a linearity between proton spatial correlation, modeled as the ratio between the intensities of the two Raman O-H stretching components (the correlated component, corresponding to in-phase stretching motion of a hydrogen-bonded aggregate ('patch') consisting of a central H_2O molecule and its nearest and

7.3 The PMF

Let us consider zirconium hydride[16] ZrH_2.
Due to hydrogen being bound in a nearly equilateral tetrahedron of Zr atoms, this metal hydride is a typical example of isotropy, with cross-sections for scattering from the first excited level varying with scattering angle as predicted for a harmonic oscillator, and cross-section for purely elastic scattering by hydrogen atoms varying linearly with momentum transfer (as required for harmonic motion) at least at smaller Q-values [179]. Thus, ZrH_2 is a promising candidate to test the linearity of the MF in the isotropic univariate Gaussian case.
An old 2009 calibration experiment on ZrH_2 (in an aluminum can) at 290 K was recovered from the ISIS database; raw ToF data were γ- and MS-corrected an analogous way as described in the AI case. Then, a multi-Voigtian profile (+ residual background) was fitted to the reduced ToF outputs, and fitted lines for Al, Zr and background were subtracted from the overall spectra in order to recover ^{1}H signals only. Subsequently, hydrogen ToF spectra were transformed to the y-domain. The resulting average $\overline{F}$-curve is given in Fig. 7.16, together with the average of fixed-angle isotropic[17] Gauss-Hermite best fits[18], which returned a σ of about 4.2 $Å^{-1}$ (in line with [180, 181]).
The overall NCP was then corrected for FSEs by direct subtraction, and then 'symmetrized' (Fig. 7.17), in the sense that a positive semi-curve was obtained making an average over symmetric points aside the peak[19]. The associated MF was numerically computed over such a semi-curve according to Eq. 6.22, and then compared to the exact linear curve described in Eq. 6.25, as reported in Fig. 7.18.
This latter figure shows how the numerical procedure returns very reliable estimates of the MF for $x_\parallel$ less than about 0.35 Å or so, before uncertainties explode due to both computation errors and finite-range approximations[20]. Another source of error

higher neighbors, and the uncorrelated one, for which the phase relationships are lost), and a structural correlation length (SCL) as recovered from the high-distance tail of the last significant peak in the radial distribution function, where $g(r) = 1$.

This linearity arises because the proton motions are correlated over hydrogen-bonded distances determined by the SCL, which also limits the transverse acoustic phonon wavelength (shear mode).

[16]Studies of the constitution of the Zr-H system have identified three zirconium hydride phases - γ, δ, and ϵ, respectively - which differ in their crystallography and hydrogen composition. These phases have nominal stoichiometric compositions ZrH, $ZrH_{1.5}$, and ZrH_2, respectively. However, it looks like the γ-phase alone is truly stoichiometric, while the other two hydrides can exist over a range of hydrogen compositions [178]. The ϵ-phase (the one taken into account in the present experiment) is characterized by a centered tetragonal lattice.

[17]The isotropic hypothesis was corroborated by a 3D multivariate Gaussian fit, which returned three coincident directional sigmas within errors.

[18]The fits were performed with the FSE parameter either harmonically fixed or free to vary. These two approaches produced coincident sigmas (within the experimental errors) and null non-Gaussian coefficients (within their own uncertainties again), returning two nearly perfectly superimposed curves.

[19]In order to produce a smoother curve, more suitable to be numerically integrated.

[20] Indeed, this latter issue is subtler than expected. As $x_\parallel$ goes bigger and bigger, the number of oscillations included in the profile of each integrand in the integral ratio shown in Eq. 6.22 increases rapidly. This means that the amount of area subtended by any integrand curve (which has a Gaussian envelope) over the finite range between 0 and 30 $Å^{-1}$ (which is the experimental

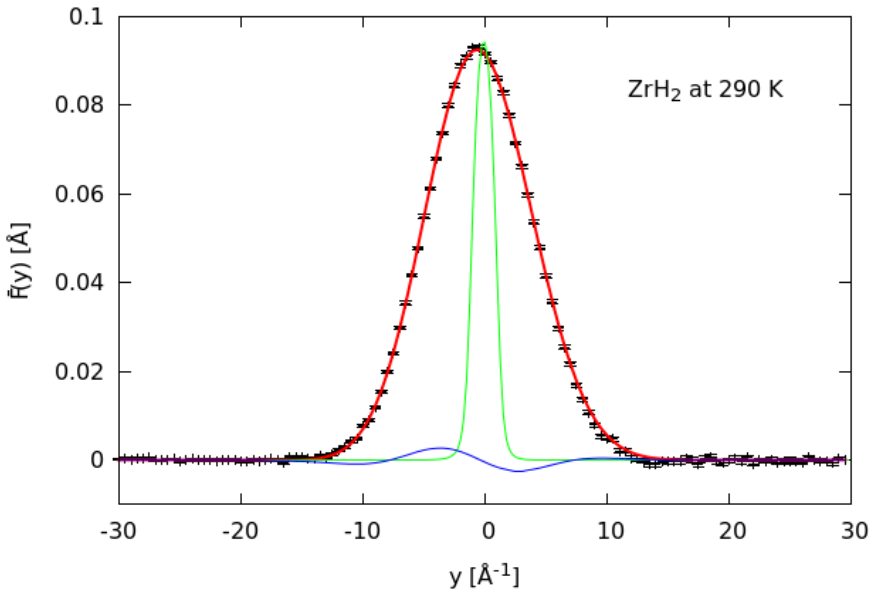

Figure 7.16: Experimental NCP (black) + isotropic Gauss-Hermite fit (red) + FSE contribution (blue) + rescaled VESUVIO resolution curve (green) for ZrH_2 at 290 K. Generated via Gnuplot 4.6.

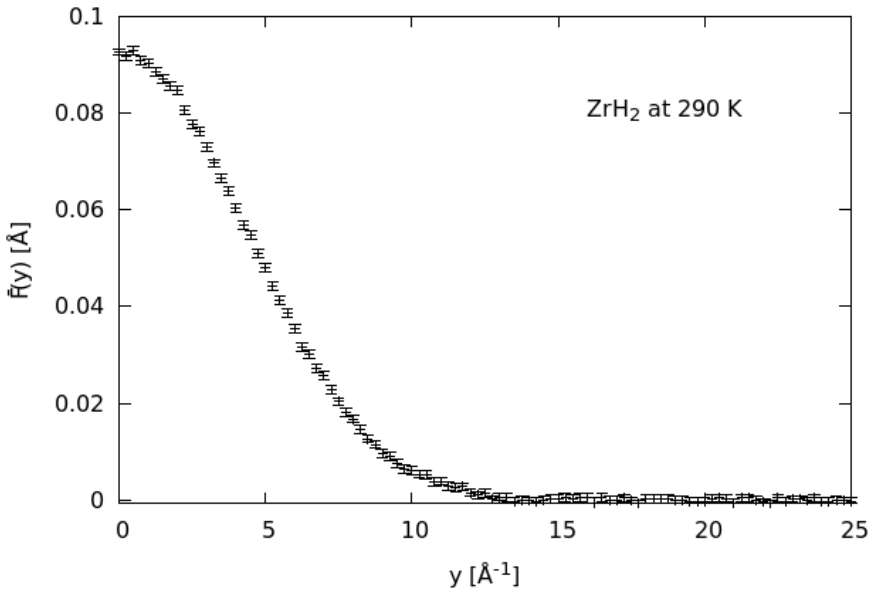

Figure 7.17: FSE-corrected and symmetrized NCP for ZrH_2 at 290 K. Generated via Gnuplot 4.6.

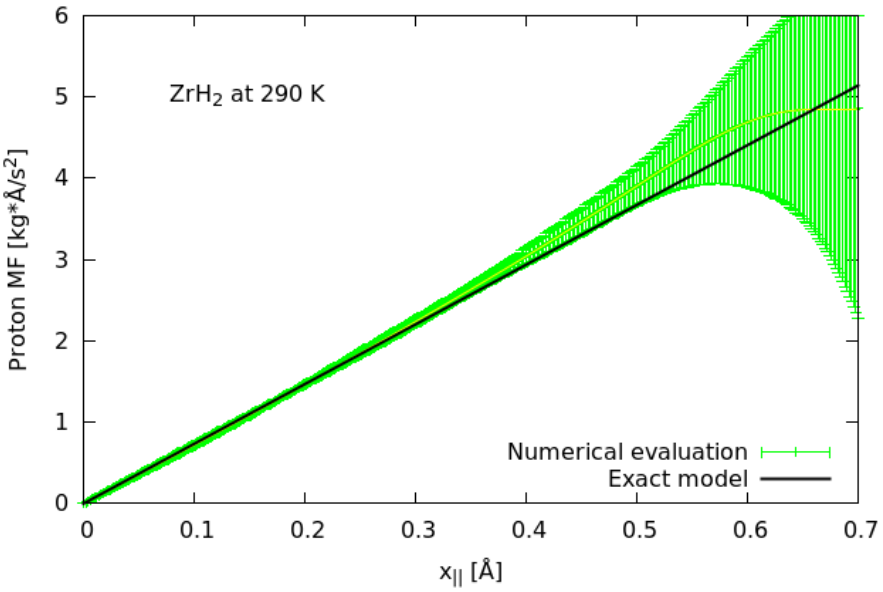

Figure 7.18: Proton MF along $\hat{\mathbf{Q}}$ for ZrH_2 at 290 K from numerical evaluation (green) and exact linear model (black). Generated via Gnuplot 4.6.

is the convoluted resolution, which nevertheless should represent no serious issue, being its contribution to the variance of the experimental signal not larger than 3% [134].
That said, the range $[0 \div 0.3]$ Å was chosen as the 'safe' one to make comparisons with MFs that can be computed only numerically.
A first test was performed with a set of FSE-corrected and symmetrized NCPs of crystalline ice I_h from earlier DINS experiments, taken at 5, 71, and 271 K, respectively (with estimated average sigmas of about 4.85, 4.87, and 4.99 $Å^{-1}$, respectively). As one can see in Fig. 7.19, at the two lowest temperatures each associated proton MF projected along the direction of the momentum transfer proves linear within the experimental uncertainties (which are small) if compared to the exact linear model recovered from a univariate Gaussian with $\sigma = \overline{\sigma}_{I_h}$. Conversely, a clear sign of anharmonicity appears at 271 K.
This is coherent with a picture of I_h as a quasi-harmonic system with a small amount of anisotropy that stems from the molecular orientations in the crystal[21] (Fig. 7.20) [149], and a general anharmonic behavior that emerges at high temperature.

window for non-negative y-variables) is a poorer and poorer approximation of the exact integral calculated between the origin and infinity. In other words, beyond a certain number of oscillations the cut of the asymptotic 'tails' of the oscillating Gaussian sweeps a dominant part of the integral up.

[21] Water molecules embedded into any crystalline ice are fully H-bonded, which results in a 4-fold molecular coordination. Bonding conditions are established by the Bernal-Fowler ice rules, which state that (1) one and only one hydrogen atom is found along each of the H-bonds; and that (2) two hydrogen atoms are always covalently bonded to each of the oxygen atoms, which preserves the stoichiometry of the compound [99].

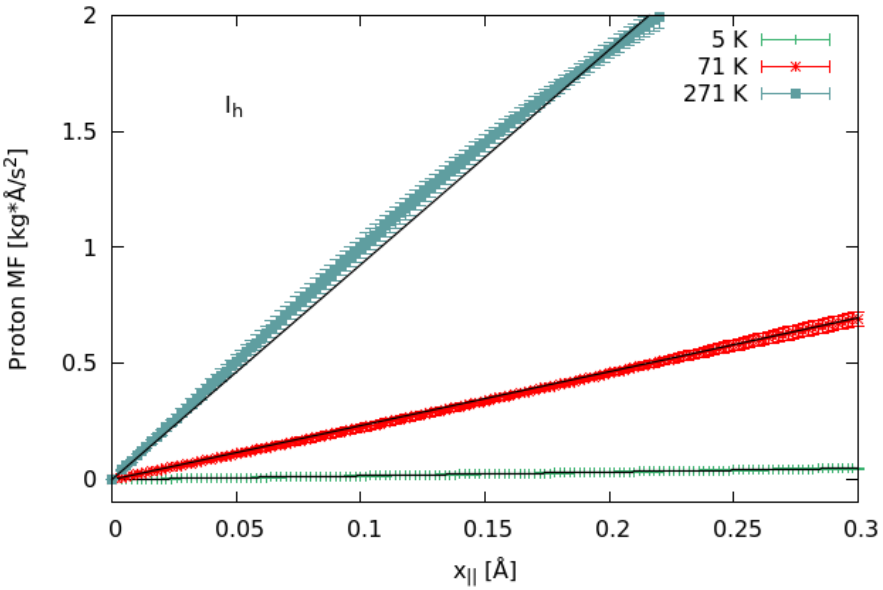

Figure 7.19: Proton MF along $\hat{\mathbf{Q}}$ for I_h at 5, 71, and 271 K, respectively, from numerical evaluation (color) and exact linear model as extracted from a hypothetical 1D Gaussian with $\sigma = \overline{\sigma}_{I_h}$ (black). Generated via Gnuplot 4.6.

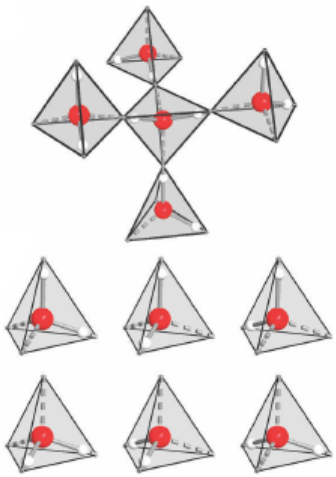

Figure 7.20: Top: A pentameric fragment of I_h. Covalent bonds are indicated by solid lines and hydrogen bonds by broken lines, respectively. Bottom: The six possible orientations of a water molecule in ice. Reproduced from [99].

Let's turn to the AIs. In spite of larger errors than the ones affecting the NCPs of the crystalline sample, MFs reported in Fig. 7.21 show a more and more anharmonic behavior as density decreases, which mirrors what was found by DINS as described in paragraph 7.1.
Supercritical water at last. NCP errors are large here, especially at the two highest temperatures, yet Figs. 7.22 and 7.23 seem to suggest that the transition from the subcritical to supercritical domain is accompanied by an apparent 'isotropic harmonization' of the proton potential, probably as a consequence of the progressive rupture of the H-bond network and gain of similarity with the monomeric form of the substance [45].
Notice how the strong curvature of the MF in ice, as well as its linearization in the supercritical region, is suggestive of a non-negligible influence of anharmonicity in H-bonding, which possibly turns out as the next stage of evolution of the mathematical gear described in [159], and further developed in paragraph 6.3. This way the tool could be stably adopted in order to refine curve fits to NCP points, provided that experimental NCP data are not excessively noisy.

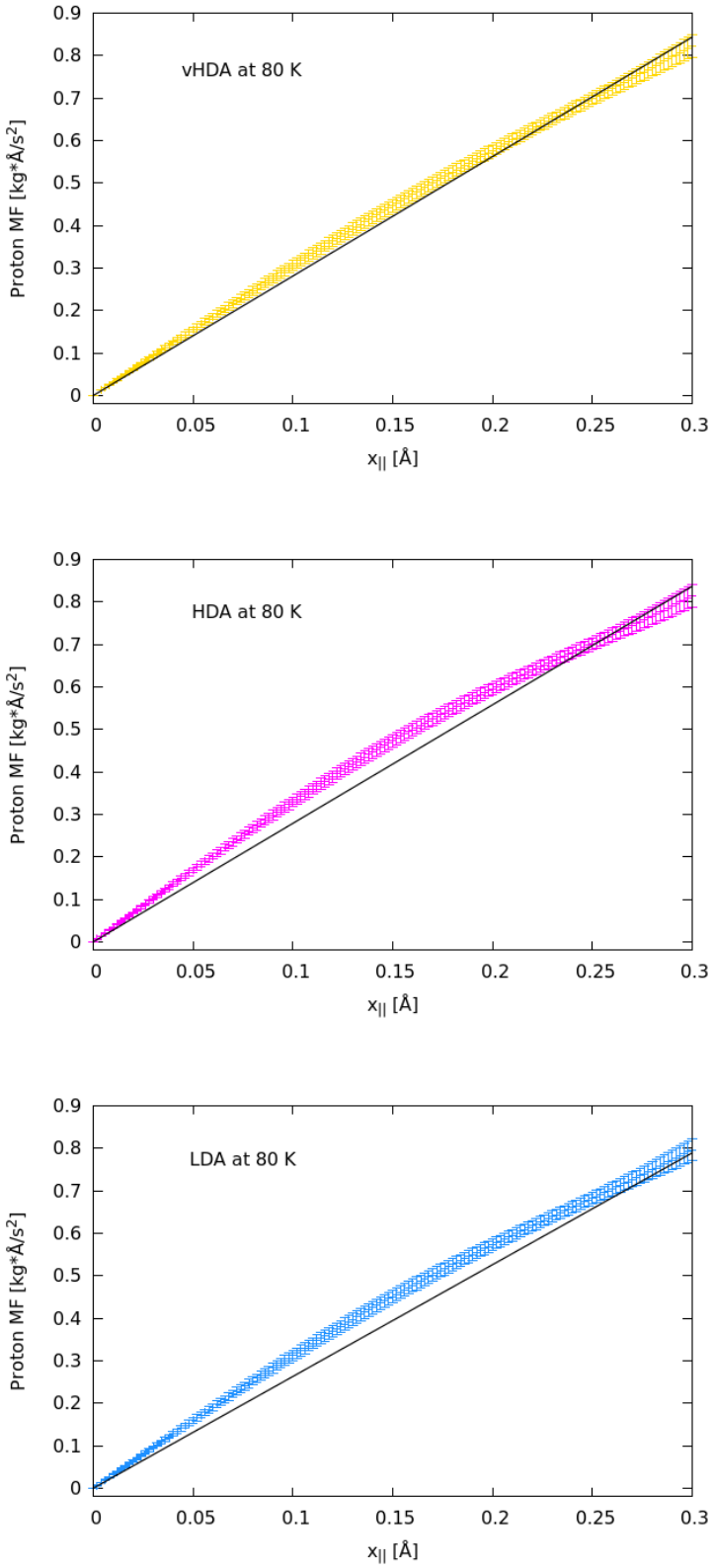

Figure 7.21: Proton MF along $\hat{\mathbf{Q}}$ for vHDA (top), uHDA (center), and LDA-I (bottom), respectively, from numerical evaluation (color) and exact linear model as extracted from a hypothetical 1D Gaussian with $\sigma = \overline{\sigma}_{AI}$ (black). Generated via Gnuplot 4.6.

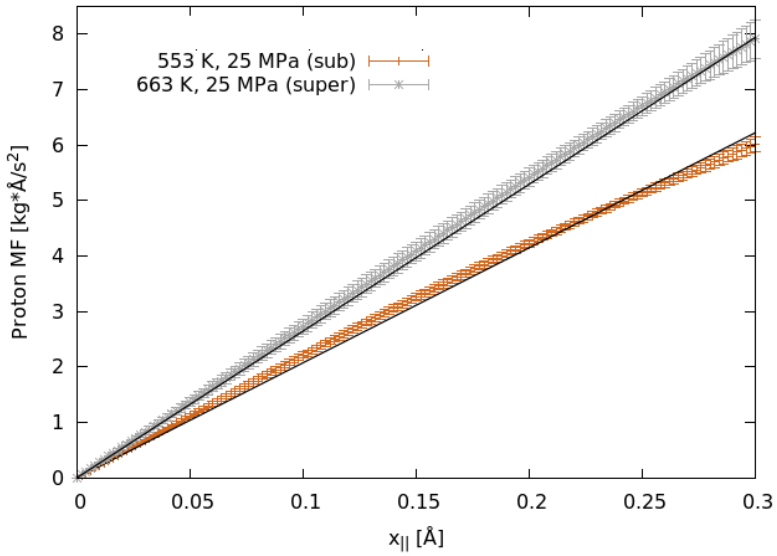

Figure 7.22: Proton MF along $\hat{\mathbf{Q}}$ for subcritical (553 K) and supercritical water (663 K) at 25 MPa, from numerical evaluation (color) and exact linear model as extracted from a hypothetical 1D Gaussian with $\sigma = \overline{\sigma}_{SCW}$ (black). Generated via Gnuplot 4.6.

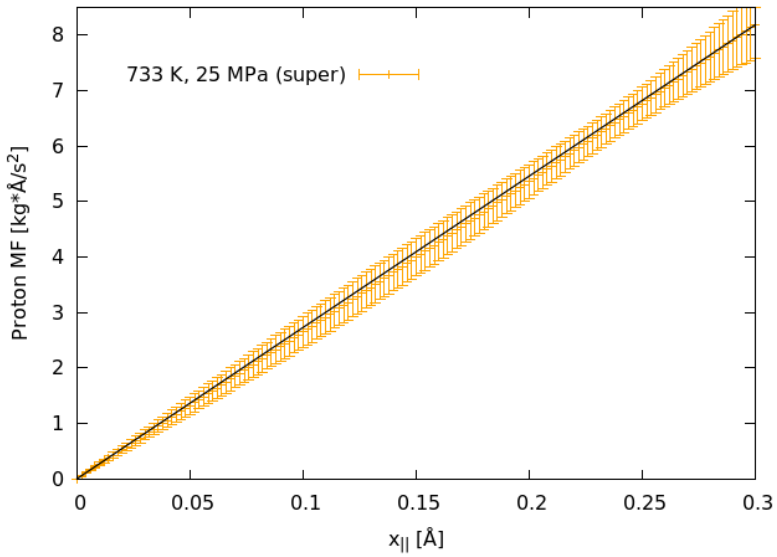

Figure 7.23: Proton MF along $\hat{\mathbf{Q}}$ for supercritical water at 733 K and 25 MPa, from numerical evaluation (color) and exact linear model as extracted from a hypothetical 1D Gaussian with $\sigma = \overline{\sigma}_{SCW}$ (black). This plot is presented separately since its overlapping the determination at 663 K is confusing to the eye. Generated via Gnuplot 4.6.

8

Adding pieces to the neverending puzzle

Camminando non c'è strada per
andare che non sia di camminar

Vinicio Capossela

After more than two centuries of scientific investigation, even now water is largely *terra incognita*. This tiny molecule, with its particularly small moments of inertia and its exceptional ability to establish numerous H-bonds around it, is still able to offer surprises both from a dynamic and a thermodynamic point of view.
Ok, let's take stock of which pieces we've been able to add to the picture.
If one peruses scientific literature, when it comes to elucidating H-bond dynamics, IR spectroscopy remains the prime technique to study water. Yet, infrared spectra often ignore quantum anharmonicity [149]. On the other hand, theories using harmonic or quasi-harmonic descriptions of quantum effects related to zero-point vibrations lead to an overestimation of the atomic and molecular kinetic energies that are greater than those obtained from path integral molecular dynamics simulations [149, 182]. The shortcomings of the harmonic description originate from the stiffer underlying effective potentials than those derived from *ab-initio* methods.
The relevance of anharmonic effects in the quantum dynamics of the hydrogen nuclei in water, as well as their evolution with density, has been highlighted along this entire monograph. In particular, in the case of the AIs, DINS has provided for direct probing of the increase in the kinetic energy along the $O-H$ bond direction, as the curvature of the effective potential increases and becomes more harmonic with increasing density. The subtlety of such anharmonic contributions has been derived by combination and comparison of this technique, which is sensitive to the single-particle hydrogen wave function, with methods that are responsive to vibrational energy differences, such as INS and Raman.
Not to mention the mean-force toolbox, which in its simplicity has proven able to convey a key information to formally shape the scatterer potential, even in those cases when experimental errors affecting the NCP are not so restrained.
Many possible neutron-based extensions of the present work can be envisaged.
As to the AIs, for example, interesting hints could come from the analysis of phonon modes (VDoS from INS).
A point that is quite debated is the possible existence of a boson peak for high-density amorphous ices. Though Tulk et al. [100] called for a glassy nature of HDA in 2002, a more recent quasi-elastic neutron (QENS) study [183] seems to rule out this

possibility for the whole triplet of AIs. Indeed, this topic is particularly intriguing, since a recent experimental work by Chumakov et al. [184] on SiO_2 suggests that the boson peak would be the glassy counterpart of the van Hove singularity[1] of the corresponding crystal, with the *density* of the system, and not disorder, playing a critical role. And we've just seen how density drives modifications in the DINS responses of water amorphs.
More generally, local structures of the AIs could prove much more ordered than expected, and somehow 'borrow' different structural motives from the corresponding crystalline phases depending on density.
As to supercritical water, on the other hand, a massive, systematic INS+DINS investigation (possibly coupled to other approaches, such as SAXS [185]) along the Widom line(s) is needed, with a focus onto the extraction of the VDoS in order to recover the velocity auto-correlation function, which, in turn, will allow for the precise tracking of the dynamic Frenkel line in the phase diagram.
It's still a long ride home, but for sure, with the advent of a new generation of accelerator-based pulsed neutron sources like the European Spallation Source (ESS), exciting opportunities to improve our knowledge of the structure and dynamics of the 'first and foremost medicine[2]' are in sight.

[1] Van Hove singularities in the densities of states (DoSs) of crystals occur at critical points of the Brillouin zone, where the DoS gets not differentiable.

[2] Slovakian proverb.

Bibliography

[1] Parmentier, A., et al (2015). *Evolution of Hydrogen Dynamics in Amorphous Ice with Density*. J. Phys. Chem. Lett. **6**, 2038-2042

[2] Andreani, C., et al (2014). *Discussion: Nuclear Quantum Dynamics - Protons and Beyond*. J. Phys. Conf. Ser. **571**(1),012004

[3] Andreani, C., et al (2014). *Discussion: Measurement and Instrumentation*. J. Phys. Conf. Ser. **571**(1),012010

[4] Ceriotti, M., et al (2014). *Discussion: Theoretical Horizons and Calculation*. J. Phys. Conf. Ser. **571**(1),012013

[5] Briganti, G., et al (2016). *Neutron Scattering Observation of Quasi-free Rotations of Water Confined in Carbon Nanotubes*. Sci. Rep., submitted

[6] Greicius, Tony ed. *The Solar System and Beyond is Awash in Water*. July 31, 2015. NASA. <https://www.nasa.gov/jpl/the-solar-system-and-beyond-is-awash-in-water>

[7] Ball, P. *Life's Matrix: A Biography of Water*. Berkeley and Los Angeles: University of California Press, 2001

[8] Qin, W., L. Wang and D. Zhong (2016). *Dynamics and Mechanism of Ultrafast Water–Protein Interactions*. PNAS Early Edition, doi:10.1073/pnas.1602916113

[9] Speedy, R.J., and C.A. Angell (1976). *Isothermal Compressibility of Supercooled Water and Evidence for a Thermodynamic Singularity at -45 °C*. J. Chem. Phys. **65**, 851-858

[10] Speedy, R.J. (1982). *Stability-limit conjecture. An interpretation of the properties of water*. J. Phys. Chem. **86**, 982-991

[11] Mishima, O., and H.E. Stanley (2008). *The Relationship between Liquid, Supercooled and Glassy Water*. Nature **396**, 329-335

[12] Debenedetti, P.G., and H.E. Stanley. *Supercooled and Glassy Water*. Physics Today, June 2003, 40-46

[13] Poole, P.H., et al (1992). *Phase Behaviour of Metastable Water*. Nature **360**, 324-328

[14] Xu, L., et al (2005). *Relation between the Widom Line and the Dynamic Crossover in Systems with a Liquid-Liquid Phase Transition*. PNAS USA **102**(46), 16558-16562

[15] Roentgen, W.C. (1892). *Ueber die Constitution des Fluessigen Wassers*. Annu. Phys. u. Chem. **45**, 91

[16] Stillinger, F.H., and A. Rahman (1974). *Improved Simulation of Liquid Water by Molecular Dynamics*. J. Chem. Phys. **60**, 1545-1557

[17] Chen, S.-H.., et al (2006). *The Violation of the Stokes–Einstein Relation in Supercooled Water*. PNAS USA **103**(35), 112974-12978

[18] Cerveny, S., et al (2016). *Confined Water as Model of Supercooled Water*. Chem. Rev. **116**, 7608-7625

[19] Sellberg, J.A., et al (2014). *Ultrafast X-Ray Probing of Water Structure Below the Homogeneous Ice Nucleation Temperature*. Nature **510**, 381-384

[20] Limmer, D.T., and D. Chandler (2011). *The Putative Liquid-Liquid Transition is a Liquid-Solid Transition in Atomistic Models of Water*. J. Chem. Phys. **135**, 134503

[21] Limmer, D.T., and D. Chandler (2013). *The Putative Liquid-Liquid Transition is a Liquid-Solid Transition in Atomistic Models of Water.II*. J. Chem. Phys. **138**, 214504

[22] Chandler, D. (2014). *Illusions of Phase Coexistence: Comments on 'Metastable Liquid-Liquid Transition in a Molecular Model of Water' by J.C. Palmer et al.* Nature **510**, 385, arXiv:1407.6854

[23] Sastry, S., et al (1996). *Singularity-free Interpretation of the Thermodynamics of Supercooled Water*. Phys. Rev. E **53**, 6144-6154

[24] Arunan, E., et al (2011). *Definition of the Hydrogen Bond (IUPAC Recommendations 2011)*. Pure Appl. Chem. **83**(8), 1637-1641

[25] Isaacs, E.D., et al (1999). *Covalency of the Hydrogen Bond in Ice: A Direct X-Ray Measurement*. Phys. Rev. Lett. **82**(3), 600-603

[26] Pauling, L. (1935). *The Structure and Entropy of Ice and of Other Crystals with Some Randomness of Atomic Arrangement*. J. Am. Chem. Soc. **57**, 2680

[27] Maerchal, Y. *The Hydrogen Bond and the Water Molecule*. Elsevier Science, 2006

[28] Laage, D., and J.T. Hynes (2006). *A Molecular Jump Mechanism of Water Reorientation*. Science **311**(5762), 832-835

[29] Head-Gordon, T., and M.E. Johnson (2006). *Tetrahedral Structure or Chains for Liquid Water*. PNAS USA **103**, 7973-7977

[30] Scherm, R. (1972). *Fundamentals of Neutron Scattering by Condensed Matter*. Ann. Phys. **7**, 349-370

[31] Fernandez-Alonso, F., and D.L. Price eds. (2013). *Neutron Scattering - Fundamentals*. Experimental Methods in the Physical Sciences **44**

[32] Seel, A.G., R. Senesi, and F. Fernandez-Alonso (2014). *The VI Workshop in Electron Volt Neutron Spectroscopy: Frontiers and Horizons*. J. Phys.: Conf. Ser. **571**, 011001

[33] Callaghan, P.T. *Translational Dynamics and Magnetic Resonance: Principles of Pulsed Gradient Spin Echo NMR*. Oxford: Oxford University Press, 2011

[34] Havriliak, S. Jr. and S. Havriliak *Dielectric and Mechanical Relaxation in Materials*. New York: Hanser, 1997

[35] Kirstein, O. (2013). *Neutron Science and Instruments*. ESS Technical Design Report, Chapter 2. URL: http://eval.esss.lu.se/cgi-bin/public/DocDB/ShowDocument?docid=274

[36] Romanelli, G., et al (2015). *Probing the Effects of 2D Confinement on Hydrogen Dynamics in Water and Ice Adsorbed in Graphene Oxide Sponges*. PCCP **17**, 31680-31684

[37] Ceriotti, M., et al (2016). *Nuclear Quantum Effects in Water and Aqueous Systems: Experiment, Theory, and Current Challenges*. Chem. Rev. **116**, 7529-7550

[38] Gainaru, C., et al (2014). *Anomalously Large Isotope Effect in the Glass Transition of Water*. 10.1073/pnas.1411620111

[39] McKenzie, R.H., et al (2014). *Effect of Quantum Nuclear Motion on Hydrogen Bonding*. J. Chem. Phys. **140**, 174508

[40] Habershon, S., T.E. Markland, and D.E. Manolopoulos (2009). *Competing Quantum Effects in the Dynamics of a Flexible Water Model*. J. Chem. Phys. **131**, 024501

[41] Markland, T.E., and B.J. Berne (2012). *Unraveling Quantum Mechanical Effects in Water using Isotopic Fractionantion*. PNAS USA **109**, 7988-7991

[42] Li, X.-Z., B. Walker, and A. Michaelides (2011). *Quantum Nature of the Hydrogen Bond*. PNAS USA **108**(16), 6369-6373

[43] Ceriotti, M., and T.E. Markland (2013). *Efficient Methods and Practical Guidelines for Simulating Isotope Effects*. J. Chem. Phys. **138**, 014112

[44] Garbuio, V., et al (2007). *Proton Quantum Coherence Observed in Water Confined in Silica Nanopores*. J. Chem. Phys. **127**, 154501

[45] Pantalei, C., et al (2008). *Proton Momentum Distribution of Liquid Water from Room Temperature to the Supercritical Phase*. Phys. Rev. Lett. **100**, 177801

[46] Romanelli, G., et al (2013). *Direct Measurement of Competing Quantum Effects on the Kinetic Energy of Heavy Water upon Melting*. J. Phys. Chem. Lett. **4**, 3251-3256

[47] Andreani, C., G. Romanelli, and R. Senesi (2013). *A Combined INS and DINS Study of Proton Quantum Dynamics of Ice and Water across the Triple Point and in the Supercritical Phase*. Chem. Phys. **427**, 106-110

[48] Nakagawa, H., et al (2014). *Local dynamics coupled to hydration water determines DNA-sequence-dependent deformability*. Phys. Rev. E **90**, 022723

[49] Bergmann, U., et al (2007). *Isotope Effects in Liquid Water Probed by X-ray Raman Spectroscopy*. Phys. Rev. B: Condens. Matter Mater. Phys. **76**, 024202

[50] Lehmkuehler, F., et al (2016). *Intramolecular Structure and Energetics in Supercooled Water down to 255 K*. PCCP **18**, 6925

[51] Wernet, Ph., et al (2004). *The Structure of the First Coordination Shell in Liquid Water*. Science **304**(5673), 995-999

[52] Harada, Y., et al (2013). *Selective Probing of the OH or OD Stretch Vibration in Liquid Water using Resonant Inelastic Soft-X-ray Scattering*. Phys. Rev. Lett. **111**(19), 193001

[53] Diken, E.G., et al (2004). *Isotopic Fractionation and Zero-Point Effects in Anionic H-bonded Complexes: A Comparison of the $I^- \cdot HDO$ and $F^- \cdot HDO$ Ion–Molecule Clusters*. Chem. Phys. Lett. **387**, 17-22

[54] Soper, A.K., and C.J. Benmore (2008). *Quantum Differences between Heavy and Light Water*. Phys. Rev. Lett. **101**, 065502

[55] Kumagai, T., et al (2010). *Symmetric Hidrogen Bond in a Water-Hydroxyl Complex on Cu(110)*. Phys. Rev. B: Condens. Matter Mater. Phys. **81**, 045402

[56] Guo, R., et al (2016). *Nuclear Quantum Effects of Hydrogen Bonds Probed by Tip-enhanced Inelastic Electron Tunneling*. Science **352**(6283), 321-325

[57] Bakker, H.J., and H.-K. Nienhuys (2002). *Delocalization of Protons in Liquid Water*. Science **297**(5581), 587-590

[58] Maksyutenko, P., T.R. Rizzo, and O.V. Boyarkin (2006). *A direct measurement of the dissociation energy of water*. J. Chem. Phys. **125**, 181101

[59] Hardy, E.H., et al (2001). *Isotope Effect on the Translational and Rotational Motion in Liquid Water and Ammonia*. J. Chem. Phys. **114**, 3174

[60] Mallamace, F., et al (2008). *Thermodynamic Properties of Bulk and Confined Water*. J. Chem. Phys. **141**, 18C504

[61] Fei, Y., and T. Gao (2015). *Dielectric Anomaly in Ice near 20 K: Evidence of Macroscopic Quantum Phenomena*. J. Phys. Chem. Lett. **6**(14), 2822–2825

[62] Paciaroni, A., et al (2008). *Fingerprints of Amorphous Icelike Behavior in the Vibrational Density of States of Protein Hydration Water*. Phys. Rev. Lett. **101**, 148104

[63] Freedman, M.A. (2015). *Potential Sites for Ice Nucleation on Aluminosilicate Clay Minerals and Related Materials*. J. Phys. Chem. Lett. **6**(19), 3850-3858

[64] Hanslmeier, A. *Water in the Universe*. Springer, 2011

[65] Kikuchi, Y., et al (2011). *Analysis of Supercritical Water Oxidation for Detoxification of Waste Organic Solvent in University Based on Life Cycle Assessment*. J. Haz. Mat. **194**, 283-289

[66] Fomin, Y.D., et al (2015). *Dynamical Crossover Line in Supercritical Water*. Nature Scientific Reports **5**, 14234

[67] Svishchev, I.M., and D.A. Guzonas (2011). *Supercritical Water and Particle Nucleation: Implications for Water Chemistry Control in a GEN IV Supercritical Water Cooled Nuclear Reactor* J. Supercrit. Fluids **60**, 121-126

[68] Ossi, P.M. *Disordered Materials - An Introduction*. Berlin: Springer-Verlag, 2006

[69] Loerting, T., V.V. Brazhkin, and T. Morishita (2009). *Multiple Amorphous-Amorphous Transitions*. Adv. Chem. Phys. **143**, 29-82

[70] De Podesta, M. *Understanding the Properties of Matter*. London: CRC Press, Taylor & Francis Group, 2002

[71] Johari, G.P., S. Ram, G. Astl, and E. Mayer (1990). *Characterizing Amorphous and Microcrystalline Solids by Calorimetry*. J. Non-Cryst. **116**, 282-285

[72] Angell, C.A. (1995). *Formation of Glasses from Liquids and Biopolymers*. Science **267**, 1924

[73] Bernstein, J. *Polymorphism in Molecular Crystals*. Oxford: Oxford University press, 2002

[74] Palatnik, L.S., A.A. Nechitailo, and A.A. Kozma (1981). *Polyamorphism and Short-Range Order Substructure in Amorphous Boron Films*. Akademiia Nauk SSSR, Doklady **261**(5), 1134-1137

[75] Loerting, T., et al (2011). *How Many Amorphous Ices are There?*. PCCP **13**, 8783-8794

[76] Mishima, O., L.D. Calvert, and E. Whalley (1984). *'Melting Ice' I at 77 K and 10 kbar: A New Method of Making Amorphous Solids*. Nature **310**, 393-395

[77] Machon, D., et al (2014). *Pressure-Induced Amorphization and Polyamorphism: Inorganic and Biochemical Systems*. Progress in Materials Science **61**, 216-282

[78] Burton, E.F., and W.F. Oliver (1935). *X-Ray Diffraction Patterns of Ice*. Nature **135**, 505-506

[79] Loerting, T., et al (2006). *High Density Amorphous Ice from Cubic Ice*. Chem. Phys. Chem. **7**, 1203-1206

[80] Nelmes, R.J., et al (2006). *Annealed High-Density Amorphous Ice under Pressure*. Nature Physics **2**, 414-418

[81] Loerting, T., et al (2001). *A Second Distinct Structural 'State' of High-Density Amorphous Ice at 77 K and 1 bar*. PCCP **3**, 5355-5357

[82] Handa, Y.P., O. Mishima, and E. Whalley (1986). *High-Density Amorphous Ice. III. Thermal Properties*. J. Chem. Phys. **84**, 2766-2770

[83] Winkel, K., et al (2009). *Relaxation Effects in Low Density Amorphous Ice: Two Distinct Structural States Observed by Neutron Diffraction*. J. Chem. Phys. **130**, 204502

[84] Loerting, T. (2016). *Amorphous Ices: Dynamics*. Lecture - Erice School 2016 - Water and Water Systems

[85] Tainter, C.J., L. Shi, and J.L. Skinner (2014). *Structure and OH-stretch Spectroscopy of Low- and High-Density Amorphous Ices*. J. Chem. Phys. **140**, 134503

[86] Mueller, U. *Inorganic Structural Chemistry*. Chichester, UK: J. Wiley and Sons, 2006

[87] Guthrie, M., et al (2004). *A Structural Study of Very High-Density Amorphous Ice*. Chem. Phys. Lett. **397**, 335-339

[88] Giovanbattista, N., K. Amann-Winkel, and T. Loerting (2013). *Amorphous Ices*. Adv. Chem. Phys. **152**, 139-173

[89] Loerting, T., et al (2015). *The Glass Transition in High-Density Amorphous Ice*. J. Non-Cryst. Solids **407**, 423-430

[90] Levinger, N.E. (2002). *Water in confinement*. Science **298**, 1722-1723

[91] Chonde, M., M. Brindza, and V. Sadtchenko (2006). *Glass Transition in Pure and Doped Amorphous Solid Water: An Ultrafast Microcalorimetry Study*. J. Chem. Phys. **125**, 094501

[92] Sepulveda, A., et al (2012). *Glass Transition in Ultrathin Films of Amorphous Solid Water*. J. Chem.Phys. **137**, 244506

[93] Johari, G.P., A. Hallbrucker, and E. Mayer (1987). *The Glass-Liquid Transition of Hyperquenced Water*. Nature **330**, 552-553

[94] Seidl, M., et al (2011). *Volumetric Study Consistent with a Glass-to-Liquid Transition in Amorphous Ices under Pressure*. Phys. Rev. B **83**, 100201(R)

[95] Loew, F., et al (2013). *Ultra-Slow Dynamics in Low Density Amorphous Ice Revealed by Deuteron NMR: Indication of a Glass Transition*. PCCP **15**, 9308-9314

[96] Elsaesser, M.S., et al (2010). *Reversibility and Isotope Effect of the Calorimetric Glass-to-Liquid Transition of Low-Density Amorphous Ice*. PCCP **12**(3), 708-712

[97] Angell, C.A. (2008). *Insights into Phases of Liquid Water from Study of its Unusual Glass-Forming Properties*. Science **319**, 582-587

[98] Shephard, J.J., J.S.O. Evans, and C.G. Salzmann (2013). *Structural Relaxation of Low-Density Amorphous Ice upon Thermal Annealing*. J. Phys. Chem. Lett. **4**, 3672-3676

[99] Salzmann, C.G., et al (2011). *The Polymorphism of Ice: Five Unresolved Questions*. PCCP **13**, 18468–18480

[100] Tulk, C.A., et al (2002). *The Low-Frequency Density of States for Amorphous and Crystalline Ices*. Appl. Phys. A **74** [Suppl.], S1185-S1187

[101] Kolesnikov, A.I., et al (1995). *Similarity of Vibrational Spectra of High-Density Amorphous Ice and High-Pressure Phase Ice VI*. Physica B **213**&**214**, 474

[102] Schober, H., et al (2000). *Crystal-like High Frequency Phonons in the Amorphous Phases of Solid Water*. Phys. Rev. Lett. **85**, 4100-4103

[103] Tse, J.S., et al (2000). *Origin of Low-Frequency Local Vibrational Modes in High Density Amorphous Ice*. Phys. Rev. Lett. **85**, 3185

[104] Mishima, O. (2004). *The Glass-to-Liquid transition of the Emulsified High-Density Amorphous Ice made by Pressure-induced Amorphization*. J. Chem. Phys. **121**, 3161

[105] Andersson, O. (2008). *Dielectric Relaxation of the Amorphous Ices*. J. Phys.:Condens. Matter **20**, 244115

[106] Bassett, W.A., et al (1993). *A New Diamond Anvil Cell for Hydrothermal Studies to 2.5 GPa and from -190 to 1200 °C*. Rev. Sci. Instrum. **64**, 2340

[107] McMillan, P.F., and H.E. Stanley (2010). *Going Supercritical*. Nature Physics **6**, 479-480

[108] Tassaing, T., Y. Danten, and M. Besnard (2002). *Infrared Spectroscopic Study of Hydrogen-Bonding in Water at High Temperature and Pressure*. J. Mol. Liq. **101**(1-3), 149-158

[109] Sahle, C.J., et al (2013). *Microscopic Structure of Water at Elevated Pressures and Temperatures*. PNAS USA **110**(13), 6301-6306

[110] Smiechovski, M., et al (2016). *Correlated Particle Motion and THz Spectral Response of Supercritical Water*. Phys. Rev. Lett. **116**, 027801

[111] Stanley, H.E. *Introduction to Phase transitions and Critical Phenomena*. New York: Oxford University Press, 1971

[112] Brazhkin, V.V., et al (2012). *Where is the Supercritical Fluid on the Phase Diagram?*. Physics - Uspecki **55**(11), 1061-1079

[113] Gallo, P., D. Corradini, and M. Rovere (2014). *Widom Line and Dynamical Crossovers as Routes to Understand Supercritical Water*. Nature Communications **5**, 5806

[114] Imre, A.R., et al (2012). *The Pseudocritical Regions for Supercritical Water*. Nucl. Eng. Des. **252**, 179-183

[115] Wagner, W., and A. Pru„ (2002). *The IAPWS Formulation 1995 for the Thermodynamic Properties of Ordinary Water Substance for General and Scientific Use*. J. Phys. Chem. Ref. Data **31**, 387-535

[116] Simeoni, G.G., et al (2010). *The Widom Line as the Crossover between Liquid-like and Gas-like Behaviour in Supercritical Fluids*. Nature Phys. **6**, 503

[117] Brazhkin, V.V., et al (2013). *'Liquid-Gas' Transition in the Supercritical Region: Fundamental Changes in the Particle Dynamics*. PRL **111**, 145901

[118] Franzese, G., and H.E. Stanley (2007). *The Widom Line of Supercooled Water*. J. Phys.: Condens. Matter **19**, 205126

[119] Prielmeier, F.X., et al (1987). *Diffusion in Supercooled Water to 300 MPa*. Phys. Rev. Lett. **59**, 1128

[120] Ito, K., C.T. Moynihan, and C.A. Angell (1999). *Thermodynamic Determination of Fragility in Liquids and a Fragile-to-Strong Liquid Transition in Water*. Nature **398**, 492-495

[121] Adam, G., and J.H. Gibbs (1965). *On the Temperature Dependence of Cooperative Relaxation Properties in Glass-Forming Liquids*. J. Chem. Phys. **43**, 139-146

[122] Sillescu, H. (1999). *Heterogeneity at the Glass Transition: a Review*. J. Non-Cryst. Solids **243**, 81-108

[123] Tanaka, H., et al (2010). *Critical-Like Behaviour of Glass-Forming Liquids*. Nature Materials **9**, 324-331

[124] van Hove, L. (1954). *Correlations in Space and Time and Born Approximation Scattering in Systems of Interacting Particles*. Phys. Rev. **95**, 249

[125] Fultz, B., et al. *Experimental Inelastic Neutron Scattering - Introduction to DANSE*. Springer-Verlag, 2009

[126] Fermi, E. (1936). *Motion of Neutrons in Hydrogenous Substances*. Ricerca Scientifica **7**, 13-52

[127] Scopigno, T., G. Ruocco, and F. Sette (2005). *Microscopic Dynamics in Liquid Metals: The Experimental Point of View*. Rev. Mod. Phys. **77**, 881

[128] Rahman, A., K.S. Singwi, and A. Sjoelander (1962). *Theory of Slow Neutron Scattering by Liquids. I*. Phys. Rev. **126**(3), 986-996

[129] De Gennes, P.G. (1959). *Liquid dynamics and inelastic scattering of neutrons*. Physica **25**, 825

[130] Colognesi, D., M. Celli, and M. Zoppi (2004). *Density of Phonon States in Solid Parahydrogen from Inelastic Neutron Scattering*. J. Chem. Phys. **120**, 5657

[131] Young, J.A., and J.U. Koppel (1964). *Slow Neutron Scattering by Molecular Hydrogen and Deuterium*. Phys. Rev. **135**, A603-611

[132] Dawidowski, J., et al (2002). *Analysis of Multiple Scattering and Multiphonon Contributions in Inelastic Neutron Scattering Experiments*. Nuclear Instruments and Methods in Physics Research B **195**, 389-399

[133] Andreani, C., et al (2005). *Measurement of Momentum Distribution of Light Atoms and Molecules in Condensed Matter Systems using Inelastic Neutron Scattering*. Adv. Phys. **54**(5), 377-469

[134] Senesi, R. (2012). *Direct Kinetic Energy Extraction from Neutron Compton Profiles*. Nucl. Instr. Meth. Phys. Res. **661**, 70-76

[135] Vega, C., et al (2010). *Heat Capacity of Water: A Signature of Nuclear Quantum Effects*. J. Chem. Phys. **132**, 046101

[136] West, G.B. (1975). *Electron scattering from atoms, nuclei and nucleons*. Phys. Rev. C **18**, 263-323

[137] Sears, V.F. (1984). *Scaling and Final-State Interactions in Deep-Inelastic Neutron Scattering*. Phys. Rev. B **30**, 44

[138] Watson, G.I. (1996). *Neutron Compton Scattering*. J. Phys.: Condens. Matter. **8**, 5955-5975

[139] Dianoux, A.-J., and G. Lander. *Neutron Data Booklet*. ILL: Old City Publishing Group, 2003

[140] Pietropaolo, A., and R. Senesi (2011). *Electron Volt Neutron Spectrometers*. Physics Reports **508**, 45-90

[141] Karlsson, M. (2015). *Proton Dynamics in Oxides: Insight into the Mechanics of Proton Conduction from Quasielastic Neutron Scattering*. PCCP **17**, 26-38

[142] Seel, A.G., M. Krzystyniak, and F. Fernandez-Alonso (2014). *The VESUVIO Spectrometer Now and When?*. J. Phys.: Conference Series **571**, 012006

[143] Gorini, G., G. Festa, and C. Andreani (2014). *Epithermal Neutron Instrumentation at ISIS*. J. Phys.: Conference Series **571**, 012005

[144] Mayers, J., and A.M. Adams (2011). *Calibration of an Electron Volt Neutron Spectrometer*. Nuclear Instruments and Methods in Physics Research A **625**, 47-56

[145] Flammini, D., et al (2012). *Spherical Momentum Distribution of the Protons in Hexagonal Ice from Modeling of Inelastic Neutron Scattering Data*. J. Chem. Phys. **136**, 024504

[146] Krzystyniak, M., et al (2013). *Mass-selective Neutron Spectroscopy of Lithium Hydride and Deuteride: Experimental Assessment of the Harmonic and Impulse Approximations*. Phys. Rev. B **88**, 184304

[147] Mayers, J. (2011). *Calculation of Background Effects on the VESUVIO eV Neutron Spectrometer*. Meas. Sci. Technol. **22**, 015903

[148] Mayers, J. (2011). Technical Report RAL-TR-2011-003, STFC

[149] Lin, L., et al (2011). *Momentum distribution, Vibrational Dynamics, and the Potential of Mean Force in Ice*. Phys. Rev. B **83**, 220302

[150] Neumann, K.U., O. Schaerpf, and K.R.A. Ziebeck (1992). *On the question of the origin for a spherical average in scattering experiments*. Physica B: Condens. Matt. **180-181**, Part 2, 817-818

[151] Reiter, G.F., J. Mayers, and J. Noreland (2002). *Momentum-Distribution Spectroscopy using Deep Inelastic Neutron Scattering*. Phys. Rev. B **65**, 104305

[152] James, F. *MINUIT Minimization Package*. Geneva: Reference Manual CERN Program Library, 1994

[153] Trzesniak, D., A.-P. E. Kunz, and W.F. van Gunsteren (2007). *A Comparison of Methods to Compute the Potential of Mean Force*. Chem. Phys. Chem. **8**, 162-169

[154] Harmandaris, V.A., et al (2006). *Hierarchical Modeling of Polystyrene: From Atomistic to Coarse-Grained Simulations*. Macromolecules **39**, 6708-6719

[155] Straatsma, T.P., and J.A. McCammon (1992). *Computational Alchemy*. Annu. Rev. Phys. Chem. **43**, 407-435

[156] Brandsdal, B.O., et al (2003). *Free Energy Calculations and Ligand Binding*. Adv. Protein Chem. **66**, 123-158

[157] Kirkwood, J.G. (1935). *Statistical Mechanics of Fluid Mixtures*. J. Chem. Phys. **3**, 300-313

[158] Morrone, J.A., and R. Car (2008). *Nuclear Quantum Effects in Water*. Phys. Rev. Lett. **101**, 017801

[159] Lin, L., et al (2010). *Displaced Path Integral Formulation for the Momentum Distribution of Quantum Particles*. Phys. Rev. Lett. **105**, 110602

[160] Morrone, J.A., et al (2007). *Proton Momentum Distribution in Water: an Open Path Integral Molecular Dynamics Study*. J. Chem. Phys. **126**, 234504

[161] Gonzalez, M.A., and J.L.F. Abascal (2011). *A Flexible Model for Water Based on TIP4P/2005*. J. Chem. Phys. **135**, 224516

[162] Burns, K., K. Adams, and J. Longwell (1950). *Interference Measurements in the Spectra of Neon and Natural Mercury*. J. Opt. Soc. Am. **40**, 339-344

[163] Senesi, R., et al (2013). *Temperature Dependence of the Zero Point Kinetic Energy in Ice and Water Above Room Temperature*. Chem. Phys. **427**, 111-116

[164] Roettger, K., et al (1994). *Lattice Constants and Thermal Expansion of H_2O and D_2O Ice Ih Between 10 and 265 K*. Acta Cryst. **B50**, 644-648

[165] Cheng, B., J. Beheler, and M. Ceriotti (2016). *Nuclear Quantum Effects in Water at the Triple Point: Using Theory as a Link between Experiments*. J. Phys. Chem. Lett. **7**, 2210-2215

[166] Moreh, R., and D. Nemirovsky (2010). *On the Proton Kinetic Energy in H_2O and in Nanotube Water*. J. Chem. Phys. **133**, 084506

[167] Finkelstein, Y., and R. Moreh (2013). *Proton Dynamics in Ice VII at High Pressures*. J. Chem. Phys. **139**, 044716

[168] Minceva-Sukarova, B., W.F. Sherman, and G.R. Wilkinson (1944). *The Raman Spectra of Ice (I_h, II, III, V, VI and IX) as Functions of Pressure and Temperature*. J. Phys. C **17**, 5833-5850

[169] Senesi, R., et al (2013). *The Quantum Nature of the $O-H$ Stretching Mode in Ice and Water Probed by Neutron Scattering Experiments*. J. Chem. Phys. **139**, 074504

[170] Temelso, B., and G.C. Shields (2011). *The Role of Anharmonicity in Hydrogen-Bonded Systems: The Case of Water Clusters*. J. Chem. Theory Comput. **7**, 2804-2817

[171] Lamb, W.J., G.A. Hoffman and J. Jonas (1981). *Self-Diffusion in Compressed Supercritical Water*. J. Chem. Phys. **74**(12), 6875-6880

[172] Andreani, C., et al (2001). *Proton Dynamics in Supercritical Water*. J. Chem. Phys. **115**(24), 11243-11248

[173] Ricci, M.A., et al (1998). *Light and Neutron Scattering Studies of the OH Stretching Band in Liquid and Supercritical Water*. J. Chem. Phys. **108**, 450

[174] Skarmoutsos, I., and E. Guardia (2010). *Effect of the Local Hydrogen Bonding Network on the Reorientational and Translational Dynamics in Supercritical Water*. J. Chem. Phys. **132**, 074502

[175] Bencivenga, F., et al (2009). *High Frequency Dynamics in Liquids and Supercritical Fluids: A Comparative Inelastic X-Ray Scattering Study*. J. Chem. Phys. **130**, 064501

[176] Bencivenga, F., et al (2007). *Structural and Collisional Relaxations in Liquids and Supercritical Fluids*. Phys. Rev. Lett. **98**, 085501

[177] Walrafen, G.E., and Y.C. Chu (1995). *Linearity between Structural Correlation Length and Correlated-Proton Raman Intensity from Amorphous Ice and Supercooled Water up to Dense Supercritical Steam*. J. Phys. Chem. **99**, 11225-11229

[178] Puls, M.P. *The Effect of Hydrogen and Hydrides on the Integrity of Zirconium Alloy Components*. London: Springer-Verlag, 2012

[179] Whittermore, W.L. (1964). *Neutron Interactions in Zirconium Hydride*. General Atomic 4490 (Rev.)

[180] Evans, A.C., J. Mayers, and D.N. Timms (1993). *Deep Inelastic Neutron Scattering in the Study of Atomic Momentum Distributions*. Z. Naturforsch. **48**a, 425-432

[181] Evans, A.C., J. Mayers, and D.N. Timms (1996). *Neutron-Scattering Study of the Impulse Approximation in ZrH_2*. Phys. Rev. B **53**, 3023

[182] Ramirez, R., et al (2012). *Quasi-Harmonic Approximation of Thermodynamic Properties of Ice I_h, II, and III*. J. Chem. Phys. **137**, 044502

[183] Koza, M.M. (2008). *Vibrational Dynamics of Amorphous Ice Structures Studied by High-Resolution Neutron Spectroscopy*. Phys. Rev. B: Condens. Matter Mater. Phys. **78**, 064303

[184] Chumakov, A.I., et al (2014). *Role of Disorder in the Thermodynamics and Atomic Dynamics of Glasses*. Phys. Rev. Lett. **112**, 025502

[185] Huang, C., et al (2009). *The Inhomogeneous Structure of Water at Ambient Conditions*. PNAS USA **106**(36), 15214

[186] Stillinger, F.H., and P.G. Debenedetti (2013). *Glass Transition Thermodynamics and Kinetics*. Annu. Rev. Conedens. Matter Phys. **4**, 263-285

[187] Lubchenko, V. (2015). *Theory of the Structural Glass Transition: A Pedagogical Review*. Adv. Phys. **64**(3), 283-443

[188] Lubchenko, V., and P.G. Wolynes (2007). *Theory of Structural Glasses and Supercooled Liquids*. Annu. Rev. Phys. Chem. **58**, 235-266

[189] Hansen, J.-P., and I.R. McDonald *Theory of Simple Liquids*. Academic Press, 2013

[190] Egelstaff, P.A. *An Introduction to the Liquid State*. Oxford: Clarendon Press, 1992

[191] Reiter, G.F., and R. Silver (1985). *Measurement of Interionic Potentials in Solids Using Deep-Inelastic Neutron Scattering*. Phys. Rev. Lett. **54**, 1047

[192] Morse, P.M. (1929). *Diatomic Molecules According to the Wave Mechanics. II. Vibrational Levels*. Phys. Rev. **34**(1), 57-64

[193] Dahl, J.P., and M. Springborg (1988). *The Morse Oscillator in Position Space, Momentum Space, and Phase Space*. J. Chem. Phys. **88**, 4535

[194] Abramowitz, M., and I.A. Stegun *Handbook of Mathematical Functions*. New York: Dover Publications, Inc., 1970

[195] Ceperley, D.M. (1995). *Path Integrals in the Theory of Condensed Helium*. Rev. Mod. Phys. **67**(2), 279-355

A

Glass transition: the jargon

In glass-formers the higher heat capacity normally exhibited by the liquid compared to its crystal tends to persist and magnify upon supercooling down to the experimental glass transition temperature T_g (Fig. A.1), with internal relaxation times suddenly exceeding practical measurement times, typically falling in the $10^2 - 10^3$ s range [186].
If one calculates the entropy change

$$\Delta S(T) = \Delta S(T_m) \int_T^{T_m} \frac{dT'}{T'} \left[C_p^{liq}(T') - C_p^{cr}(T') \right] \tag{A.1}$$

upon further cooling at the prevailing pressure, this quantity apparently vanishes linearly as a function of $T - T_K$ at a Kauzmann temperature $0 < T_K < T_g$. Analogously the enthalpy of the extrapolated liquid remains significantly above the crystalline counterpart at T_K, which implies that the two phases would remain structurally distinct. This is a paradox, since a configurationally disordered liquid would possess a lower entropy than its periodically ordered crystal phase, traveling towards negative absolute entropy at $T = 0$. The paradox gets fixed if the disordered phase is thought to exhibit an 'ideal' higher-than-first-order phase transition[1] at T_K, below which it would remain basically unchanged from the structural point of view, as does the crystal.
The Kauzmann temperature identified on the basis of static measurable thermal properties[2] might have implications on kinetic properties, too, such as shear viscosity (η), mean shear-stress (τ_{shear}) and thermal-relaxation (τ_{therm}) times, and self-diffusion constant (D). Historically, the experimental trends of such properties have been approximately fitted to the generic Vogel-Tammann-Fulcher (VTF) function $Ae^{\frac{C}{T-T_0}}$, with C and T_0 positive constants, and A showing a weak dependence on T. The extent to which measurements are close to, or deviate from, a pure Arrhenius behavior (corresponding to $T_0 = 0$) allows for the traditional arrangement of glass formers into a strong-vs-fragile scale, with one possible measure of 'strength' via the dimensionless quantity $\frac{C}{T_0}$ (that is, the more Arrhenius the behavior, the stronger

[1] Actually, the glass transition is not a real phase transition, but rather sort of kinetic arrest [187]. It can be imparted certain features of a 2^{nd}-order phase transition, since, employing a rapid enough quench, the entropy experiences a discontinuity in its temperature derivative. This is due to the vanishing of the component of the heat capacity concerning the reconfigurational motions of the particles, with C_p exhibiting a jump at T_g. Experimentally the quench rate is always finite, which implies that the discontinuity in the heat capacity is partially smeared out.

[2] To be precise, the Kauzmann criterion $\Delta S(T) = 0$ for an ideal glass transition is replaced, in the large-system limit, by the vanishing of $\frac{\Delta S(T)}{N}$ at T_K.

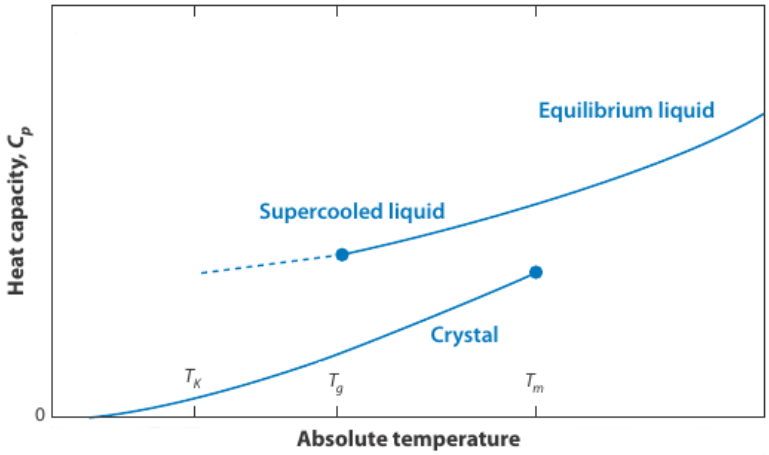

Figure A.1: Isobaric heat capacities for the equilibrium- ($T \geq T_m$), supercooled liquid ($T \leq T_m$), and equilibrium crystal ($0 < T < T_m$). T_m is what's labeled T_M in Fig. 1.4 (equilibrium melting). The dashed line is an extrapolation below T_g. Reproduced from [186] with modifications.

the material). It's the lying very close to T_K of the divergence of the empirical VTF expression at T_0 to suggest that the static criterion may be automatically accompanied by singularities in kinetic parameters [188].
A further link resides in the Adam-Gibbs model of glasses [121]. The idea that underpins this formalization consists of relaxation and flow processes in the deeply supercooled regime proceeding via local structural excitations that occur within independent cooperatively rearranging regions (CRRs) of the medium. The number of CRRs is presumed roughly proportional to the inverse of their average volume over the range $0 < T < T_m$. Further, the mean value of CRR size, as well as of CRR excitation free energies, is argued to be inversely proportional to the difference in entropy between the liquid and crystal phases that can be ascribed to nonvibrational degrees of freedom ($\Delta S_{conf}(T)$). This way a typical relaxation time should go

$$\tau \sim \overline{A} e^{\frac{\overline{C}}{T\Delta S_{conf}(T)}} \tag{A.2}$$

with $\Delta S_{conf}(T)$ to be easily replaced by $\Delta S(T)$, being the vibrational contributions to the entropies of the two phases close enough that their difference can be neglected. As a result, if $\Delta S(T)$ vanishes at a $T_K > 0$, this would be accompanied by the divergence of measurable relaxation rates, and of the macroscopic shear viscosity.
Since the CRRs are treated as independent subsystems, they should undergo thermodynamic fluctuations.
Restricting standard relations of statistical thermodynamics to the slow degrees of freedom responsible of the transition process, by a suitable set of *ad hoc* assumptions it is possible to estimate characteristic length scales (ξ) for the system from experimental data [122].

B

Correlation: the pair distribution and van Hove functions

Two important members of the correlation-function tribe are known as the pair distribution and van Hove functions.
When the Hamiltonian of a system gets splitted into a kinetic and a potential contribution, the partition function can, in turn, be separated into a configurational (spatial) and a kinetic (momentum) component, and the derived thermodynamic functions into an ideal-gas and an excess (i.e., from interactions) part. An analogous factorization can be performed on the reduced distribution function ($n < N$) in the phase space at equilibrium [189]

$$f_0^{[n]}(\mathbf{r}^n, \mathbf{p}^n) = \rho_N^{(n)}(\mathbf{r}^n) f_M^{(n)}(\mathbf{p}^n) \tag{B.1}$$

where the $f_M^{(n)}$ is a product of n independent Maxwellians

$$f_M^{(n)}(\mathbf{p}^n) = \frac{exp(-\beta \sum_{i=1}^{n} \frac{|\mathbf{p}|_i^2}{2m})}{(2\pi m k_B T)^{\frac{3}{2}n}}; \tag{B.2}$$

while $\rho_N^{(n)}$ represents the n-particle equilibrium density

$$\rho_N^{(n)}(\mathbf{r}^n) = \frac{N!}{(N-n)!} \frac{1}{Z_N} \int exp(-\beta V_N) d\mathbf{r}^{N-n}, \tag{B.3}$$

which, when multiplicated as $\rho_N^{(n)}(\mathbf{r}^n) d\mathbf{r}^n$, returns the probability to find $n < N$ particles il the volume element $d\mathbf{r}^n$.
From $\rho_N^{(n)}(\mathbf{r}^n)$ the n-particle distribution function

$$g_N^{(n)}(\mathbf{r}^n) = \frac{\rho_N^{(n)}(\mathbf{r}_1, ..., \mathbf{r}_n)}{\prod_{i=1}^{n} \rho_N^{(1)}(\mathbf{r}_i)} \tag{B.4}$$

can be defined, which tells how much the system structure departs from complete randomness.
The pair distribution function $g_N^{(2)}(\mathbf{r}_1, \boldsymbol{r}_2)$ is obtained for $n = 2$.
If the system is homogeneous, then $\rho^n g_N^{(n)}(\mathbf{r}^n) = \rho_N^{(n)}(\mathbf{r}^n)$; if isotropic, too, then $g_N^{(2)}$ only depends on $r = |\mathbf{r}_2 - \mathbf{r}_1|$ (usually being called the radial distribution function, $g(r)$).
Being the ensemble average of the microscopic density expressed by

$$\rho_N^{(1)}(\mathbf{r}) =< \sum_{i=1}^{N} \delta(\mathbf{r} - \mathbf{r}_i) > \tag{B.5}$$

and the implication

$$\rho_N^{(2)}(\mathbf{r}, \mathbf{r}') =< \sum_{i=1}^{N} \sum_{j=1}^{N'} \delta(\mathbf{r} - \mathbf{r}_i)\delta(\mathbf{r}' - \mathbf{r}_j) > \Longrightarrow < \frac{1}{N} \sum_{i=1}^{N} \sum_{j=1}^{N'} \delta(\mathbf{r} - \mathbf{r}_j + \mathbf{r}_i) >=$$
$$= \frac{\rho^2}{N} \int g_N^{(2)}(\mathbf{r}, \mathbf{r}') d\mathbf{r}' = \rho g(r) \tag{B.6}$$

holding true, one can infer that $\rho_N^{(2)}(\mathbf{r}, \mathbf{r}')$ reproduces a spacial density-fluctuation correlation.
Further, the definition of $g(r)$ implies that, on average, the number of elementary units falling into the range between r and $r + dr$ with respect to a specific particle is $4\pi r^2 \rho g(r) dr$ (3D shell volume of radius dr), which means that the function peaks correspond to different neighbor shells around the selected particle.
The time-dependent van Hove correlation function $G(\mathbf{r}, t)$ is actually a generalization of $g(r)$. $G(\mathbf{r}, t)$ is expected to return the amount of correlation between a particle placed in $\mathbf{r_i}$ at instant t and another one placed in $\mathbf{r_j}$ at $t = 0$; thus, in the classical case, it is generally defined as

$$G(\mathbf{r}, t) = \frac{1}{N} < \sum_{i=1}^{N} \sum_{j=1}^{N} \delta(\mathbf{r} - \mathbf{r_i}(t) + \mathbf{r_j}(0)) > . \tag{B.7}$$

$G(\mathbf{r}, t)$ is related to density fluctuations, since

$$G(\mathbf{r}, t) = \frac{1}{N} \int d\mathbf{r}' < \rho(\mathbf{r} - \mathbf{r}', 0)\rho(\mathbf{r}', t) > \tag{B.8}$$

or, in the homogeneous case (no dependence on the spatial coordinate)

$$G(\mathbf{r} - \mathbf{r}', t - t') = \frac{1}{N} V < \rho(\mathbf{r}', t')\rho(\mathbf{r}, t) >= \frac{1}{\rho} < \rho(\mathbf{r}', t')\rho(\mathbf{r}, t) > . \tag{B.9}$$

Therefore, in the long-term limit ($t \to \infty$), $G(\mathbf{r} - \mathbf{r}', t - t')$ approaches ρ.
The quantum generalization of the van Hove function is straightforward

$$G(\mathbf{r}, t) = \frac{1}{N} \sum_{i=1}^{N} \sum_{j=1}^{N} \int d\mathbf{r}' < \delta(\mathbf{r}' - \mathbf{r_i}(t))\delta(\mathbf{r} + \mathbf{r_j}(0) - \mathbf{r}') >, \tag{B.10}$$

if $\mathbf{r_i}$ and $\mathbf{r_j}$ are now interpreted as non-commuting Heisenberg operators.
In the case of systems for which the symmetric or antisymmetric nature of the wavefunction is of little importance (distinguishable particles, Boltzmann statistics), a natural split of G into a self component $G_s(\mathbf{r}, t)$ and a distinct contribution $G_d(\mathbf{r}, t)$ occurs by separation of diagonal ($i = j$) from off-diagonal ($i \neq j$) terms. G_s and G_d are such that, at $t = 0$, $G(\mathbf{r}, 0) = G_s(\mathbf{r}, 0) + G_d(\mathbf{r}, 0) = \delta(r) + \rho g(r)$.
Finally, the following relation must be fulfilled by the real and imaginary parts of G

$$Im\, G(r,t) = -tanh\left(\frac{\hbar}{2k_B t}\frac{\partial}{\partial t}\right) Re\, G(\mathbf{r},t), \tag{B.11}$$

which is a detailed-balance condition and can be interpreted as a special case of the fluctuation-dissipation theorem expressing the link between the (linear) response of the system to a perturbation and its fluctuations in the absence of the same perturbation [31].

C

Time correlation: the VAC function

Time correlation functions are often used to describe time-dependent random and irreversible processes in condensed phases resulting from the interaction with the surroundings, so providing for a common instrument to deal with issues raised in the context of spectroscopy and relaxation phenomena.
Be $A(t)$ any time-dependent observable. This invokes a Heisenberg representation of the operators.
Its associated time autocorrelation function (TACF) is defined as follows

$$C_A(t,t') =< A(t)A(t') >= \frac{Tr(A(t)A(t')\rho)}{Tr(\rho)} \tag{C.1}$$

where ρ represents the equilibrium density matrix of the system.
In case the system is time-translationally invariant, one of the instants t or t' can be safely replaced by zero.
From a qualitative point of view, a TACF describes how long a given property of a system persists until it is averaged out by microscopic motions and interactions with its surroundings.
The characteristic time-scale of a random process is the correlation time, τ_c.
τ_c characterizes the time scale for $C_{\delta A}(t)$ (where $\delta A \equiv A - < A >$ represents a fluctuation) to decay to zero in the long run.
Notice how the correlation time can be conveniently obtained in terms of a fluctuation TACF

$$\frac{1}{< \delta A^2 >} \int_0^\infty dt < \delta A(t)\delta A(0) > . \tag{C.2}$$

The velocity autocorrelation function (VACF) is a prime TACF conveying significant many-body info when analyzing the vibrational or diffusive properties of a molecular system.
For one particle in a time-invariant system, along the x-direction it is defined as

$$z(\tau) = \frac{1}{3} < \mathbf{v}(\tau)\mathbf{v}(0) >=< \dot{x}(\tau)\dot{x}(0) > \tag{C.3}$$

and commonly normalized as follows

$$z(\tau) = \frac{< \dot{x}(\tau)\dot{x}(0) >}{\dot{x}(0)\dot{x}(0)}. \tag{C.4}$$

A link can be found between the VACF and the incoherent part S_i of the dynamic structure factor under appropriate approximations [190].
Let us assume that the one-particle component of the intermediate scattering function $F_i(\mathbf{q},t)$ is nearly a Gaussian function

$$F_i(q,t) =< e^{-i\mathbf{Q}\cdot\mathbf{R}(0)}e^{-i\mathbf{Q}\cdot\mathbf{R}(t)} >= e^{-\frac{Q^2}{2}<(\mathbf{R}(0)-\mathbf{R}(t))^2_Q>} + O(Q^4) \tag{C.5}$$

where $(\mathbf{R}(0)-\mathbf{R}(t))^2_Q$ is referred to the spatial component along the $\mathbf{Q}$-direction. This approximation is reasonable for classical systems, with the $O(Q^4)$-terms becoming negligible for $\mathbf{Q}\to\mathbf{0}$.
Differentiating Eq. C.5 twice with respect to t, one gets

$$\frac{1}{F_i(Q,t)}\frac{\partial^2 F_i(Q,t)}{\partial t^2} = -\frac{Q^2}{2}\frac{\partial^2 < (\mathbf{R}(0)-\mathbf{R}(t))^2_Q >}{\partial t^2}+\frac{Q^4}{4}(\frac{\partial < (\mathbf{R}(0)-\mathbf{R}(t))^2_Q >}{\partial t})^2+O(Q^4) \tag{C.6}$$

that is, in the limit $\mathbf{Q}\to\mathbf{0}$,

$$\frac{\partial^2 < (\mathbf{R}(0)-\mathbf{R}(t))^2_Q >}{\partial t^2} = -[\frac{2}{Q^2}\frac{\partial^2 F_i(Q,t)}{\partial t^2}]_{Q\to 0} \tag{C.7}$$

from which one infers

$$\omega^2[\frac{S_i(Q,\omega)}{Q^2}]_{Q\to 0} = \frac{1}{4\pi}\int_{-\infty}^{+\infty}\frac{\partial^2 < (\mathbf{R}(0)-\mathbf{R}(t))^2_Q >}{\partial t^2}e^{i\omega t}dt. \tag{C.8}$$

Being $< (\mathbf{R}(t+t')-\mathbf{R}(t'))^2_Q >= const.+ < R(t+t')R(t') >_Q$, and using the properties of the time correlation functions, if the x-direction is taken along $\mathbf{Q}$, then

$$\frac{\partial^2 < (\mathbf{R}(0)-\mathbf{R}(t))^2_Q >}{\partial t^2} = 2 < v_x(0)v_x(t) > . \tag{C.9}$$

Thus, finally

$$\omega^2[\frac{S_i(Q,\omega)}{Q^2}]_{Q\to 0} = \frac{1}{2\pi}\int_{-\infty}^{+\infty} < v_x(0)v_x(t) > e^{-i\omega t}dt = \tilde{z}(\omega). \tag{C.10}$$

This last relationship allows for retrieving the spectral density of the VACF from measurements of the dynamic structure factor if the investigated system can be reasonably approximated by an ensemble of incoherent scatterers.

D

Multivariate Gaussian distributions in DINS

In the framework of a harmonic (or quasi-harmonic) description of molecular vibrations, the momentum distribution of a poly-atomic molecular system can be effectively pictured as a 3D anisotropic multivariate normal distribution.
The general multivariate nD Gaussian with non-null correlations can be vectorially written as

$$\frac{1}{(2\pi)^{\frac{n}{2}}|\Sigma|^{\frac{1}{2}}}e^{-\frac{1}{2}(\mathbf{x}-\mu)^T\Sigma^{-1}(\mathbf{x}-\mu)} \tag{D.1}$$

where $\Sigma = (\Sigma_{ij})$ is the covariance matrix and $\rho_{ij} = \frac{\Sigma_{ij}}{\sigma_i\sigma_j}$ is any mutual correlation coefficient.

For $n = 3$ the covariance matrix has the form $\Sigma = \begin{pmatrix} \sigma_1^2 & \rho_{12}\sigma_1\sigma_2 & \rho_{13}\sigma_1\sigma_3 \\ \rho_{12}\sigma_1\sigma_2 & \sigma_2^2 & \rho_{23}\sigma_2\sigma_3 \\ \rho_{13}\sigma_1\sigma_3 & \rho_{23}\sigma_2\sigma_3 & \sigma_3^2 \end{pmatrix}$.

Given that

$$|\Sigma| = [1 + 2\rho_{12}\rho_{23}\rho_{13} - (\rho_{12}^2 + \rho_{23}^2 + \rho_{13}^2)](\sigma_1\sigma_2\sigma_3)^2 \tag{D.2}$$

and

$$cofactor\ \ matrix = COF(\Sigma) = COF^T(\Sigma) = \tag{D.3}$$

$$= \begin{pmatrix} (1-\rho_{23}^2)(\sigma_2\sigma_3)^2 & (\rho_{12}-\rho_{13}\rho_{23})\sigma_1\sigma_2\sigma_3^2 & (\rho_{12}\rho_{23}-\rho_{13})\sigma_1\sigma_2^2\sigma_3 \\ (\rho_{12}-\rho_{13}\rho_{23})\sigma_1\sigma_2\sigma_3^2 & (1-\rho_{13}^2)(\sigma_1\sigma_3)^2 & (\rho_{23}-\rho_{12}\rho_{13})\sigma_1^2\sigma_2\sigma_3 \\ (\rho_{12}\rho_{23}-\rho_{13})\sigma_1\sigma_2^2\sigma_3 & (\rho_{23}-\rho_{12}\rho_{13})\sigma_1^2\sigma_2\sigma_3 & (1-\rho_{12}^2)(\sigma_1\sigma_2)^2 \end{pmatrix} \tag{D.4}$$

and

$$\Sigma^{-1} = \frac{1}{|\Sigma|}COF^T(\Sigma), \tag{D.5}$$

one eventually finds that the 3D multivariate Gaussian with $\mu = (0,0,0)$ can be explicitly written as

$$\frac{e^{-\frac{1}{2\rho^2}[(1-\rho_{yz}^2)\frac{p_x^2}{\sigma_x^2}+(1-\rho_{xz}^2)\frac{p_y^2}{\sigma_y^2}+(1-\rho_{xy}^2)\frac{p_z{}^2}{\sigma_z^2}]-\frac{1}{\rho^2}[(\rho_{xy}-\rho_{xz}\rho_{yz})\frac{p_xp_y}{\sigma_x\sigma_y}+(\rho_{xy}\rho_{yz}-\rho_{xz})\frac{p_xp_z}{\sigma_x\sigma_z}+(\rho_{yz}-\rho_{xy}\rho_{xz})\frac{p_yp_z}{\sigma_y\sigma_z}]}}{(2\pi)^{\frac{3}{2}}\rho\sigma_x\sigma_y\sigma_z} \tag{D.6}$$

with $\rho^2 = 1 + 2\rho_{12}\rho_{23}\rho_{13} - (\rho_{12}^2 + \rho_{23}^2 + \rho_{13}^2)$.
In those cases when Σ gets diagonalized within a new $(x'y'z')$ reference system[1], Eq. D.6 reduces to

$$\frac{1}{(2\pi)^{\frac{3}{2}}}\frac{1}{\sigma_{x'}\sigma_{y'}\sigma_{z'}}e^{-\frac{1}{2}\left(\frac{p_{x'}^2}{\sigma_{x'}^2}+\frac{p_{y'}^2}{\sigma_{y'}^2}+\frac{p_{z'}^2}{\sigma_{z'}^2}\right)}. \tag{D.7}$$

In particular, if translations and librations are placed in a semiclassical picture, while vibrations retain full quantum description [133], this sigma-triplet can be related to the principal oscillation frequencies through

$$\sigma_{i'}^2 = \frac{M\omega_\lambda}{2\hbar}coth\frac{\beta\hbar\omega_\lambda}{2} \tag{D.8}$$

with λ being any normal mode.
Eq. D.7 should, in principle, model our $n(\mathbf{p})$.
Yet, the momentum distribution has to be averaged over all possible molecular orientations $\mathbf{\Theta}$, which are assumed isotropically distributed (as it's common for liquids and poly-crystals). This is equivalent - once that $\mathbf{\Theta}$ has been fixed at a convenient value $\mathbf{\Theta_d}$ (the one that diagonalizes Σ, for example) - to an average over every possible orientation of the momentum $\mathbf{p}$ [133,150], so that $n(\mathbf{p})$ can be finally expressed as the following spherical average

$$n(p) =< n(\mathbf{p}, \mathbf{\Theta_d}) >_{\hat{p}} =$$

$$= \frac{1}{4\pi}\frac{1}{(2\pi)^{\frac{3}{2}}}\frac{1}{\sigma_x\sigma_y\sigma_z}\int_0^{2\pi}d\phi\int_0^{\pi}sin(\theta)e^{-\frac{1}{2}p^2(\frac{sin^2(\theta)cos^2(\phi)}{\sigma_x^2}+\frac{sin^2(\theta)sin^2(\phi)}{\sigma_y^2}+\frac{cos^2(\theta)}{\sigma_z^2})}d\theta \tag{D.9}$$

with primes removed from any axis name.
This last object is *not* a univariate isotropic Gaussian: indeed, after some basic calculus one can easily assess that

$$n(p) = \frac{1}{2}\frac{e^{-\frac{1}{2}\frac{p^2}{\sigma_z^2}}}{(2\pi)^{\frac{3}{2}}\sigma_x\sigma_y\sigma_z} +$$

$$+\frac{1}{4\pi}\frac{1}{(2\pi)^{\frac{3}{2}}}\frac{1}{\sigma_x\sigma_y\sigma_z}\int_0^{2\pi}d\phi\frac{e^{-\frac{1}{2}p^2(\frac{cos^2(\phi)}{\sigma_x^2}+\frac{sin^2(\phi)}{\sigma_y^2})}}{\sqrt{\frac{1}{2}p^2(\frac{1}{\sigma_z^2}-\frac{cos^2(\phi)}{\sigma_x^2}-\frac{sin^2(\phi)}{\sigma_y^2})}}\int_{-\sqrt{\frac{1}{2}p^2(\frac{1}{\sigma_z^2}-\frac{cos^2(\phi)}{\sigma_x^2}-\frac{sin^2(\phi)}{\sigma_y^2})}}^{\sqrt{\frac{1}{2}p^2(\frac{1}{\sigma_z^2}-\frac{cos^2(\phi)}{\sigma_x^2}-\frac{sin^2(\phi)}{\sigma_y^2})}}e^{-t^2}dt = \tag{D.10}$$

$$= \frac{1}{2}\frac{e^{-\frac{1}{2}\frac{p^2}{\sigma_z^2}}}{(2\pi)^{\frac{3}{2}}\sigma_x\sigma_y\sigma_z} +$$

$$+\frac{1}{4\sqrt{\pi}}\frac{1}{(2\pi)^{\frac{3}{2}}}\frac{1}{\sigma_x\sigma_y\sigma_z}\int_0^{2\pi}d\phi\frac{e^{-\frac{1}{2}p^2(\frac{cos^2(\phi)}{\sigma_x^2}+\frac{sin^2(\phi)}{\sigma_y^2})}erf(\sqrt{\frac{1}{2}p^2(\frac{1}{\sigma_z^2}-\frac{cos^2(\phi)}{\sigma_x^2}-\frac{sin^2(\phi)}{\sigma_y^2})})}{\sqrt{\frac{1}{2}p^2(\frac{1}{\sigma_z^2}-\frac{cos^2(\phi)}{\sigma_x^2}-\frac{sin^2(\phi)}{\sigma_y^2})}}. \tag{D.11}$$

[1] One can always consider the molecular orientation along which Σ is diagonal.

Eq. D.10 (or D.11) is clearly not a 1D Gaussian; further, it must be evaluated numerically, just as any expression containing the definite integral of a Gaussian integrand over a finite range.
The corresponding NCP turns out to be

$$J_{IA}(y) = 2\pi\hbar \int_{|\hbar y|}^{\infty} p < n(\mathbf{p}, \mathbf{\Theta_d}) >_{\hat{p}} dp =$$

$$= \frac{\hbar}{2} \frac{1}{(2\pi)^{\frac{3}{2}}} \frac{1}{\sigma_x \sigma_y \sigma_z} \int_{|\hbar y|}^{\infty} pdp \int_0^{2\pi} d\phi \int_0^{\pi} sin(\theta) e^{-\frac{1}{2}p^2 (\frac{sin^2(\theta)cos^2(\phi)}{\sigma_x^2} + \frac{sin^2(\theta)sin^2(\phi)}{\sigma_y^2} + \frac{cos^2(\theta)}{\sigma_z^2})} d\theta, \tag{D.12}$$

or, defining $S(\theta, \phi) = \frac{sin^2(\theta)cos^2(\phi)}{\sigma_x^2} + \frac{sin^2(\theta)sin^2(\phi)}{\sigma_y^2} + \frac{cos^2(\theta)}{\sigma_z^2}$,

$$J_{IA}(y) = \frac{\hbar}{2} \frac{1}{(2\pi)^{\frac{3}{2}}} \frac{1}{\sigma_x \sigma_y \sigma_z} \int_0^{2\pi} d\phi \int_0^{\pi} sin(\theta) d\theta \int_{|\hbar y|}^{\infty} p e^{-\frac{1}{2}p^2 S(\theta,\phi)} dp \tag{D.13}$$

that is ($S(\theta, \phi)$ always being strictly positive),

$$J_{IA}(y) = \frac{\hbar}{2} \frac{1}{(2\pi)^{\frac{3}{2}}} \frac{1}{\sigma_x \sigma_y \sigma_z} \int_0^{2\pi} d\phi \int_0^{\pi} sin(\theta) \frac{1}{S(\theta, \phi)} e^{-\frac{1}{2}S(\theta,\phi)\hbar^2 y^2} d\theta \tag{D.14}$$

which once again calls for a numerical evaluation.

E

Binding potential going anharmonic: the Morse oscillator

A common choice to describe the spectroscopy of diatomic molecules (and anharmonic vibrational dynamics in general) is the 1D Morse oscillator [192], which is a model for a particle in a one-dimensional anharmonic potential energy surface with a dissociative limit at infinite displacement.
The analytical form of the Morse potential in one dimension is

$$V(x) = D_e(1 - e^{-\alpha x})^2 \tag{E.1}$$

where D_e sets the depth of the minimum, $x = r - r_e$ its offset, and α the curvature of the potential (Fig. E.1).
If V is expanded in powers of x around $x = 0$

$$V(x) = \frac{1}{2}k_0x^2 + \frac{1}{6}gx^3 + \frac{1}{24}hx^4 + ... \quad , \tag{E.2}$$

an easy relation between the harmonic constant k_0 and Morse parameters D_e and α can be found, since $k_0 = 2D_e\alpha^2$ (as well as $g = -6D_e\alpha^3$, $h = 14D_e\alpha^4$, etc.).
Solving the Schroedinger equation for a diatomic molecule of reduced mass m_R under Morse potential, the energy eigenvalues in the position space turn out of the form

$$E_n = \hbar\omega_0 \left[\left(n + \frac{1}{2}\right) - x_e\left(n + \frac{1}{2}\right)^2\right] \qquad n = 0, 1, 2, ... \tag{E.3}$$

where $\omega_0 = \sqrt{\frac{2D_e\alpha^2}{m_R}}$ is the (harmonic) fundamental frequency, and $x_e = \frac{\hbar\omega_0}{4D_e}$ represents the anharmonic constant.
The dissociation energy is given by $D_0 = D_e - E_0 = D_e - \frac{1}{2}\hbar\omega_0\left(1 - \frac{1}{2}x_e\right)$.
The associated (skewed, real) eigenfunctions can be analitically expressed in closed form [193] as

$$\psi_{\lambda,n}(y) = N(\lambda, n)\xi^{\lambda-n-\frac{1}{2}}e^{-\frac{\xi}{2}}L_n^{(2\lambda-2n-1)}(\xi) \qquad n = 0, 1, ..., \left(\lambda - \frac{1}{2}\right) \tag{E.4}$$

where $y = \alpha x$ is a dimensionless variable, $\lambda = \frac{\sqrt{2m_RD_e}}{\alpha\hbar}$ a dimensionless parameter, $\xi = 2\lambda e^{-y}$, $N(\lambda, n) = \sqrt{\frac{(2\lambda-2n-1)\Gamma(n+1)}{\Gamma(2\lambda-n)}}$ is the normalization constant, $\Gamma(z) = \int_0^\infty e^{-t}t^{z-1}dt$ (with $Re(z) > 0$) is the Gamma function and L_n the Laguerre polynomial of order n [194].

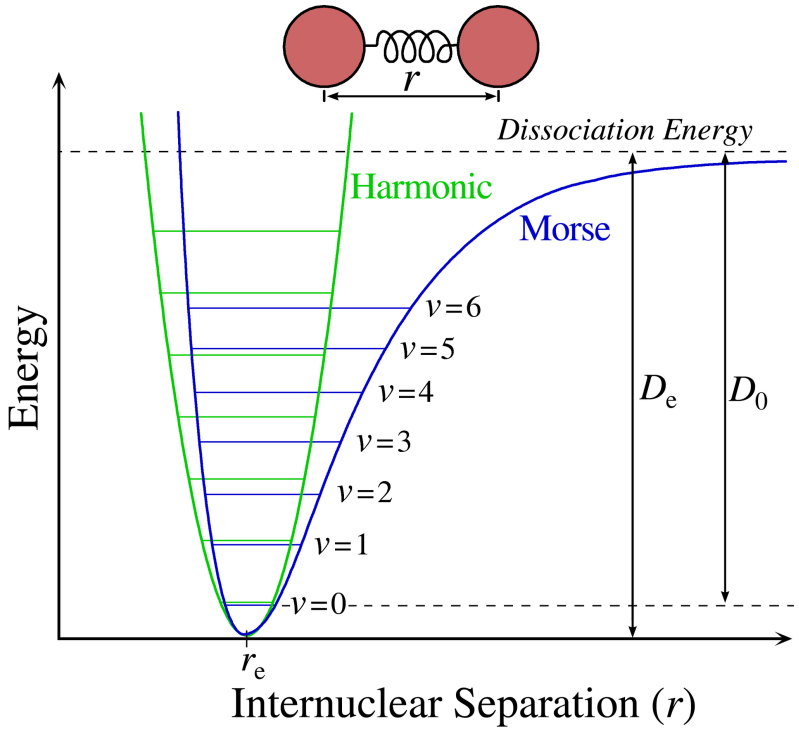

Figure E.1: 1D Morse (blue) and corresponding harmonic potential (green). D_e is the well depth, D_0 the true energy required for dissociation due to the zero-point energy of the ground-state. Unlike the harmonic energy levels, which are evenly spaced, the eigenvalues for the Morse case show a spacing that decreases as the energy approaches the dissociation value. Credits: Somoza - Own work. Licensed under CC BY-SA 3.0 via Commons.

In the momentum space, on the other hand, the eigenfunctions of the Morse oscillator are complex and their compact expression is

$$\overline{\psi}_{\lambda,n}(k) = N(\lambda,n)(2\pi)^{-\frac{1}{2}}2^{\lambda-n-\frac{1}{2}}\lambda^{-ik}\sum_{j=0}^{n}2^j b(\lambda,n;j)\Gamma\left(\lambda-n+j-\frac{1}{2}+ik\right), \quad \text{(E.5)}$$

where the dimensionless coordinate $k = \frac{p}{\alpha\hbar}$ is introduced, as well as $b(\lambda,n;j) = \frac{(-1)^j}{j!}\frac{\Gamma(2\lambda-n)}{\Gamma(2\lambda-2n+j)\Gamma(n-j+1)}$.

F

The momentum distribution in the PI representation

The quantum mechanics of many-body systems is a hardly chewable bite. One - often neglected - of Feynman's early successes with path integrals (PIs) was his mapping of a quantum system by PIs onto a classical model of interacting 'polymers' [195]. The asset of this procedure is that, apart from providing a physical picture, the PI approach directly translates into a computational method: indeed, the polymers can be simulated by either PI Monte Carlo (PIMC) or PI molecular-dynamics (PIMD) techniques and can be understood with the aid of classical statistical mechanics.
As known, all properties of a quantum system in thermal equilibrium can be obtained via the thermal density matrix $\rho = e^{-\beta\mathcal{H}}$ in the case of the canonical ensemble[1].
Given its product property, the operator at a temperature T can be re-expressed in terms of density matrices at a temperature PT with time step $\tau = \frac{\beta}{P}$

$$e^{-\beta\mathcal{H}} = (e^{-\tau\mathcal{H}})^P, \tag{F.1}$$

or, in the position representation,

$$\rho(R_0, R_P; \beta) = \int ..... \int dR_1 .....dR_{P-1} \rho(R_0, R_1; \tau)\rho(R_1, R_2; \tau).....\rho(R_{P-1}, P_M; \tau). \tag{F.2}$$

This expression is exact for any value of P; it merely replaces the density matrix at an inverse temperature β with a product of P density matrices at the smaller inverse temperature τ.
Since no known analytic expression exists for the density matrix of an arbitrary Hamiltonian at finite temperature, it is usual, at this point, to resort to approximate expressions [37]. One popular choice is the so-called 'primitive' approximation, which is a 2^{nd}-order one, being it correct to order τ^2.
If the Hamiltonian is splitted into (nonrelativistic) kinetic and potential operators ($\mathcal{H} = \mathcal{T} + \mathcal{V}$), and the following exact operator identity is taken into account

$$e^{-\tau(\mathcal{T}+\mathcal{V})+\frac{\tau^2}{2}[\mathcal{T},\mathcal{V}]} = e^{-\tau\mathcal{T}}e^{-\tau\mathcal{V}}, \tag{F.3}$$

the primitive approximation can be written as

$$e^{-\tau(\mathcal{T}+\mathcal{V})} \sim e^{-\tau\mathcal{T}}e^{-\tau\mathcal{V}}, \tag{F.4}$$

[1]The generalization to other ensembles is straightforward.

once one observes that, as $\tau \to 0$ (PT large enough), the commutator term on the left-hand side of Eq. F.3 can be neglected in comparison to other terms.
As a result, the exact density matrix can be approximated by the product of the density matrices of $\mathcal{T}$ and $\mathcal{V}$ alone[2].
Chosen a suitable complete basis, the primitive approximation in the position space can be written down as

$$\rho(R_0, R_2; \tau) \sim \int dR_1 \left\langle R_0 | e^{-\tau \mathcal{T}} | R_1 \right\rangle \left\langle R_1 | e^{-\tau \mathcal{V}} | R_2 \right\rangle. \tag{F.6}$$

where

$$\left\langle R_1 | e^{-\tau \mathcal{V}} | R_2 \right\rangle = e^{-\tau \mathcal{V}(R_1)} \delta(R_2 - R_1) \tag{F.7}$$

since the potential operator is diagonal in this representation; and[3]

$$\left\langle R_0 | e^{-\tau \mathcal{T}} | R_1 \right\rangle = \sum_n L^{-3N} e^{-\tau \lambda K_n^2 - i K_n (R_0 - R_1)} = (4\pi\lambda\tau)^{-\frac{3N}{2}} e^{-\frac{(R_0 - R_1)^2}{4\lambda\tau}} \tag{F.8}$$

in the case of distinguishable particles[4] in a cube of side L and periodic boundary conditions, with $\mathbf{n}$ a 3D integer vector and $\mathbf{K_n} = \frac{2\pi \mathbf{n}}{L}$ [195].
This way the discrete PI expression for the density matrix in the primitive approximation gets shaped as

$$\rho(R_0, R_P; \beta) = \int dR_1 ..... dR_{P-1} (4\pi\lambda\tau)^{-\frac{3NP}{2}} e^{-\sum_{m=1}^{P} \left[\frac{(R_{m-1} - R_m)^2}{4\lambda\tau} + \tau \mathcal{V}(R_m) \right]}, \tag{F.9}$$

and it links the quantum density matrix at any temperature to integrals over the path $R_1 .... R_{M-1}$ of something resembling a classical Maxwell-Boltzmann distribution function.
There you have the mapping from a quantum system to a classical one.
Eq. F.9 can be just interpreted as a classical configuration integral; the action has a classical analogue, which corresponds to the one of a chain of P beads connected by springs. This quantum chain is called a polymer. In particular, the formula for diagonal elements[5] of ρ involves a P-step closed path: a ring polymer.
As seen in paragraph 6.2, the momentum distribution is a Fourier transform involving off-diagonal terms of ρ, in contrast to the partition function, which is only determined by diagonal contributions. Thus the closed paths commonly employed to retrieve Z (with all related thermal quantities) cannot be used to calculate $n(\mathbf{p})$.

[2] One might worry about possible errors in the limit $P \to \infty$. Yet, according to the Trotter formula:

$$e^{-\beta(\mathcal{T}+\mathcal{V})} = \lim_{P \to \infty} [e^{-\tau \mathcal{T}} e^{-\tau \mathcal{V}}]^P, \tag{F.5}$$

provided that $\mathcal{T}$, $\mathcal{V}$ and $\mathcal{T} + \mathcal{V}$ are self-adjoint and make sense separately.

[3] This is obtained by approximation of a sum by an integral, which is correct when $\lambda\tau \ll L^2$, that is, when the thermal wavelength of one step is much smaller than the size of the box.

[4] This condition can be loosened.

[5] Keep in mind that thermodynamical properties are determined by the trace of the density matrix.

What's usually done is to remove the restriction on just one atom of the system about its return to its starting position. The classical simulation will be then executed on $(N-1)$ ring polymers and one linear polymer.